

RADIATIVE-DIFFUSIVE MODELS
OF THE ARCTIC BOUNDARY LAYER

by

GERALD F. HERMAN

A.B., University of Chicago, 1970

S.M., Massachusetts Institute of Technology, 1972

SUBMITTED IN PARTIAL FULFILLMENT OF THE
REQUIREMENTS FOR THE DEGREE OF DOCTOR OF SCIENCE

at the

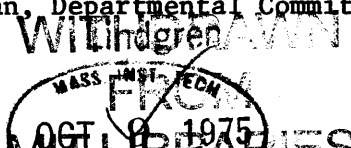
MASSACHUSETTS INSTITUTE OF TECHNOLOGY

June, 1975

Signature of Author
Department of Meteorology, June, 1975

Certified by
Thesis Supervisor

Accepted by
Chairman, Departmental Committee on Graduate Students



RADIATIVE-DIFFUSIVE MODELS OF THE ARCTIC BOUNDARY LAYER

by

Gerald F. Herman

Submitted to the Department of Meteorology on 20 June 1975
in partial fulfillment of the requirements for the degree
of Doctor of Science.

ABSTRACT

Persistent and extensive layers of stratiform cloud occur over the Arctic basin from late spring until early fall. The frequency of low cloudiness is greater than seventy percent, and these high values are found in all regions of the Central Polar Ocean and the peripheral seas. The clouds occur frequently as two or more well-defined stratus layers approximately 300 m thick that are separated by distinct clear regions of the same approximate depth.

We attempt to find self-consistent radiative-diffusive models that will predict the observed multiple stratus layers. We consider the formation of Arctic stratus clouds in the relatively warmer and moister continental air as it flows over the pack ice. The initial profiles of temperature and relative humidity as well as their values at the surface are specified in advance, and the modification of the continental air is calculated as a time marching problem.

Turbulent transport in the surface layer is parameterized by the Monin-Obukhov similarity formulation. Above the surface layer a simple mixing-length formulation is used, except in the unstable cases when a convective adjustment is used.

Solar radiation is treated with Chandrasekhar's "First Approximation". The water vapor spectrum in the NIR is represented with two grey absorption coefficients, and the cloud is treated as a grey scatterer and absorber. Thermal radiation is computed with emissivities. The cloud is a grey absorber and emitter in the thermal spectrum, and a "mixed-emissivity" is computed for the cloud-gas mixture.

We find that condensation is induced in an initially unsaturated air mass due to diffusive cooling to the colder surface and longwave emission to space. Intense mixing within the cloud is generated by strong cooling due to droplet emission at the cloud top. A bi-layered structure

develops, and we attribute this to a greenhouse mechanism whereby solar radiation penetrates to the interior of the cloud and causes evaporation there, while at the same time the top remains cold due to emission to space, and the lowest layer remains cold since the surface temperature is fixed at 0°C. A mechanism is also suggested for the lifting of a cloud top due to longwave emission in the clear atmosphere directly above the cloud.

It is suggested that the persistence of stratus clouds in the Arctic is due to the absence of dissipative mechanisms that are ordinarily encountered at lower latitudes. Condensation occurs initially over a fairly rapid time scale, but convective heating and solar radiation act too slowly to dissipate the resulting cloud layers.

It is also suggested that the summertime maximum of low cloudiness is associated with the maximum in the surface temperature of the ice which occurs during the summer season.

Thesis Supervisors:

Richard M. Goody

Title: Mallinckrodt Professor of Planetary Physics, Harvard University

Reginald E. Newell

Title: Professor of Meteorology, Massachusetts Institute of Technology

DEDICATION

To the memory of my father, Algerd G. Herman

ACKNOWLEDGEMENTS

I am pleased to acknowledge those who have so kindly contributed their time and effort during the course of my graduate education. My thanks are due to the following:

Professor Reginald E. Newell, for his active and personal interest in my development as a scientist. He has been and remains a continuous source of intellectual stimulation and inspiration.

Professor Richard Goody, for his active interest and sound advice during the course of my thesis work. His kind and very patient application of the Socratic method has provided me with valuable insights into the science of meteorology, and into myself as a meteorologist.

Professor Henry Houghton, for his wise counsel and continuous encouragement during all phases of my graduate education. I am particularly grateful for the support which he offered when I most needed it.

And to numerous friends and colleagues who offered their comments and criticism during the course of this work.

I am also grateful for the moral support provided by the following: F.A. Wiener, P.A. Cunerty, B.A. Waraksa, D.E. McLaughlin, J.C. Bauer, H.A. Richter, and N. Wieckowicz.

I appreciate the hospitality of the Center for Earth and Planetary Physics of Harvard University in allowing me to use their facilities during the preparation of this thesis.

I appreciate the excellent work of Miss Isabelle Kole, who drafted the diagrams, and of Ms. Eve Sullivan, who typed the manuscript.

This work was done while the author was supported as a research assistant under ERDA, Division of Biomedical Research.

TABLE OF CONTENTS

	Page
ABSTRACT	2
DEDICATION	4
ACKNOWLEDGEMENTS	5
TABLE OF CONTENTS	6
LIST OF FIGURES	8
LIST OF TABLES	10
1. THE OBSERVED PHENOMENA	11
1.1 Cloud Morphology	11
1.1.1 Areal-averaged seasonal variation	11
1.1.2 Seasonally-averaged geographic distribution	12
1.1.3 Mean vertical distribution	12
1.1.4 Distribution on the synoptic scale	20
1.2 Relevant Features of the Circulation at High Latitudes	20
1.2.1 The mean circulation	20
1.2.2 Synoptic features	21
1.2.3 Temperature and wind	22
1.2.4 Relative humidity	24
1.3 Macrometeorological Conditions	29
1.3.1 Heat and moisture fluxes at the surface	29
1.3.2 Thermodynamic state of the lower boundary	31
1.3.3 Main characteristics of the radiation field	32
1.3.4 Albedo	34
1.4 Cloud Microphysics	34
2. STATEMENT OF PROBLEM AND METHOD OF SOLUTION	37
2.1 The Problem	37
2.1.1 Structure and mechanism	37
2.1.2 Geographic distribution	38
2.1.3 Seasonal behavior	38
2.2 Method of Solution	39
2.2.1 General discussion	39
2.2.2 Basic equations	42
2.3 Previous Relevant Investigations	45

	Page
3. PARAMETERIZATIONS	47
3.1 Parameterization of Turbulence	47
3.1.1 The surface layer	47
3.1.2 Effects of horizontal inhomogeneity and radiative transfer	55
3.1.3 Turbulence above the surface layer	61
3.2 Radiative Transfer	64
3.2.1 The "First Approximation"	64
3.2.2 Solar radiation	67
3.2.3 Thermal radiation	82
4. RESULTS AND DISCUSSION	95
4.1 Mechanism and Structure	95
4.1.1 The basic states	95
4.1.2 Initiation of condensation	100
4.1.3 Development	104
4.1.4 Radiative processes	114
4.1.5 Variation of parameters	124
4.1.6 Properties of the upper cloud layer	133
4.2 Geographical Effects	137
4.2.1 Persistence	137
4.2.2 Separation	139
4.2.3 Other effects	143
4.3 Seasonal Behavior	144
APPENDICES	147
LIST OF SYMBOLS	157
REFERENCES	164
BIOGRAPHICAL NOTE	171

LIST OF FIGURES

Figure		Page
1.1	Annual march of total cloud amount in the Arctic.	14
1.2	Annual march of low cloud amount and frequency.	15
1.3	Annual march of low cloudiness, 1955-1959.	16
1.4	Distribution of total cloud amount in the Arctic.	17
1.5	Frequency of low cloudiness in the Arctic.	18
1.6	Vertical distribution of stratus clouds observed by Weller.	19
1.7	Energy transports in the Arctic.	25
1.8	Cyclone behavior in the Arctic during July.	26
1.9	Temperature profiles under Arctic stratus.	27
1.10	Aircraft measurements of temperatures within Arctic stratus.	28
1.11	Duration of daylight in the Arctic, and drop-size distribution for Arctic stratus.	36
3.1	Bulk Richardson number as function of z/L .	52
3.2	Heat and momentum transfer coefficients.	53
3.3	Radiative and turbulent lifetimes.	60
3.4	Empirical fit to the absorption data of Yamamoto.	77
3.5	Behavior of the scattering parameter β .	78
3.6	Reflectivities and transmissivities computed by the model.	79
3.7	Sample cloud heating rates for 500 m cloud.	80
3.8	Variation of cloud heating rate with surface albedo.	81
3.9	Mixed emissivity as function of water vapor amount.	91
3.10	Mixed emissivity as function of droplet path length.	92
3.11	Graphic solution to infrared heating rate equation.	93
3.12	Sample infrared heating rates.	94
4.1	Liquid water distribution for warmer air flowing over colder ice surface.	98
4.2	Liquid water distribution for cooler air flowing over warmer ice surface.	99
4.3	Liquid water distribution computed with Estoque's eddy diffusivity.	107
4.4	Liquid water distribution computed with 2 m sec^{-1} basic current	108
4.5	Liquid water distribution for hypothetical atmosphere with no turbulence.	109

Figure	Page
4.6 Radiative equilibrium temperatures for selected values of τ_T^* .	113
4.7 Liquid water distribution for hypothetical atmosphere with no radiation.	117
4.8 Components of the radiative and turbulent regimes computed by model.	120
4.9 Liquid water distribution for realistic diurnal cycle.	122
4.10 Sample temperature profiles computed by model.	123
4.11 Cloud distributions for oscillatory solar heating functions.	142
4.12 Annual march of temperature of the pack ice, and integrated liquid water computed by model.	146
B1. Weighting functions for extinction parameters in solar spectrum.	150
B2. Weighting functions for extinction parameters in infrared spectrum.	151

LIST OF TABLES

Table	Page
1.1 Cloud parameters from Russian measurements	13
1.2 Radiation measurements in Arctic stratus by Koptev and Voskresenskii	34
1.3 Observations of mean stratiform cloud properties during summer conditions	35
3.1 Coefficients for 4-point fit	71
3.2 Planck mean cloud efficiencies (Solar spectrum)	74
3.3 Planck mean cloud efficiencies (Thermal spectrum)	82
3.4 Scattering parameter $\bar{\beta}$	83
4.1 Cloud conditions for varying absorption cross sections, χ_a^T	127
4.2 Cloud conditions for varying solar absorption cross sections, χ_a^S	128
4.3 Cloud conditions for varying surface reflectivity, α	129
4.4 Cloud conditions for varying surface roughness, z_o	130
4.5 Cloud conditions for varying mean vertical velocities, w	131
4.6 Cloud conditions for varying initial stability, N^2	132

1. THE OBSERVED PHENOMENA

The most striking feature of the climate of the summertime Arctic is the persistence of extensive layers of stratiform cloud over the Polar oceans from mid-May through mid-September. These cloud layers, which we shall hereafter refer to as summertime Arctic stratus, represent a very difficult problem since they occur as a result of meteorological processes that occur over a wide range of scales. Their structure is at the same time related to the large-scale transports of heat and moisture into the Arctic Basin, which is a problem of the general circulation, and to the optical and thermal properties of the liquid water drops, which are important for the microphysical processes of radiative transfer and cloud physics. We shall attempt to form a cohesive explanation for structure, distribution and persistence of summertime Arctic stratus. The relevant features of Arctic meteorology that we need to consider are described in the following sections.

1.1 CLOUD MORPHOLOGY

1.1.1 Areally-averaged Seasonal Variation

Although long-term cloud statistics have not yet been compiled, an accurate picture of the monthly variation of spatially-averaged cloud conditions can be found in the studies of Huschke (1969) and Vowinckel and Orvig (1970). Fig. 1.1 shows the annual march of total cloud amount in various regions of the Arctic. The variability of the total cloud amount is dominated by the variability of low or stratiform clouds, as shown in Fig. 1.2. Both the frequency of occurrence and the total cloud amount increase to their maximum summertime values over a very short transitional

period. The frequency and cloud amount are step-functions in time, and this behavior is evident in each of the five years of the Huschke study (Fig.1.3) and appears to be a permanent climatological feature, although it is less pronounced in the Canadian Arctic than in the other regions. The lower values in the Canadian Arctic presumably are due to the large number of continental stations in that sector, especially on the Greenland ice cap, which ordinarily have much lower total cloudiness.

Note also that each figure shows a very slight minimum during the middle of the summer season. This depression may be related to minima in the sensible and latent heat fluxes calculated for that period by several authors. This feature will be discussed in a later section.

1.1.2 Seasonally-averaged Geographic Distribution

The isolines of total cloud amount in the Arctic Basin are almost axially symmetric, with values increasing toward the pole (Fig.1.4). The low cloud frequencies also show the same symmetry (Fig.1.5).

Upper-level clouds occur infrequently in the Arctic Basin during the summer, and are associated with the migratory lows which traverse that region. Over the adjacent continents the cloud cover tends to be high, and is due largely to the increased convective activity over the warm land surfaces. The Norwegian and Barents Seas also are extremely cloudy, but this cloudiness is associated with the quasi-permanent Icelandic low. The Greenland continent has high values of upper- and middle-level cloudiness, but is free of low cloud all year round.

1.1.3 Mean Vertical Distribution

The cloud morphology in the vertical is harder to establish due to the difficulty of inferring vertical structure from surface-based

measurements on the pack ice. The little that is known about the vertical structure ordinarily has been obtained in aircraft experiments that were designed to study cloud microphysics. The mean cloud parameters shown in Table 1.1 originate from the work of Dergach et al. (1960), Zavarina and Romasheva (1957), and Dolgin (1960).

Table 1.1
Cloud Parameters from Russian Measurements

	Zavarina and Romasheva	Dergach <u>et al.</u>	Dolgin
Mean Base	-	200-300m	-
Mean Thickness	350-500m	150-250m	350m
Minimum Thickness	100-150m	50m	-
Maximum Thickness	1000m	700m	-

This is an unsatisfactory picture insofar as it gives no information regarding the seasonal or geographic variation of the mean thickness or height. Moreover, it gives no indication of layering, a mysterious feature of these clouds that has been observed by aviators in the Arctic for many years, but that has only recently been mentioned in the meteorological literature (Jayaweera and Ohtake, 1973). It appears that it is common for Arctic stratus to occur in a number of well-defined layers separated by intervening clear regions which are several hundred meters thick. The layered nature of these clouds has been observed in a few flights made by Weller (Personal communication, 1974), and is shown schematically in Fig.1.6. Although only two- and three-layered clouds are documented here, reports have been made of as many as five simultaneous layers. Clearly, a cohesive explanation for the layered nature of these clouds cannot be formed from these few observations. However, until more studies are made we must

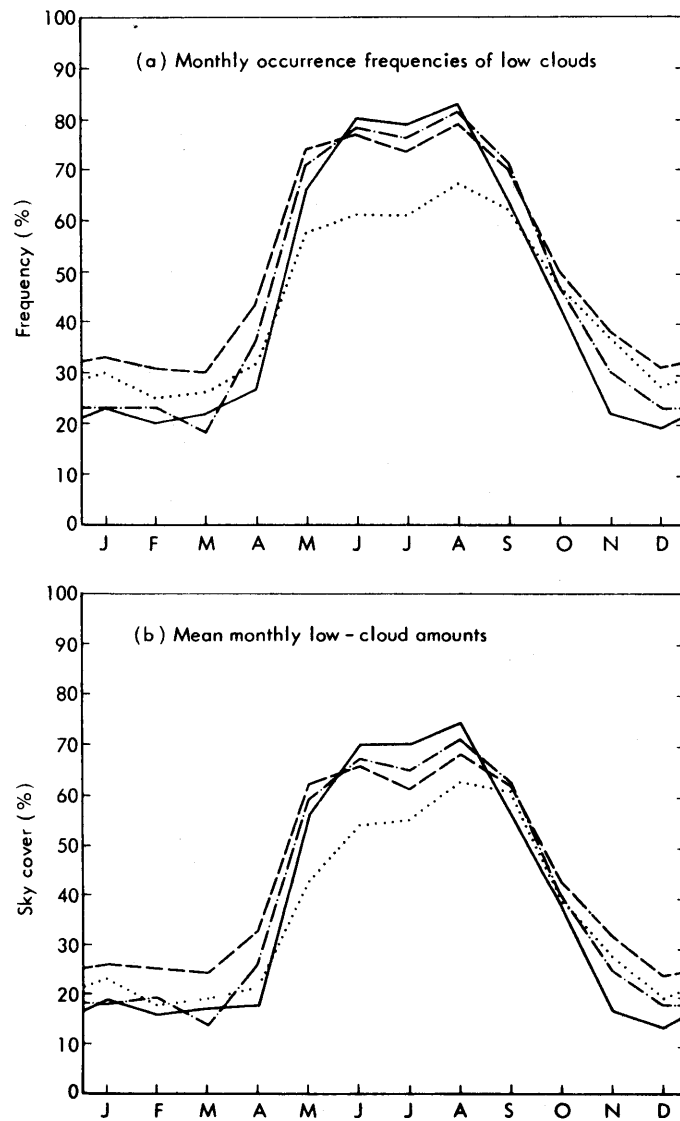
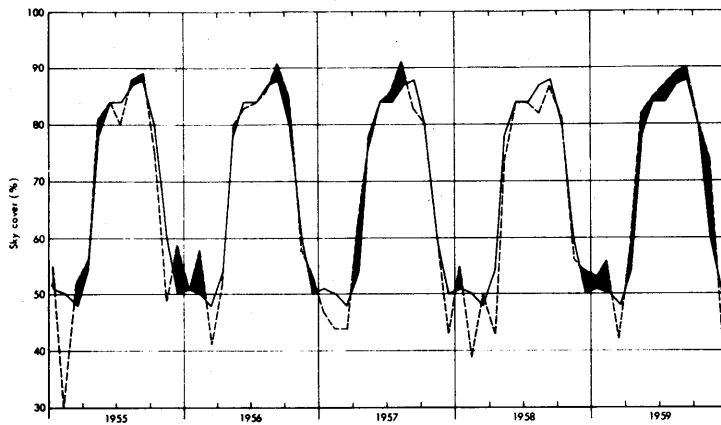
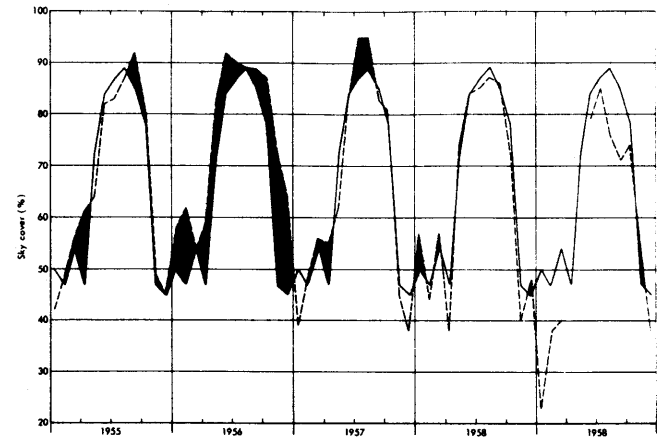


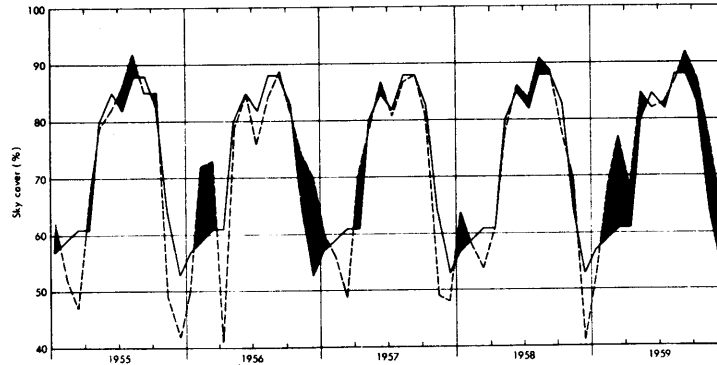
Fig. 1.2 Annual march of low cloud amount and low cloud frequency. Broken lines indicate same regions as in Fig.1.1 (after Huschke, 1969).



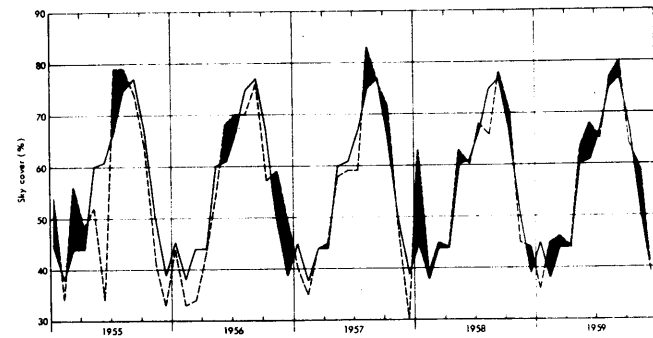
Region II



Region IV



Region I



Region III

Fig. 1.3 Annual march of total cloud amount over 5 year period (broken line), and the 5-year average (solid line) (after Huschke, 1969).

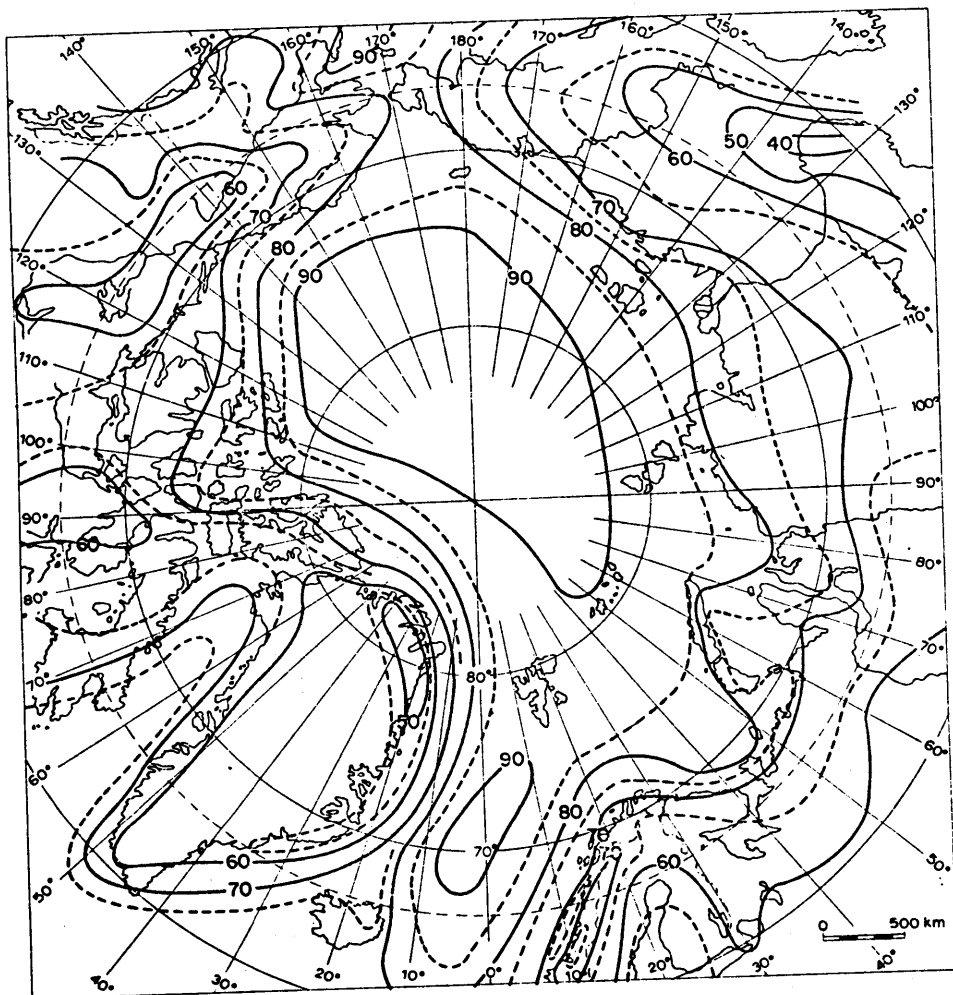


Fig. 1.4 Isolines of total cloud amount in July (after Vowinckel and Orvig, 1970).

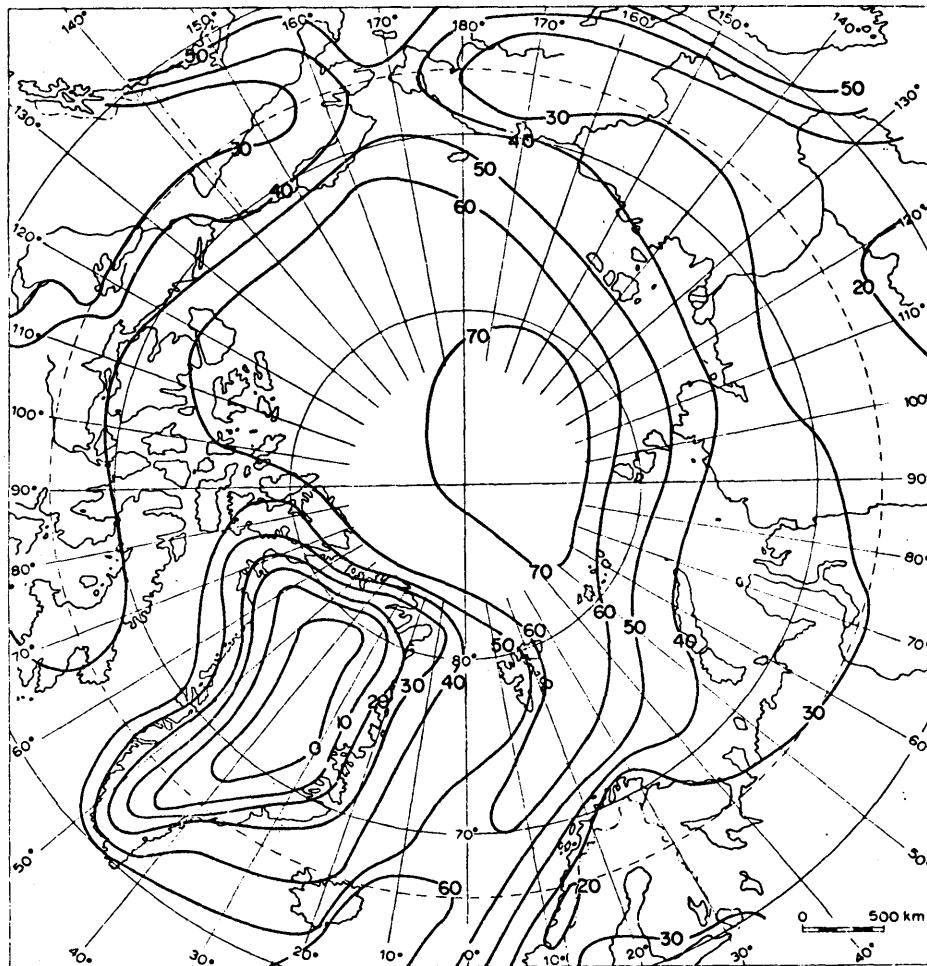


Fig. 1.5 Isolines of low cloud frequency in summer (after Vowinckel and Orvig, 1970).

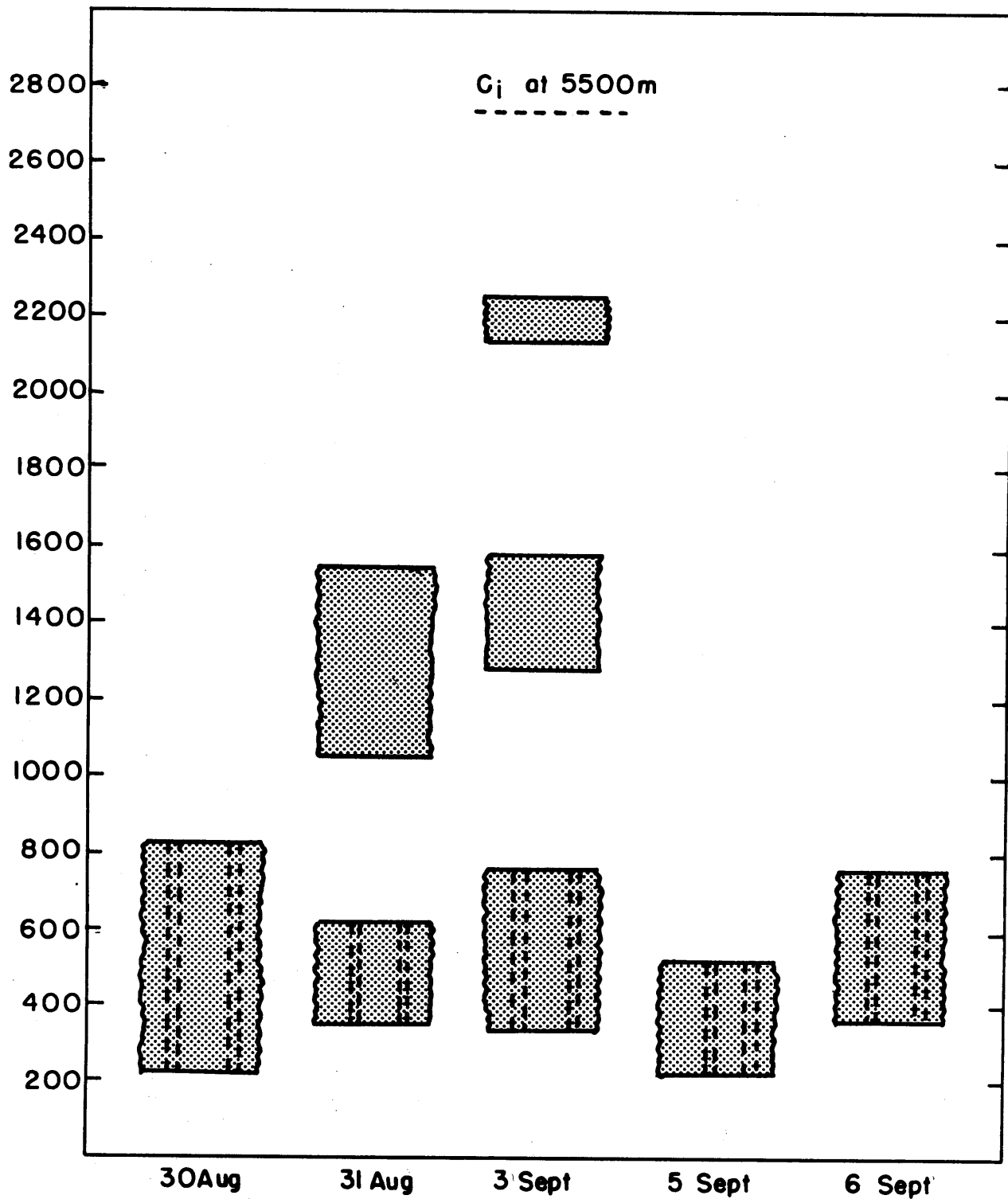


Fig. 1.6 Schematic diagram of the cloud distribution in the vertical at Barrow Alaska for several days in 1971. Dotted lines indicate breaks or gaps in the cloud layer (adapted from data kindly provided by Gunter E. Weller).

rely on this crude picture, along with the hearsay evidence of flyers, which points to layering as a rule rather than an exception.

1.1.4 Distribution on the Synoptic Scale

We know very little about the extent or duration of the individual stratus decks which comprise the long-term means. Presumably this information could be inferred from the Ptarmigan military reconnaissance data (Belmont, 1958) or from the surface data that went into the Huschke analysis. Zavarina and Dyuzheva (1959, quoted by Gavrilova (1963)) give a mean horizontal extent of stratiform clouds in the Soviet Arctic of 400-600km. Dolgin (1960) states a similar mean of 460km, with extreme values of 2000km. There are no data pertaining to the extent and variation of any of the multiple layers within a deck, or to the horizontal variation of their base and top heights. Such information is needed to study the life history of an individual set of layers in the Lagrangian sense. Observations of Arctic stratus on shorter time- and smaller space-scales simply do not exist.

1.2 RELEVANT FEATURES OF THE CIRCULATION AT HIGH LATITUDES

1.2.1 The Mean Circulation

The general circulation at high latitudes is difficult to describe mainly because there are so few reporting stations. The M.I.T. General Circulation Library, for example, retains twenty-four stations north of 70°, and only four stations north of 80°. Consequently, good statistics are difficult to establish.

The results of Newell et al. (1972, p.45) and of Oort and Rasmussen (1971, p.23) do indicate a trace of a direct polar cell similar to that first envisaged by Bergeron. But during the winter its associated mass fluxes are two orders of magnitude smaller than those of the tropical

Hadley cell, and are smaller yet during the summer. The transport of heat which is needed to compensate for the energy loss in the polar region is effected almost exclusively by the standing and transient eddies. The latter dominate during the summer, and the former during the winter (Oort, 1974). The relative importance of these transports is illustrated in Fig.1.7. The transient eddy contribution is large and positive, and so is the standing eddy contribution in all seasons except the late spring and early summer. The direct cell is always weak, and may even become indirect during the summer.

1.2.2 Synoptic Features

The picture of the Arctic Basin as a region of quasi-permanent anticyclonic circulation has, in recent years, been replaced by one of a region of low pressure and vigorous cyclonic activity. The analyses of Dzerdzevskii (1945) and of Reed and Kunkel (1960) both indicated that there is a low pressure center of about 1005 mb located at about 85°N - 180°W during the summer, and that it is quite symmetrical with respect to the location of the pack ice. Cyclones that enter the central polar basin ordinarily are old and occluded, and fill and decay somewhere over the pack ice. They originate mostly in the active baroclinic zones along the coasts which are associated with the thermal contrasts between the cold polar oceans and the warmer land surfaces, or else they are remnants of disturbances from the mid-latitude storm track, and enter the Arctic either from the North Atlantic or through the Bering Strait (Fig.1.8). The coastal baroclinic zone is a feature that is peculiar to the summertime Arctic, and is partly the reason that the frequency of cyclones is as large during the summer as during the winter. The zonally-averaged frequency of cyclones showed a minimum in the region 70 - 75°N and a maximum around 80 - 90°N during

the summer period in the Reed and Kunkel analysis.

Anticyclones tend to be scarce, with only three traversing the basin in the course of a typical summer. There are no permanent anticyclones in the vicinity of the pack ice, and most highs tend to be poorly defined remnants of the strong anticyclones of Central Greenland, Central Siberia, and the Canadian Archipelago.

During the summer the melting pack ice acts as a buffer, and this constrains the surface layer to remain close to 0°C; consequently, fronts are difficult to observe at the surface. However, upper air observations indicate that they are frequent during the summer. Fronts most frequently develop along the northern shores of Alaska, Canada, and Siberia, but do not completely encircle the Arctic Basin.

The Reed and Kunkel analysis indicated that the distribution of high- and middle-level clouds with respect to the location of fronts and cyclones was essentially the same as in mid-latitude synoptic systems. The greatest cloudiness tended to occur in advance of a wave disturbance and near occlusions, and the least cloudiness to the rear of the wave or occlusion. Low cloud, however, was always present, quite irrespective of the synoptic pattern. Some variability was found insofar as the low cloudiness tended to increase poleward and decrease toward the coast, but, in general, the low cloudiness was a "basic state" upon which was superimposed the normal distribution of high and middle level clouds associated with the synoptic situation.

1.2.3 Temperature and Wind

The stratification of the boundary layer over the pack ice during the summer is determined mainly by the melting ice and snow which maintains a surface temperature that does not deviate substantially from zero degrees.

During the melting season, which begins about June 15 and ends about August 20 (Untersteiner, 1964), convection in the surface layer is minimal (Vowinckel and Taylor, 1965, Table 4).

The most intensely convective periods occur during the late spring and early fall, if we assume that the calculated values of the sensible heat flux are valid indicators of convective activity.

The temperature structure has been studied in detail with kites and tethered balloons (Sverdrup, 1933), with dropsondes (Poage, 1954), and from surface observations and radiosonde data (Belmont, 1958; Vowinckel and Orvig, 1967).

The most frequently occurring profiles consist of a shallow layer with a negative gradient that is about two-thirds of the dry adiabatic, and extend from the surface to about 200-500m. Generally, this layer will be capped by an inversion layer of about 200m. Less frequently, the surface layer will be isothermal or have a positive gradient.

The relation between the temperature structure and the location of the stratus layers is very poorly documented. At best, surface observations with kites and balloons will yield only the location of the lowest base along with the temperature, while radiosondes and dropsondes give no information about the cloud structure at all. In principle, aircraft observations could give combined measurements of temperature and cloud structure, but it seems that only a single profile for Arctic stratus has appeared in the literature (Dergach et al., 1960).

The results of these various observations are summarized in Figs.1.9-1.10. The picture is confusing. In the Sverdrup data the lapse rate is always negative in the sub-cloud region, but the height of the base does not seem to relate to any structure in the temperature profile. The

Russian data indicate that the top of the stratus layer is close to the base of the inversion, and this is likely to be an accurate picture inasmuch as it agrees with our knowledge of mid-latitude stratus.

Some statistics on wind speed and direction were obtained over the pack ice during the Sverdrup expedition. The mean wind speed at anemometer level was 3.9m sec^{-1} , and deviated only slightly from the annual mean. The speed tended to be less than 6m sec^{-1} more than 80% of the time, and had a very small and irregular diurnal variation, consistent with the negligible temperature variation at the surface.

Near the coast, winds with a southerly component were associated with positive free air temperatures and light cloudiness, while winds from the pack ice were associated with zero degree temperatures and heavy cloud cover. This was reasonable, since the Siberian continent tended to be warm and free of low cloud, while the pack ice was cold and cloudy.

On the pack ice itself there was very little correlation between wind direction and either temperature or cloudiness, since air advected from any direction was uniformly cold and cloudy. Furthermore, the surface temperature showed only a small diurnal variation with a maximum amplitude of about 1°C , and did not vary markedly with cloud conditions.

1.2.4 Relative Humidity

Over the pack ice the surface layer is always very close to saturation with respect to liquid water. Sverdrup quotes the following mean relative humidities: May, 86.0%; June, 93.4%; July, 95.8%; August, 96.2%; September, 93.2%; October 85.3%. At coastal stations high relative humidities tended to occur with winds from the pack ice, and lower relative humidities with winds from the continents.

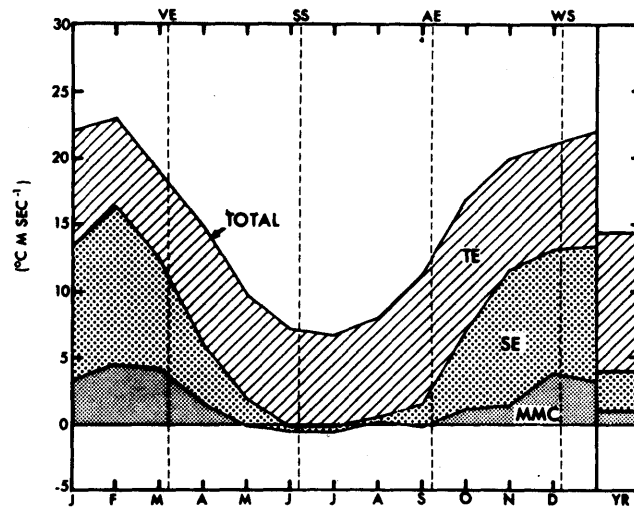


Fig. 1.7a Annual cycle of poleward flux of energy across 60°N by transient eddies (TE), stationary eddies (SE), and the mean meridional circulation (MMC) (after Oort, 1974).

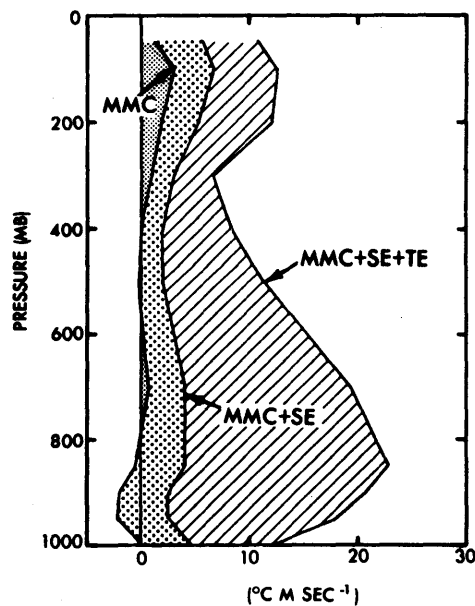


Fig. 1.7b Annual mean poleward flux of energy across 60°N by transient eddies, stationary eddies, and mean meridional circulation (after Oort, 1974).

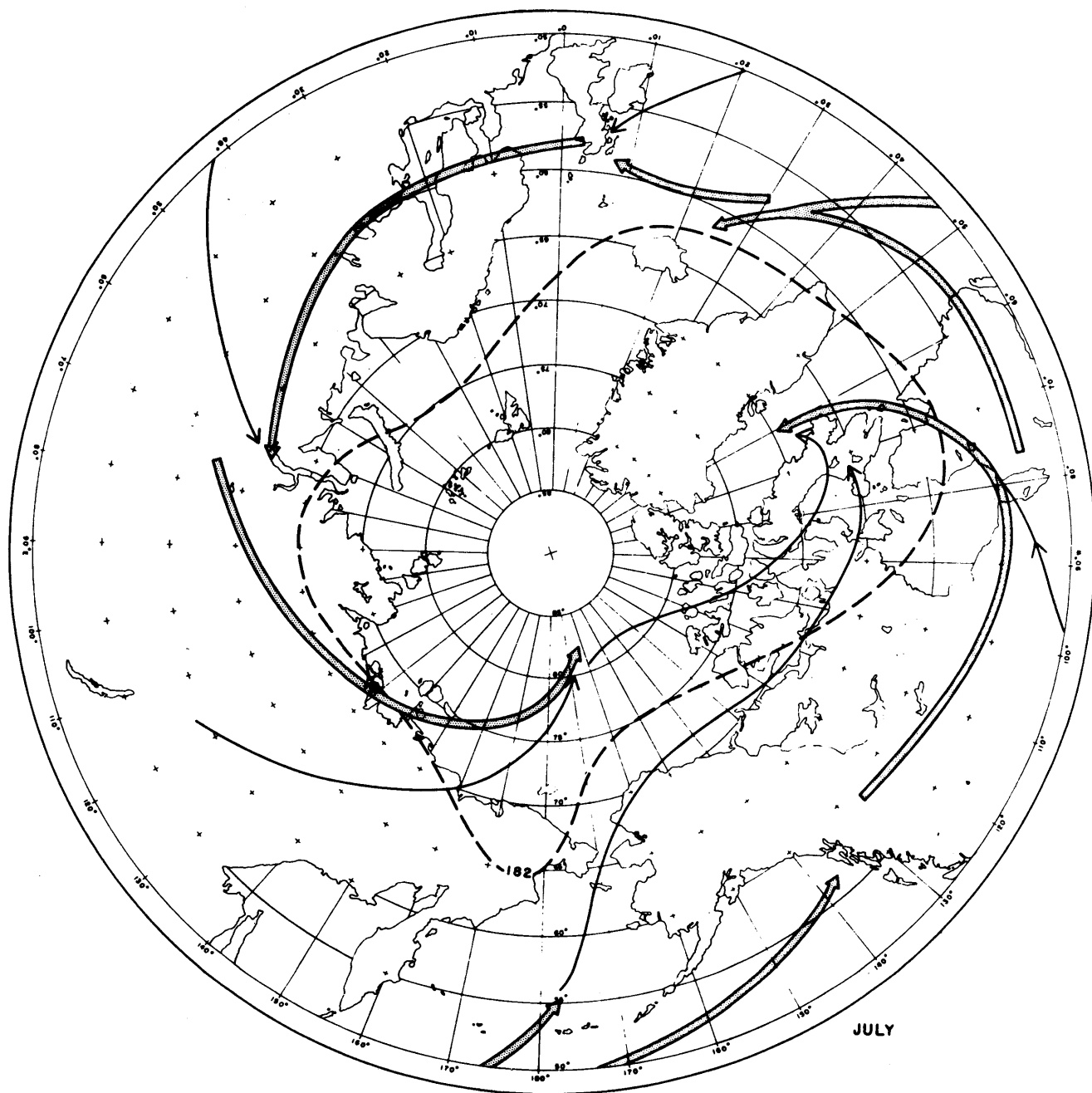


Fig. 1.8 Schematic diagram of cyclone behavior over polar areas in July (after Reed, 1959).

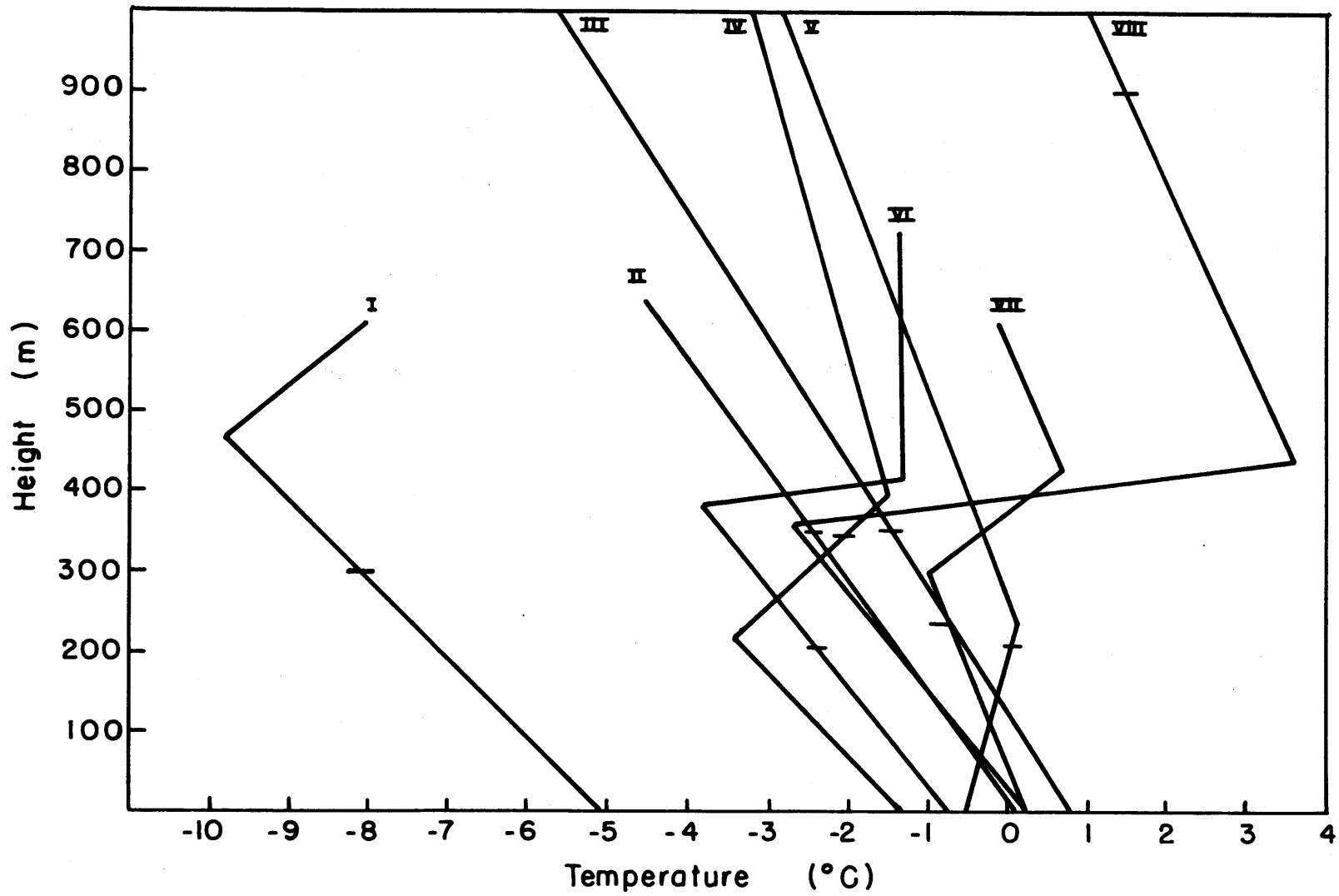


Fig. 1.9 Temperature profiles from selected kite and tethered balloon observations of Sverdrup. Tick marks on the temperature profiles indicate the base of the lowest stratus layer. (adapted from Sverdrup, 1933)

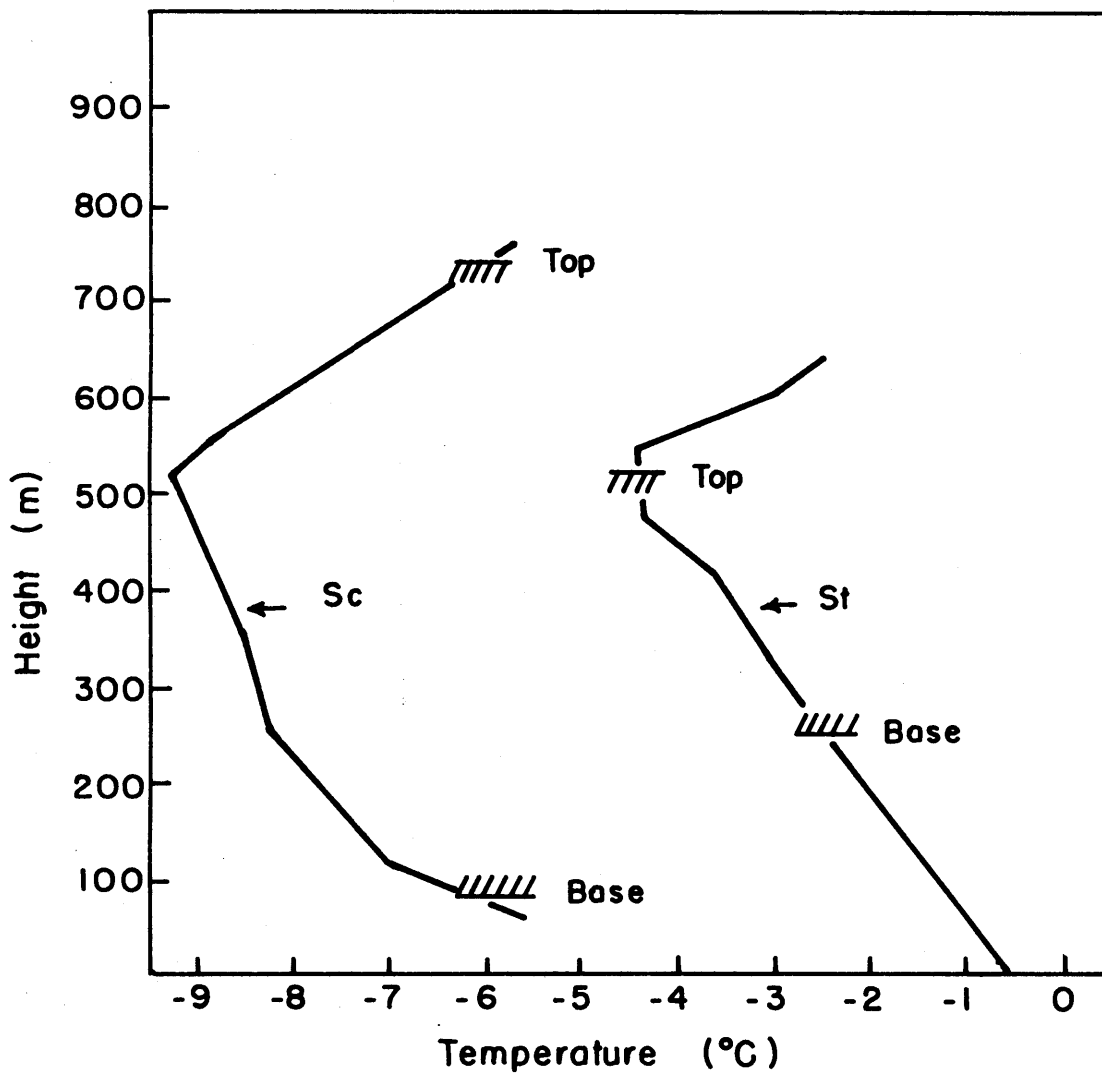


Fig. 1.10 Temperature profiles within Arctic stratus clouds (adapted from Dergach et al., 1960).

1.3 MACROMETEOROLOGICAL CONDITIONS

1.3.1 Heat and Moisture Fluxes at the Surface

Estimates of the fluxes of heat and moisture at the surface have been made by Badgley (1961), Vowinckel and Taylor (1965), and by several Russian investigators whose work was summarized by Fletcher (1965). The methods used to calculate the fluxes differ from author to author, and the results for some months do not even agree in sign. Most of the above authors, however, seem to indicate that the flux of latent heat is positive (upward) during most of the summer season, although the magnitude is relatively small since the mixing ratio in the surface layer is always close to its saturation value at 0°C.

The results of Badgley and of Vowinckel and Taylor show positive sensible heat fluxes at the beginning and at the end of the melting season, and negative (downward) fluxes in the middle. These results are consistent with the notion, first verified by the measurements of Sverdrup, that during the peak of the melting season the temperature of the surface is maintained near zero degrees, while air temperatures away from the surface are normally positive. Moreover, it is likely that the fluxes of heat and moisture will be progressively smaller toward the center of the pack ice, since large gradients of heat and moisture cannot be sustained over such an extensive horizontally homogeneous surface.

It is interesting that the minimum in the computed heat and moisture fluxes occurs at the same time that there is a very slight minimum in the low cloud amount in Huschke's atlas. A plausible explanation might be found by noting that Huschke's record of low cloudiness does not distinguish between stratus and stratocumulus type clouds, and the slight depression in the total cloudiness may reflect a decrease in the Sc component. This

would be consistent with the minimum in the sensible heat flux during mid-summer that has been calculated by Vowinckel and Taylor (1965) and others. It is also consistent with recent ice maps (British Met. Office, Climatological Service) which show that during July the area of the pack ice that is covered by surface air temperatures greater than 0°C attains its seasonal maximum.

We may note at this point that several authors (cf. Fletcher, 1965) have suggested that convective activity may be enhanced during the summer due to heating of meltwater ponds by the direct absorption of solar radiation. This effect, however, is likely to be negligible since we could not expect the ponds to become substantially warmer than 0°C . First, the juxtaposition of warm water and cold ice should be hydrodynamically unstable since melting at the edges of the ponds would give rise to horizontal temperature gradients. Moreover, the density of fresh water increases with temperature up to 4°C , and heating of the upper layers would actually increase vertical mixing, as illustrated by the experiments of Townsend (1964).

These assertions are supported by the observation (Doronin, 1969, p.205) that the temperature profile is nearly linear in meltwater ponds in the Soviet Arctic and that the surface temperature did not exceed 0.2°C in small ponds and 0.5°C in large ones. Preliminary results from the AIDJEX experiment (Untersteiner, personal communication, 1975) also indicated that 0.5°C was the maximum temperature to be found in meltwater ponds. It therefore appears that virtually all of the radiative energy absorbed by the water is used for ice melting and a negligible fraction is used to heat the water.

1.3.2 Thermodynamic State of the Lower Boundary

The Central Polar Ocean is icebound throughout the year, except during abnormally warm summers when the waters north of Spitzbergen or FranzJosef Land may be partially open. Of the peripheral oceans, only the Norwegian and Barents Seas are ice free throughout a normal year. The Kara, Laptev, East Siberian, Chukchi, and Beaufort Seas usually are icebound well into the spring, and may become open near their coasts during the summer, depending upon the input of warmer water from rivers or ocean currents. Roughly speaking, the isoline of 90% total cloudiness is coincident with the normal extent of 80-100% ice coverage in the Polar Ocean during July.

During the cold season the ice surface is covered with snow, and some small fraction of the ice exposes open water through leads, which are openings or cracks in the surface caused by a divergent low-level wind field. (We may note parenthetically that leads generate another form of condensation peculiar to the Arctic which is known as "Arctic sea smoke". Water evaporates from the surface of a lead at a very rapid rate since the saturation vapor pressure of the water is so much greater than that of the air. Condensation immediately occurs in the cold air, and may persist for a long period if a low inversion is present.)

With increased insolation, the snow cover and eventually the top layer of the sea ice begin to melt. The surface becomes quite heterogeneous, and consists of some combination of ablating ice and snow, fresh meltwater ponds and open ocean. From a thermodynamic viewpoint, slush, meltwater ponds and open ocean are indistinguishable insofar as they all represent a liquid source of water vapor at a temperature close to 0°C. The unmelted ice and snow may, in fact, represent a sink of water vapor,

owing to its depressed saturation vapor pressure at 0°C.

Clearly, the important question to decide is what fraction of the total ice area is liquid water. Vowinckel and Orvig (1970, p.138) imply values close to 30% in July and 20% in August. Untersteiner (1961) quotes a value of 30% at the peak of the melting season, while the Naval Atlas (U.S. Hydrographic Office, 1958) shows values as high as 70% in selected regions. The actual value is fairly important, since it will determine whether the summertime Arctic is, on the average, evaporative or condensative.

1.3.3 Main Characteristics of the Radiation Field

The most pronounced feature of the solar radiation field at high latitudes during the summer is stationarity, due primarily to the small diurnal variation of the solar zenith angle, which itself is always positive and less than 90°. This latter effect is illustrated in Fig.1.11a, which shows the duration of daylight as a function of latitude during the summer.

The minimum solar zenith angle is only 45° at the Arctic Circle at noon of the summer solstice, and drops to 66.5° at the pole. The midnight zenith angle on the same day is 90° at the Arctic Circle and 66.5° at the pole.

Actinometric studies indicate that the downward flux of radiation impinging on the ice surface during the summer consists of a very large diffuse component along with the direct beam. At Cape Chelyuskin, for example, the diffuse component averages about 83% of the total radiation at the surface during August (Gavrilova, 1963). Moreover, the diffuse component becomes larger as the albedo of the surface rises, owing to the increased number of reflections between the surface and the cloud layers.

This high figure is, of course, attributed to the frequent occurrence of Arctic stratus at Chelyuskin, which, according to the observations of Sverdrup, was 90-100% during August.

The flux of longwave radiation at the surface is determined mainly by the low temperatures and high cloudiness of the boundary layer. The net flux is diminished by the isothermal or inversion stratification that frequently occurs, and, in the presence of a stratus cloud located at or near the inversion, becomes negligibly small. In some cases negative (downward) net fluxes were measured at the surface (Gavrilova, 1963), although the net flux is always positive when averaged over any appreciable time period.

The net radiative heating of the Arctic atmosphere is normally everywhere negative (Rodgers, 1967; Dopplick, 1972). According to Rodgers, the mean heating rate at 70°N during July in the 1000-850mb layer is $+0.94 \text{ deg day}^{-1}$ in the NIR and $-1.77 \text{ deg day}^{-1}$ in the longwave.

Although several studies have been made of the radiative properties of mid-latitude stratus clouds (Neiburger 1949; Platridge, 1974), only one set of measurements on Arctic stratus has appeared in the literature (Koptev and Voskresenskii, 1962). These investigators measured the flux of solar radiation ($0.4 - 4.0\mu$) in and around a number of Arctic stratus clouds, their thickness, and also noted the state of the underlying surface. Liquid water contents and drop size distributions were also determined. The authors quoted fractional absorptances of 2-5% for a non-precipitating St cloud of depth 300-500m, and 4-10% for a non-precipitating Sc cloud of depth 200-500m. The "reflectivity" must be interpreted as the albedo of the cloud-plus-surface system since the investigators did not distinguish between radiation backscattered from the cloud and that reflected at the

surface. It varied with the depth of the cloud, the condition of the surface, and cloud microstructure, and some sample results are shown in Table 1.2.

Table 1.2
Radiation Measurements in Arctic Stratus
by Koptev and Voskresenskii

Depth (m)	Vol. conc. (cm ⁻³)	Mean Radius (μ)	Water conc. (g m ⁻³)	Surface	Reflectivity (%)
300	90.7	5.2	0.15	Ocean	69
400	18.1	7.1	0.10	Ocean	50
400	18.1	4.9	0.10	Ocean	50
400	17.7	5.1	0.011	Ocean	56

In a single layer that overlapped both ice and ocean, the reflectivity was near 30% over water, near 56% over 3-4 point ice, and 72% over 10-point ice.

1.3.4 Albedo

During the summer the surface albedo varies widely over the Polar Ocean. Freshly fallen snow has the highest reflectivity of about 80-85%. Chernigovskii (1963) obtained the following representative albedos from floating ice stations in the Central Arctic: Melting ice with melting snow, 68%; melting ice, 58-65%; pools of melt water, 33-36%; pools of melt water with ice and snow crust, 42-44%; refrozen ice, 70%; ice and snow, 75-80%.

1.4 CLOUD MICROPHYSICS

Drop size distributions and liquid water contents have been measured by a number of investigators. In addition to the results in Table 1.2, we also have the measurements given in Table 1.3.

Table 1.3
Observations of Mean Stratiform Cloud Properties
During Summer Conditions

	Liquid Water (g m^{-3})	Droplet Density (cm^{-3})	Diameter (μ)
Dergach <u>et al.</u> (1960) (Soviet Arctic)	.05-0.2 (st) 0.1-0.3 (sc)	-	14-20
Gathman and Larson (1974) (Surface fogs, Greenland Sea)	-	21	13.5
Weller <u>et al.</u> (1972) (Barrow)	-	-	13.5
Jayaweera and Ohtake (1973) (Barrow)	0.1-0.2	90	13.5
Kumai (1973) (Surface fogs, Barrow)	.05	15	15.6

A sample drop size spectrum is shown in Fig.1.11b. The particle sizes are similar to those found in mid-latitude St or Sc. The water concentrations, however, are somewhat smaller. Liquid water in mid-latitude stratus according to Neiburger is normally $0.1-0.7 \text{ g m}^{-3}$ while the concentrations found in the Arctic are only on the order of 0.1 g m^{-3} or less.

The concentration of ice crystals in Arctic stratus is extremely low, but is not zero. Jayaweera and Ohtake (1973) found ice crystal densities which increased from about 10^{-5} cm^{-3} at -10°C to about 10^{-3} at -20°C . In the same experiment ice nuclei concentrations were measured at a nearby surface station, and corresponded closely to the ice crystal concentration. This finding implies that the only source of ice crystals are the ambient ice nuclei, and the process of ice multiplication that occurs in mid-latitude convective clouds does not occur in Arctic stratus.

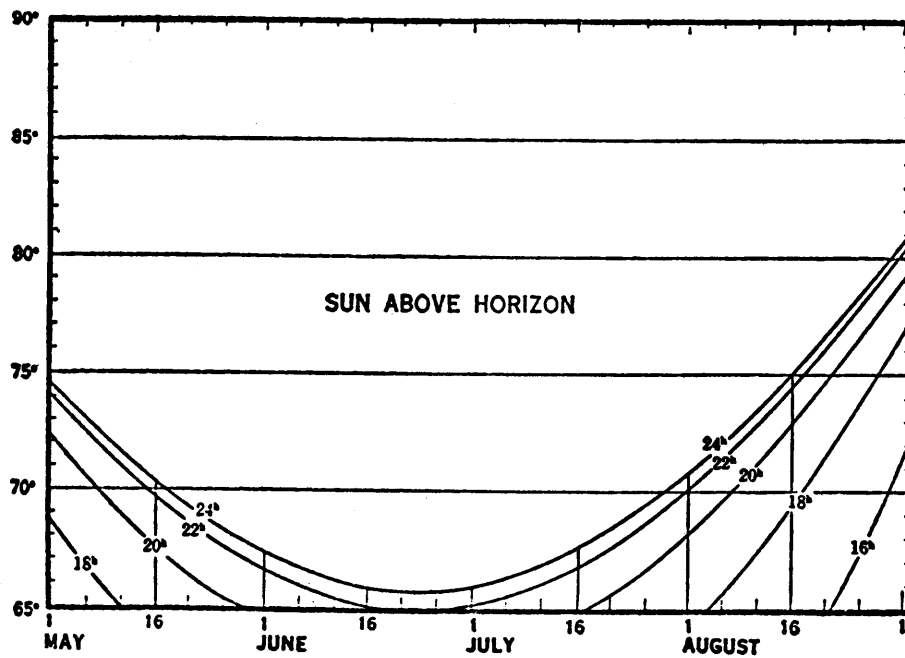


Fig. 1.11a Duration of daylight in the Arctic (from Smithsonian Meteorological Tables).

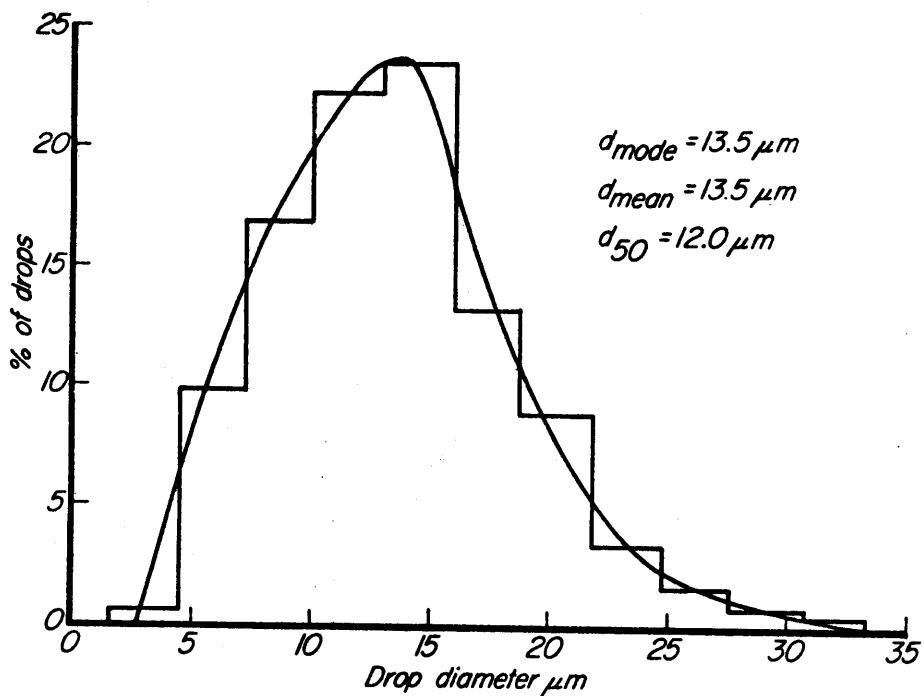


Fig. 1.11b Average drop size spectrum for Arctic stratus clouds (after Jayaweera and Ohtake, 1973).

2. STATEMENT OF PROBLEM AND METHOD OF SOLUTION

2.1 THE PROBLEM

We have been able to construct only a broad-brush picture of the summertime Arctic and the conditions of Arctic stratus due to the lack of observational data. However, the discussion of Chapter 1 does lead us to consider the following fundamental problems.

2.1.1 Structure and Mechanism

We know, in general, that fog and stratus occur when a layer of air with an adequate number of condensation nuclei is saturated either by cooling it to its saturation point, or by introducing more water vapor into it than it can accommodate at its ambient saturation temperature. But we do not know in a quantitative sense what contribution to the net cooling comes from radiation, and what comes from turbulent transports, or how much of the total water vapor is advected rather than evaporated from the surface.

The role of radiation in the development and maintenance of Arctic stratus and in layered clouds in general needs to be elucidated. It is possible that radiation may be the dominant control in some types of stratus, and the characteristic time- and length-scales over which radiative effects are important should be determined. We must discover which components of the radiation field, and which absorbers are the most important, and what is the nature of the "feedback" that occurs when a cloud perturbs the ambient temperature field.

If we have isolated the fundamental physical and dynamical processes that govern Arctic stratus, we should then be capable of explaining its peculiar structure. In particular, can the preferred distribution of

temperature and liquid water be explained, as well as the typical heights of the tops and bases, and the typical depths of isothermal and inversion layers? Finally, some explanation should be offered for the tendency of Arctic stratus to occur in well defined layers separated by clear interstices.

2.1.2 Geographic Distribution.

We must also seek to explain why these ubiquitous cloud layers appear to be limited to the polar oceans. This region in the summertime has features in its radiative regime, in the conditions of its lower boundary, and its mean circulation that are not encountered elsewhere. Some or all of these features combine to make Arctic stratus a basic part of the summertime Arctic climate. Moreover, a qualitative explanation should be offered for the characteristic horizontal scale of the decks, and any variability of cloudiness with respect to the distance from the pole or the coasts.

2.1.3 Seasonal Behavior.

The low cloudiness of the Arctic almost behaves as a step function in time, and this radical behavior needs to be explained. There are a number of interrelated quantities that show marked seasonal variation in the Arctic, such as the temperature of the lower boundary, the temperature contrast between the ice and the adjacent continents, the amount of solar radiation illuminating the Arctic, and a number of other boundary conditions such as the surface reflectivity and surface roughness. The seasonal variation of cloudiness is likely to be coupled to some combination of these parameters.

2.2 METHOD OF SOLUTION

2.2.1 General Discussion

One of the most striking features of the Arctic stratus problem is horizontal homogeneity. We have seen from the discussion in Chapter 1 that the low cloud conditions and thermal structure of the boundary layer do not show any significant point-to-point variation within the Arctic Basin, although sharp discontinuities are found near the coast lines of the North American and Eurasian continents. These properties are consistent with the classical definition of an air mass (Bergeron, 1928), and in fact, the summertime Arctic basin has been frequently referred to as the source region for "mAw" air (maritime Arctic air, warmer than the underlying surface) (Willett and Sanders, 1953; Berry et al.; Pettersen, 1956). A reasonable working hypothesis would be that stratus clouds are a basic state for maritime Arctic air in the summer. This means that in order to adequately characterize the thermodynamic structure of maritime Arctic air it is necessary to describe its conditions of low cloudiness, in addition to its stability and its vertical distribution of heat, momentum, and moisture. The problem is then one of determining how that basic state is generated and maintained.

We have seen that the more recent synoptic analyses of the summertime Arctic imply that it is a region of low pressure characterized by a well defined convergence of air streams into the Central Polar Ocean. Although detailed trajectory analyses have not been carried out on the synoptic data, the early results of Dzerdeevskii (1945, Figs.24-25), Berry et al., and more recently of Prik (1959) suggest that steady flows of warm air from continental Canada and Siberia that may persist for 5-6 days frequently occur. These appear to be associated with baroclinic disturbances

that form along the Arctic Frontal Zone. These results suggest that the source of maritime Arctic air is continental Arctic air (which, according to the standard definitions, is identical to continental polar air during the summer). This view is further supported by the analysis of Newell et al. (1972) and of Oort and Rasmussen (1971) both of which indicate that the eddy transports of heat and moisture are large and positive during the summer season, which means that northward moving parcels are associated with warmer than average temperatures, and southward moving ones with colder temperatures, and similarly for moisture.

We shall consider the modification of polar continental air as it streams over the pack ice due only to the influence of the lower boundary and radiative transfer. There are three conditions that must be satisfied for this approach to be valid.

First, the temperature of the lower boundary must remain fixed (Priestley, 1959, Ch.8). If a substantial fraction of energy that is transferred from the air to the surface is used to change the temperature of the surface, then the modification of the surface must be coupled to the modification of the air mass. This constancy of temperature is usually satisfied over the ocean since its heat capacity is large, and this allows for simple treatment of air mass modification over water, as illustrated by Burke (1945) and Asai (1967). Over melting ice this condition is particularly well satisfied since all of the heat is used to melt the ice and the surface remains near 0°C.

Second, the thermodynamics of the boundary layer must be effectively decoupled from the thermodynamics of the large-scale flow. This assumption was implicit in Deardorff's model of air mass modification (1967) and in the sea breeze model of Walsh (1974). Lilly (1968) parameterized

this effect by retaining a $w\partial\theta/\partial z$ term in his heat equation to represent the effect of subsidence.

This is a difficult requirement to satisfy since there are always large adiabatic heating and cooling rates associated with the vertical velocity fields of synoptic systems. However, there are two important observations which suggest that their effect is secondary to diabatic heating in the Arctic.

The first emerges from the Reed and Kunkel (1960) analysis of the Ptarmigan data, which showed that the cloudiness in the lowest 1500m averaged nearly 100 per cent, and showed only slight relationship to the prevailing synoptic pattern. The total cloudiness was perturbed over a surface occlusion, near the crest of wave, and in the southeast quadrant of a cold low, and certainly reflected the vertical motion fields of the disturbances. However, the fact that a uniform low cloud cover prevailed elsewhere implied that intense subsidence or rising motion was a very localized effect.

The second emerges from the analysis of Newell et al. (1974, Ch.7). These authors computed the contribution to the heat budget from diabatic and advective terms, including subsidence. During the summer at high latitudes the contribution from the vertical velocity term was so small that its sign appeared to be in doubt. Admittedly the fact that the mean vertical velocity field is small does not tell us anything about the typical vertical velocities in Arctic weather systems, as that requires a measure of the vertical velocity variance, which is not ordinarily available. However, it does imply that in some mean sense vertical velocity fields are less important for the summer climatology of the Arctic than they are in mid-latitudes or the tropics.

We therefore will not attempt to calculate explicitly the large-scale dynamical heating, and note that our results may not be representative of conditions where intense dynamical heating or cooling occurs. However, in some models we will attempt to parameterize this effect by retaining a $w\partial\theta/\partial z$ term in our heat equation, as did Lilly.

Finally, we require that the air which streams over the pack ice follow a trajectory that will keep it over the ice long enough for an equilibrium state to be established. The results of this calculation indicate that it takes 3-4 days for radiative-diffusive equilibrium between the air parcel and the lower boundary to occur. A crude trajectory analysis of the maps of Berry et al. indicated that it was not uncommon for parcels to meander about the polar basin for 5 days or more, which is sufficient time for quasi-steady conditions to be established.

2.2.2 Basic Equations

The steady state distribution of equivalent potential temperature θ_E and total water r in a moist Boussinesq atmosphere are given by

$$U_0 \frac{\partial \theta_E}{\partial x} = \frac{\theta_E}{\rho C_p T} Q_{\text{rad}} - \frac{\partial}{\partial z} (\overline{w' \theta'_E}) \quad (\text{heat}) \quad (2.2.1)$$

$$U_0 \frac{\partial r}{\partial x} = - \frac{\partial}{\partial z} (\overline{w' r'}) - w_f \frac{\partial r_\ell}{\partial z} \quad (\text{water}) \quad (2.2.2)$$

Here the advective terms have been linearized about some constant geostrophic current U_0 , Q_{rad} is the volume rate of radiative heating, w_f is the fall velocity computed from Stokes' law, r_ℓ is the mass mixing ratio of liquid water, and $(\overline{w' \theta'_E})$ and $(\overline{w' r'})$ are the turbulent fluxes of equivalent potential temperature and total water, respectively. It is demonstrated in Appendix A that the equivalent potential temperature is the appropriate conservative variable in a moist atmosphere.

We assume that the distribution of both liquid water r_l and water vapor r_v can be described by a single equation for the total water content r . This will be true only if the water droplets are transported in the same sense as the water vapor by the basic current and the turbulent eddies. The calculations of Matveev (1964) indicate that this is indeed the case. For droplets with a radius less than 40μ the so-called "fractional entrainment", which is a measure of the extent to which individual droplets follow the turbulent motions of the air, is nearly 100%.

The turbulent transport terms in (2.2.1) and (2.2.2) will be approximated as complicated functions of stability and wind shear, and for the purpose of estimating the wind profile in the boundary layer we include the momentum equations

$$U_0 \frac{\partial u}{\partial x} = f v - \frac{\partial}{\partial z} (\overline{w'u'}) \quad (2.2.3)$$

$$U_0 \frac{\partial v}{\partial x} = -f u - \frac{\partial}{\partial z} (\overline{w'v'}) \quad (2.2.4)$$

where f is the Coriolis parameter and u and v are departures from the invariant geostrophic winds U_0 and V_0 ($V_0 = 0$). The terms $\overline{w'u'}$ and $\overline{w'v'}$ represent the vertical turbulent transports of x-momentum and y-momentum, respectively. Equations (2.2.3) and (2.2.4) are coupled to the heat and moisture equations only through our parameterizations of turbulence in the surface layer and the Ekman layer. In both regions the transports will be functions of the velocity gradients $\partial u/\partial z$ and $\partial v/\partial z$, as well as of the gradients $\partial\theta_E/\partial z$ and $\partial r/\partial z$.

We transform the equations (2.2.1)-(2.2.4) from (x,z) space to (t,z) space with the substitution (Deardorff, 1967)

$$U_0 \frac{\partial}{\partial x} [] \equiv \frac{\delta}{\delta t} [] \quad (2.2.5)$$

where the "downstream derivative" $\delta/\delta t$ makes it possible to relate the change in time to the change experienced over the corresponding travel distance moving with the velocity U_0 . The equivalent system of equations corresponding to (2.2.1) - (2.2.4) is

$$\frac{\delta \theta_E}{\delta t} = \frac{\theta_E}{\rho C_T} Q_{rad} - \frac{\partial}{\partial z} (\overline{w' \theta_E'}) \quad (2.2.6)$$

$$\frac{\delta r}{\delta t} = -\frac{\partial}{\partial z} (\overline{w' r'}) - w_f \frac{\partial r_f}{\partial z} \quad (2.2.7)$$

$$\frac{\delta u}{\delta t} = f v - \frac{\partial}{\partial z} (\overline{w' u'}) \quad (2.2.8)$$

$$\frac{\delta v}{\delta t} = -f u - \frac{\partial}{\partial z} (\overline{w' v'}) \quad (2.2.9)$$

which is equivalent to a one-dimensional time dependent system of equations. We solve (2.2.6) - (2.2.9) numerically in the domain $t=0$ to some $t=t^*$ and from $z=0$ to $z=2050\text{m}$, where the upper limit of z is chosen to be slightly greater than the characteristic vertical scale of Arctic stratus.

Although equations similar to (2.2.6) - (2.2.9) have been used in a number of other studies it is well to keep in mind that they are valid in most, but not all regions of (t,z) space. In particular, the advective terms can be linearized only if

$$\left| u \frac{\partial \theta_E}{\partial x} \right| \ll \left| U_0 \frac{\partial \theta_E}{\partial x} \right| \quad (2.2.10)$$

and similarly for the r , u , and v equations. Close to the surface the departure from U_0 will be large since we require $(U_0 + u) = 0$ at $z=0$. If the horizontal gradient of θ_E is also large, then (2.2.10) will not be satisfied, and our results may not be strictly representative of conditions in that region. However, u will be largest in the surface layer, which extends to about 25 m, and it will be shown in Sect.4.1.4 that the

largest gradients will occur within the first 18 hours of transit. These limits define a very small quadrant of the total (t,z) domain, and we accept this small error in order to retain the simplicity of (2.2.6)-(2.2.9).

2.3 PREVIOUS RELEVANT INVESTIGATIONS

There have been a number of attempts in recent years to construct cloud models in which there is some interaction between the fields of temperature and liquid water and the streams of short- or long-wave radiation. The earliest and most complete works are those of Feigel'son (1964, 1970). Feigel'son has considered in some detail the short- and long-wave properties of stratus and stratocumulus clouds, and has also constructed a number of models which predict the non-steady thermal structure of a cloudy atmosphere. She has also illustrated the important role that long-wave emission plays in maintaining an inversion above the cloud layer. Her results for stratus clouds are unrealistic, however, in that they predict that the entire troposphere should fill with liquid water as a result of thermal cooling.

Gierasch and Goody (1968) constructed numerical models of the Venus atmosphere under strongly convective conditions. Clouds occurred as a result of local supersaturation, and were permitted to interact with the fields of planetary radiation and also the solar radiation which drove the convection. A condensate was sought which would both be consistent with spectroscopic observations of the planet as well as be transparent enough to allow enough radiation to reach the surface to drive the convection to support that condensate.

Lilly (1968) expanded the mixed-layer theory of Ball (1960) to the problem of a moist marine layer, and retained a radiative term in his

heat balance equation, although he did not solve explicitly for it as a time-varying quantity. The results imply that the intense inversion frequently found off the coast of California is largely maintained by the radiative cooling of the cloud layer beneath that inversion.

Zakharova (1971), Zdunkowski and Barr (1972), and Pilie et al. (1975) each constructed diffusive models of nocturnal radiation fogs in which the radiative flux divergence was computed at each time step in a time-marching problem.

Knollenberg (1972) noted that heating rate calculations in the vicinity of a cloud need to be adjusted to account for the gain or release of latent heat resulting from radiatively initiated condensation or evaporation.

Paltridge (1974) formulated a heuristic model for a turbulent stratocumulus layer. A steady state was assumed to be maintained by radiation and evaporation from the cloud top balanced by entrainment at the boundaries. The author obtained the peculiar result that radiative cooling acts to dissipate stratocumulus, and also that stratocumulus should grow thicker during the day and become more tenuous at night. His result is quite contrary to actual observations of the life-cycle of Sc-type clouds.

3. PARAMETERIZATIONS

3.1 PARAMETERIZATIONS OF TURBULENCE

3.1.1 The Surface Layer

The transfers of heat, momentum and moisture in the surface layer are computed using the similarity hypothesis of Monin and Obukhov (1954). Under steady and horizontally homogeneous conditions, and assuming that the variations with height of the fluxes of heat, momentum and moisture are small enough to justify treating them as constants, the vertical profiles of temperature, wind, and specific humidity are "universal" functions of the non-dimensional parameter z/L , where z is the height and L is the Obukhov length

$$L = -\frac{\theta}{g} \frac{U_*^3}{k_0 (\overline{w'\theta'})_0} \quad (3.1.1)$$

where U_* is the friction velocity, g/θ is a buoyancy parameter, k_0 is the von Karman constant (equal to 0.4) and $(\overline{w'\theta'})_0$ is the surface temperature flux. The mean gradients are given by

$$\frac{k_0 z}{U_*} \frac{\partial U}{\partial z} = \phi_m(z/L) \quad (3.1.2)$$

$$\frac{k_0 z}{\theta_*} \frac{\partial \theta}{\partial z} = \phi_h(z/L) \quad (3.1.3)$$

$$\frac{k_0 z}{r_{v*}} \frac{\partial r_v}{\partial z} = \phi_r(z/L) \quad (3.1.4)$$

where ϕ_m , ϕ_h and ϕ_r are functions describing the non-dimensional profiles of wind, temperature, and specific humidity, respectively. θ_* is a characteristic temperature and r_{v*} is a characteristic specific humidity. U is the resultant wind speed in the surface layer. Moreover, if the profiles of heat and moisture are themselves similar as the measurements of Dyer

(1967) indicate, and with $\phi_h = \phi_r$, equations (3.1.3) and (3.1.4) can be combined into a single equation for the virtual potential temperature, θ_v ,

$$\frac{k_0 z}{\theta_{v*}} \frac{\partial \theta_v}{\partial z} = \phi_h(z/L) \quad (3.1.5)$$

where θ_{v*} is now a characteristic virtual potential temperature. The Obukhov length L is also re-defined to include the effect of water vapor on the buoyancy flux into the surface layer:

$$L = - \frac{\theta_v U_*^3}{g k_0 (\overline{w' \theta_v'})_0} \quad (3.1.6)$$

That the virtual potential temperature should appear in the definition of the Obukhov length follows from consideration of moisture fluctuations in the turbulent kinetic energy equation of the Boussinesq system. Furthermore, we will ignore the contribution of liquid water in our definition of the virtual potential temperature, since both the observations of Arctic stratus as well as the results of this calculation indicate that the liquid water concentrations are small. We have,

$$\theta_v = \theta (1 + 0.6 r_v) \quad (3.1.7)$$

$$\approx (\theta_\epsilon - \frac{L_v r_v}{C_p}) (1 + 0.6 r_v) \quad (3.1.8)$$

where L_v is the latent heat of vaporization of water at 273 K.

The forms of ϕ_h and ϕ_m which we use are due to Businger (1973):

$$\left. \begin{aligned} \phi_h &= 0.74 (1 - 9 z/L)^{-1/2} \\ \phi_m &= (1 - 15 z/L)^{-1/4} \end{aligned} \right\} \frac{z}{L} \leq 0 \quad (3.1.9)$$

$$\left. \begin{aligned} \phi_h &= 0.74 + 4.7 z/L \\ \phi_m &= 1 + 4.7 z/L \end{aligned} \right\} \frac{z}{L} > 0 \quad (3.1.10)$$

$$\left. \begin{aligned} \phi_h &= 0.74 + 4.7 z/L \\ \phi_m &= 1 + 4.7 z/L \end{aligned} \right\} \frac{z}{L} > 0 \quad (3.1.11)$$

$$\left. \begin{aligned} \phi_h &= 0.74 + 4.7 z/L \\ \phi_m &= 1 + 4.7 z/L \end{aligned} \right\} \frac{z}{L} > 0 \quad (3.1.12)$$

Eq.(3.1.9) represents a $-1/2$ power law for the convective temperature gradient, and appears to give a better representation of real data than the $-1/3$ power law of Priestley (1959) and others. Eqs.(3.1.11) and (3.1.12) are the familiar log-linear profiles for the stable case.

Values of U and θ_v at any height z in the surface layer are obtained by integrating (3.1.2) and (3.1.5) from z_0 to z :

$$\frac{k_0}{U_*} [U(z) - U(z_0)] = \int_{z_0}^z \phi_m(z/L) dz \quad (3.1.13)$$

$$\frac{k_0}{\theta_{v*}} [\theta_v(z) - \theta_v(z_0)] = \int_{z_0}^z \phi_h(z/L) dz \quad (3.1.14)$$

where z_0 is the surface roughness. The integrals on the right side of (3.1.13) and (3.1.14) have been computed by Paulson (1970). Denoting them as I_m and I_h , respectively, we have for $z/L \leq 0$,

$$I_m = \ln z/z_0 - \Psi_1 \quad (3.1.15)$$

$$\text{where } \Psi_1 = 2 \ln \frac{1+x}{2} + \ln \frac{1+x^2}{2} - 2 \tan^{-1}(x) + \frac{\pi}{2} \quad (3.1.15a)$$

$$\text{where } x = \phi_m^{-1} \quad (3.1.15b)$$

$$I_h = 0.74 (\ln z/z_0 - \Psi_2) \quad (3.1.16)$$

$$\text{where } \Psi_2 = 2 \ln \frac{1+y}{2} \quad \text{and } y = 0.74 \phi_h^{-1} \quad (3.1.16a)$$

For $z/L > 0$,

$$I_m = \ln z/z_0 + 4.7 z/L \quad (3.1.17)$$

$$I_h = 0.74 \ln z/z_0 + 4.7 z/L \quad (3.1.18)$$

With z_0 specified in advance, and $\theta_v(0)$ given as a boundary condition, (3.1.13) and (3.1.14) constitute two equations in the two

unknowns θ_{v*} and U_* , since values for $\theta_v(z)$ and $U(z)$ are computed by the model. We can write

$$k_0 \Delta U / U_* = I_m(z/L) \quad (3.1.19)$$

$$k_0 \Delta \theta_v / \theta_{v*} = I_h(z/L) \quad (3.1.20)$$

Dividing (3.1.20) by the square of (3.1.19) and multiplying through by gz/θ_{v_0}

$$\frac{gz}{\theta_{v_0}} \frac{\Delta \theta_v}{\Delta U^2} = \frac{k_0 gz}{\theta_{v_0}} \frac{\theta_{v*}}{U_*^2} I_h I_m^{-2} \quad (3.1.21)$$

The left hand side of (3.1.21) is a bulk Richardson number Ri_B , and with the definition of L given in (3.1.6) we have

$$Ri_B = (z/L) I_h(z/L) I_m^{-2}(z/L) \quad (3.1.22)$$

which can be solved in advance to yield a table of Ri_B as a function of z/L . If we then define drag coefficients for heat and momentum of the form,

$$C_\theta = \frac{\theta_{v*}}{\Delta \theta_v} \quad \text{and} \quad C_u = \frac{U_*}{\Delta U} \quad (3.1.23)$$

we can use (3.1.19) and (3.1.20) to define a one-to-one relationship between the drag coefficients and Ri_B .

This parameterization for the surface layer in many respects parallels that of Deardorff (1971) for the entire planetary boundary layer.

Ri_B is plotted as a function of z/L in Figure 3.1. At large positive values of z/L , Ri_B approaches a value, which according to (3.1.17) and (3.1.18) is equal to 0.21 (or $1/4.7$). This reflects the well known fact that under strongly stable conditions buoyancy forces completely

suppress turbulence that is generated by the Reynolds stresses, and this occurs near $Ri_B = \frac{1}{4}$. In our model we effectively shut off all turbulence in the surface layer at $Ri_B = .21$. Radiative transfer is the only mode of energy transport left at that time.

C_θ and C_u are plotted as a function of Ri_B for several values of z/z_o in Figs.3.2a and 3.2b. The drag coefficients slowly increase with $-Ri_B$ in the convective atmosphere, reflecting the $-1/2$ and $-1/4$ power laws of ϕ_h and ϕ_m . In the stable case, they decrease uniformly to zero at $Ri_B \sim .2$, again indicating that all surface layer fluxes become zero with intense stability.

Large positive values of Ri_B are not uncommon in the summertime Arctic. Businger and Arya (1974) present data which imply values of the flux Richardson number

$$R_f = \frac{g}{\theta} \frac{\overline{w'\theta'}}{\overline{w'u'} \left| \frac{\partial u}{\partial z} \right|} \quad (3.1.24)$$

of about +1 at 3m from measurements taken in the Soviet Arctic in July 1970. It is easy to show that $R_f = z/L\phi_m^{-1}$, so that combining (3.1.24) and (3.1.21) we have $Ri_B = R_f\phi_m(z/L)I_h I_m^{-2}$, which for large z/L implies $Ri_B \sim R_f$. These data consequently describe the laminar region that we have been discussing.

Equation (3.1.23) is used to compute the fluxes of momentum, heat and moisture through the surface layer required by (2.2.6) - (2.2.9)

$$\text{Momentum:} \quad \tau = \rho_0 U_*^2 \quad (3.1.25)$$

$$\text{Heat:} \quad \overline{w'\theta'} = -U_* \theta_* \quad (3.1.26)$$

$$\text{Moisture} \quad \overline{w'r_v'} = -U_* r_{v*} \quad (3.1.27)$$

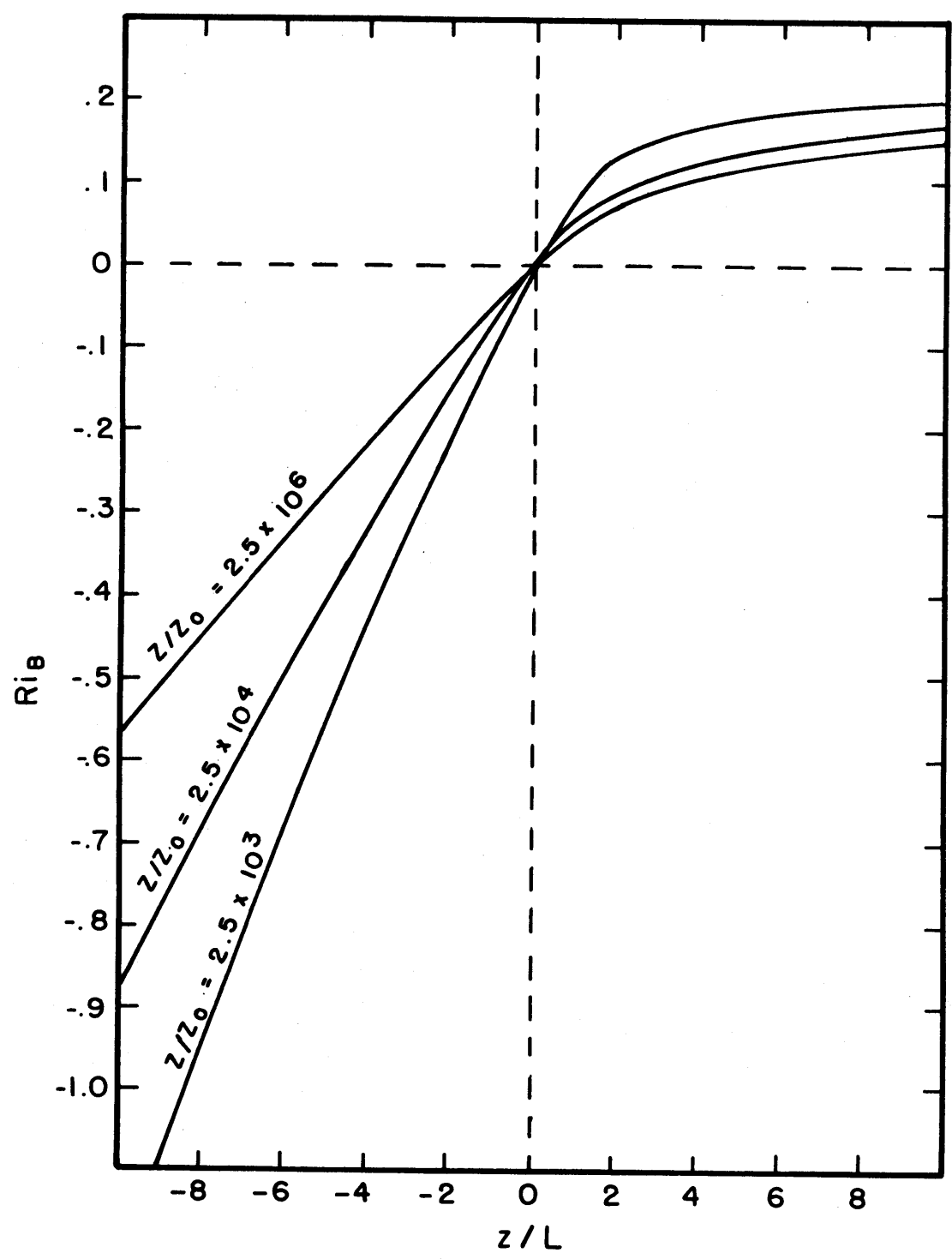


Fig. 3.1 Bulk Richardson number Ri_B as a function of z/L for several values of z/z_0 tested in the model.

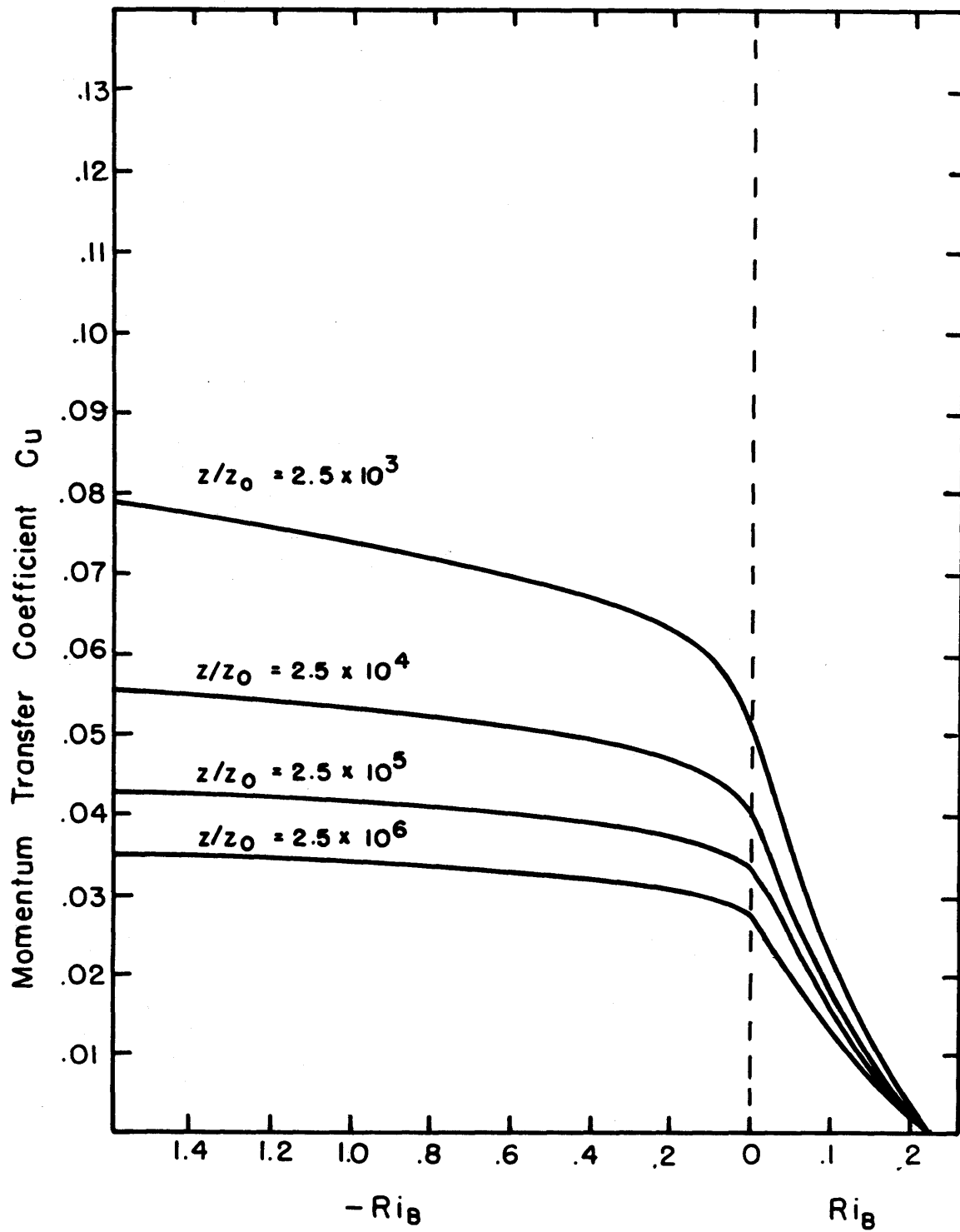


Fig. 3.2a Momentum transfer coefficient as a function of Ri_B .

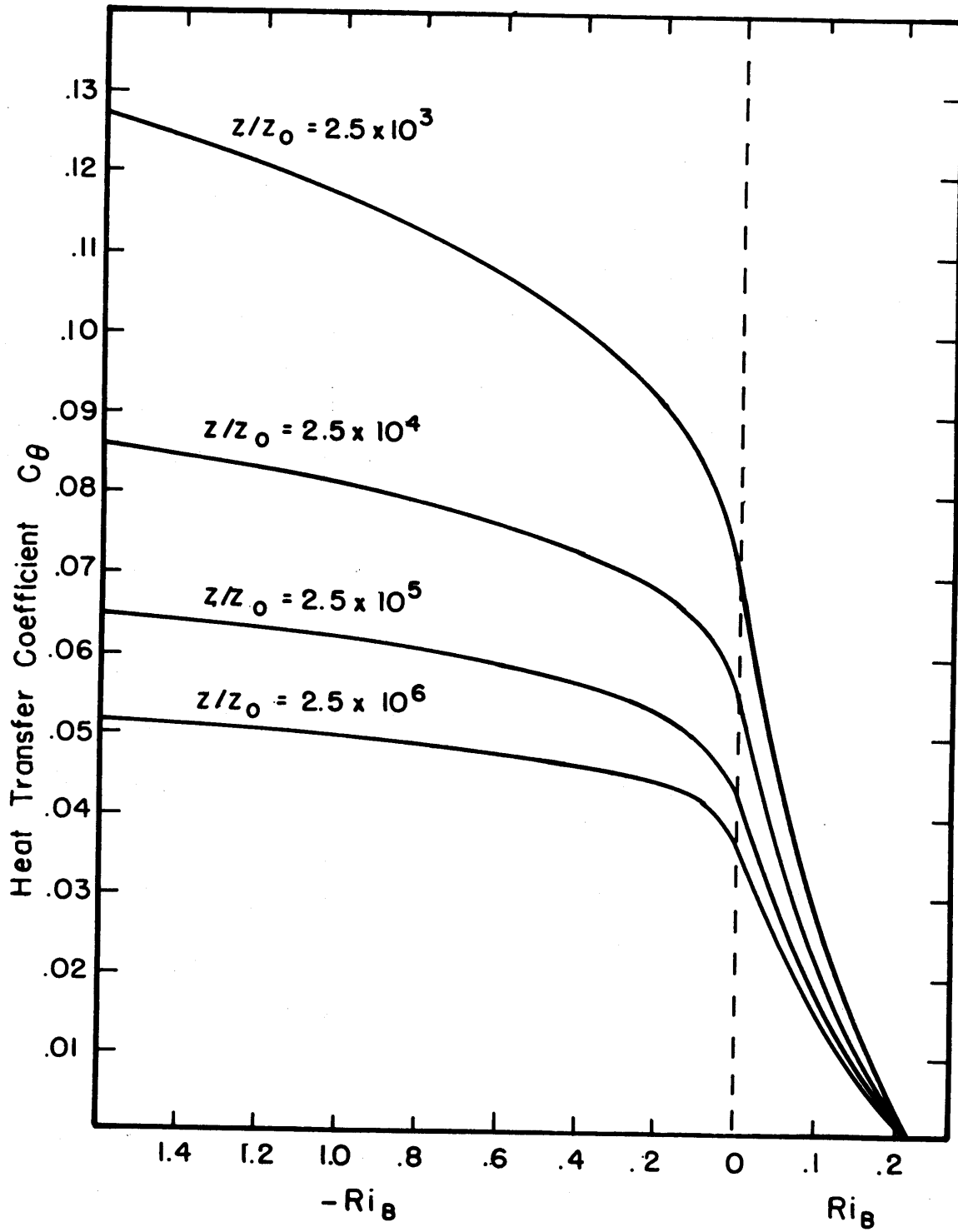


Fig. 3.2b Heat transfer coefficient as a function of Ri_B .

We convert the fluxes of potential temperature and moisture into fluxes of virtual potential temperature and equivalent potential temperature from the definitions (3.1.7) and (3.1.8):

$$\overline{w'\theta'_v} = \overline{w'\theta'} + 0.622 \bar{\theta} \overline{w'r'_v} \quad (3.1.28a)$$

$$\overline{w'\theta'_e} = \overline{w'\theta'} + \frac{L_v}{c_p T_0} \overline{w'r'_v} \quad (3.1.28b)$$

3.1.1.1 Surface Roughness

We use a range of roughness lengths z_0 to test the model's sensitivity to this parameter. Average roughness length over the pack ice vary from 0.02 cm (Untersteiner and Badgley, 1965) to 0.40 cm (Smith et al., 1970).

3.1.2 Effects of Horizontal Inhomogeneity and Radiative Transfer

The first inconsistency which arises in attempting to study the modification of a radiatively active surface layer with similarity theory stems from the assumption of horizontal homogeneity. At all times $t < 0$ the surface layer will be in equilibrium and have characteristic values of U_* and θ_{v*} corresponding to the initial values of the surface roughness and the fluxes of temperature and moisture. At $t=0$ the surface layer effectively undergoes step-function changes in surface roughness and surface temperature corresponding to the changes which would occur as an air mass moved from the continental Arctic out over the Polar Ocean or pack ice.

If the surface layer responded fast enough to the changes in the lower boundary, no problem would arise. However, the results of Shir (1972) for flow over a changed surface roughness, and those of Taylor (1971) for flow over a changed surface heat flux indicate that this is not the case. The downstream height-to-fetch ratio, which is an indication

of how rapidly equilibrium is re-established, was found to be about 1/100 in the former calculation and about 1/300 in the latter. Stated otherwise, this means that a downstream fetch of about 30 km (or a horizontal transit time of about an hour) is required for the boundary layer to adjust to a large change in the surface heat flux.

Since we view the problem of non-homogeneity as being outside the scope of this work, we simply will assume that the transient conditions can be approximated as a series of equilibrium states. That is, at all times after $t=0$, we assume local similarity corresponding to the current values of z_0 , g/θ , U_* and $(\overline{w'\theta'})_0$.

Radiative transfer affects the validity of the similarity hypothesis in two ways. On a microscale radiation tends to alter the lifetimes of the eddies themselves, while on a macroscale large flux divergences give rise to heating or cooling which may violate the constraint of stationarity.

The former process is visualized by considering a radiating parcel of air that is displaced in a stably stratified atmosphere. Since the character of radiation is to destroy temperature anomalies, the parcel will be acted upon by a weaker restoring force than would a non-radiating parcel. Similarly, a radiating parcel would be subjected to a weaker acceleration in an unstable atmosphere. Radiation therefore tends to make a stable layer less stable, and an unstable layer less unstable. The stable case has been treated in detail by Townsend (1958), and also by Brutsaert (1971), and the unstable case by Goody (1956).

We can judge the relative importance of radiation and turbulence in destroying temperature anomalies by comparing the characteristic time scales over which they act. The process with the shorter time scale will

dominate.

If q is a characteristic turbulent velocity scale and ℓ is the dominant eddy size, the Taylor (1935) hypothesis is that the energy dissipation rate ϵ is given as $\epsilon \sim q^3/\ell$. This is a statement that the largest eddies should give up most of their kinetic energy q^2 during the period of one rotation, ℓ/q . We define ℓ/q as the turbulent lifetime of an eddy τ_t .

In a convective atmosphere ℓ is the height z , and scale analysis (cf. Wyngaard, 1973) indicates that $q \sim (zg(\overline{w'\theta'})_o/\theta)^{1/3}$ so that

$$\tau_t = \left[\frac{\theta}{g} z^2 / (\overline{w'\theta'})_o \right]^{1/3} \quad (3.1.29)$$

In a stable atmosphere the characteristic velocity $q \sim U_*$. However z is no longer the characteristic length since the strong restoring forces imposed by the positive potential temperature gradient place an upper limit on ℓ . In fact, this limit is the Obukhov length L . A parcel will be displaced some distance ℓ until all of its kinetic energy has been converted into potential energy. At equilibrium

$$\frac{g}{\theta} \frac{\partial \theta}{\partial z} \ell^2 \sim q^2$$

Since $\partial \theta / \partial z = \phi_h \theta_* / (k_o z)$ by the Monin-Obukhov hypothesis, we have

$\ell^2 \sim (z/L) \phi_h^{-1} L^2$, if we assume that $q^2 \sim U_*^2$. At large z/L this implies

$\ell \sim L$ since $\phi_h = 0.74 + 4.7(z/L)$. Thus in the stable case we can write

$$\tau_t = L / U_* \quad z > L \quad (3.1.30a)$$

$$\tau_t = z / U_* \quad z \leq L \quad (3.1.30b)$$

In the neutral case $q \sim U_*$, $\ell \sim z$, and $\tau_t \sim z/U_*$.

The turbulent lifetimes for the unstable, neutral and stable regimes are shown as a function of the height z for a typical value of U_* (30 cm sec^{-1}) in Fig.3.3. For all reasonable values of the turbulent heat flux, which we have characterized by several values of L , the turbulent lifetimes are at least two orders of magnitude shorter than the radiative lifetimes for a given length scale. The radiative lifetimes were computed by Goody (1964, Table 9.3).

Under convective conditions (L negative) the lifetimes become shorter with increasing instability (L decreasing), and under stable conditions they become shorter with increasing stability. In either case radiation has very little time to act: In the first case it is because the eddies have been dissipated by viscosity, and in the second case it is because the vertical excursion of a displaced eddy is so brief. We therefore conclude that radiative damping is negligible in this problem.

We may note that these results differ somewhat from the results of Goody (1964, p.369), where the author concluded that radiation should be more important in destroying temperature anomalies than we have estimated in the present study. Goody argues that radiation should increase the critical Richardson number for the onset of turbulence by a factor of 2.6 for eddies of size less than 1 m. The present analysis yields a factor of only 1.1. The difference arises because we have assumed longer radiative lifetimes. Goody has estimated a radiative lifetime of a 1 m eddy of 10^2 sec in his discussion, whereas we use the value 3.1×10^3 sec. This latter value was obtained from Goody's Table 9.3, and is more representative of a cold, relatively dry Arctic atmosphere.

The constraint of stationarity will be violated if radiative heating or cooling alters the stratification of the surface layer so rapidly

that the turbulence can never adjust itself to the new temperature profiles. Here the relevant time constants are the turbulent lifetimes that were discussed in the previous paragraphs, and a time scale which characterizes the radiative cooling of the whole surface layer.

In a later chapter it will be shown that we can approximate the longwave cooling equation by one that contains terms representing only exchange with space and exchange with a lower boundary:

$$\rho_w c_p \left(\frac{\partial T}{\partial t} \right)_{space} = -\pi \rho_w B(z) \epsilon'(u_\infty^*) \quad (3.1.31)$$

$$\rho_w c_p \left(\frac{\partial T}{\partial t} \right)_{bound} = -\pi \rho_w \epsilon'(u_u^*) (B_0 - B(z)) \quad (3.1.32)$$

where ρ_w is the density of water vapor; $\epsilon'(u_\infty^*)$ is the derivative of the water vapor emissivity for the absorber amount u^* between z and infinity; $\epsilon'(u_u^*)$ is the derivative for the absorber amount u^* between z and the boundary; and B is the Planck function, $\sigma T(z)^4/\pi$. The solutions to (3.1.31) and (3.1.32) define exponential decay times.

$$\tau_{rad}^{space} = \left[\frac{\rho_w \epsilon'(u_\infty^*) 4\sigma \bar{T}^3}{\rho_w c_p} \right]^{-1} \quad (3.1.33)$$

$$\tau_{rad}^{bound} = \left[\frac{\rho_w \epsilon'(u_u^*) 4\sigma \bar{T}^3}{\rho_w c_p} \right]^{-1} \quad (3.1.34)$$

At some arbitrary height in the surface layer, say 10m, we have $\rho_w \sim 3 \times 10^{-6}$, $\bar{T} \sim 273^\circ$, $u_\infty^* \sim .5 \text{g cm}^{-2}$, $u_u^* \sim .003 \text{g cm}^{-2}$. With $\epsilon'(u_\infty^*) \sim .2 \text{cm}^2 \text{g}^{-1}$ and $\epsilon'(u_u^*) \sim 17 \text{cm}^2 \text{g}^{-1}$, $\tau_{rad}^{space} \sim 17$ days and $\tau_{rad}^{bound} \sim .2$ days.

Both time constants are several orders of magnitude longer than the turbulent lifetimes discussed earlier. Stationarity is therefore not affected by longwave exchange.

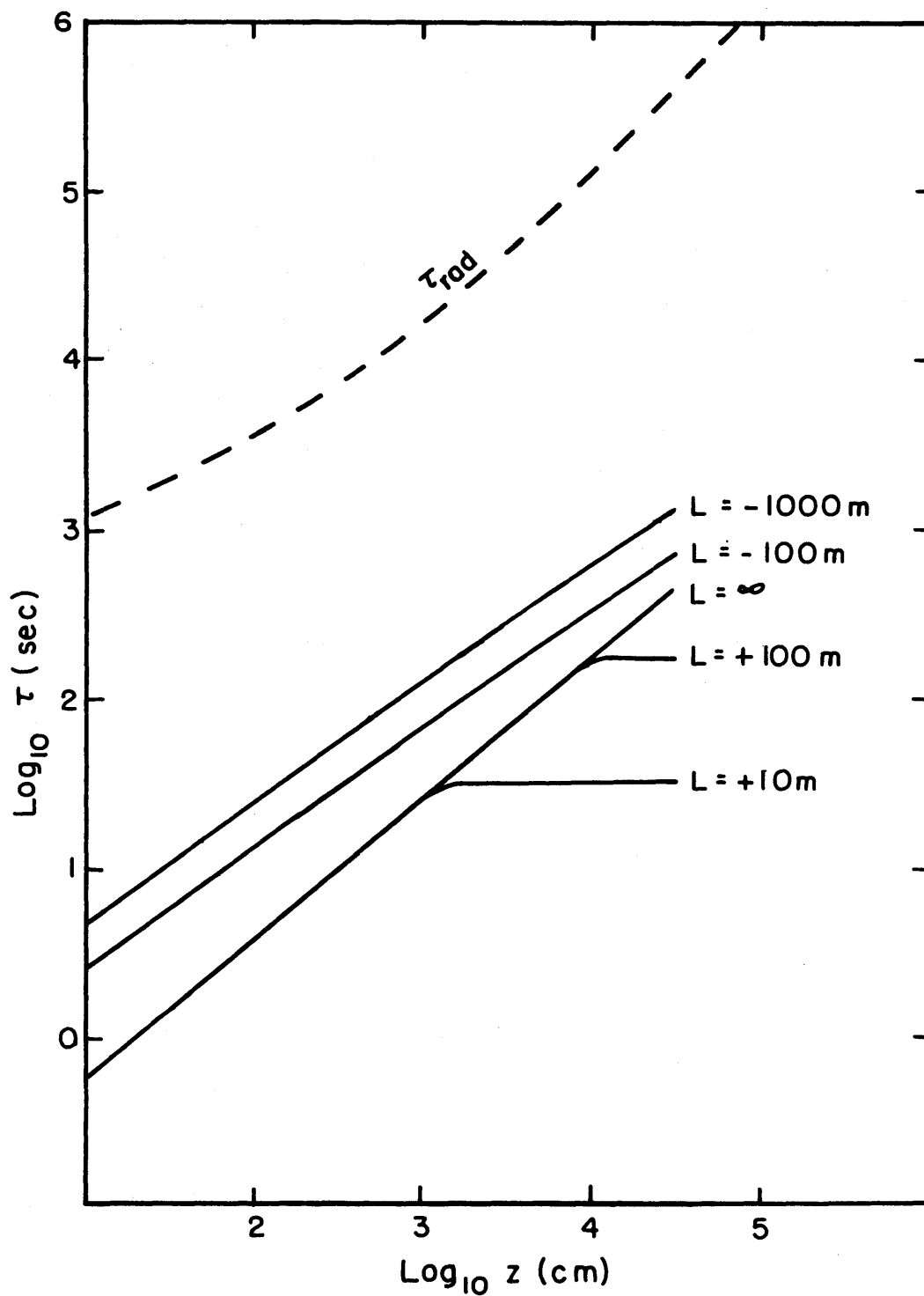


Fig. 3.3 Radiative and turbulent lifetimes as a function of vertical scale z . Turbulent lifetimes are shown as a function of the Obukhov stability parameter L .

This result does not contradict the findings of Robinson (1950) and others that large flux divergences on the order of a degree per hour do occur in the surface layer; it merely states that they do not affect the structure of the turbulence.

3.1.3 Turbulence above the Surface Layer

3.1.3.1 Neutral or Stable Cases

It is more difficult to parameterize the turbulent transports throughout the rest of the Ekman layer than it is in the surface layer mostly due to the fact that there is no adequate set of data from which a self-consistent theory can be constructed. Although there have been attempts to extend similarity theory up to the gradient wind level (Zilitinkevich et al., 1967) we will use the simplest formulations that are available. Our view is that a complicated turbulence formulation will make it more difficult to elucidate the highly non-linear effects of radiative transfer in this model.

We use a simple eddy diffusion parameterization whereby

$$\overline{w'\theta'_E} = -K(z) \partial\theta_E/\partial z \quad (3.1.35)$$

$$\overline{w'r'} = -K(z) \partial r/\partial z \quad (3.1.36)$$

$$\overline{w'u'} = -K(z) \partial u/\partial z \quad (3.1.37)$$

$$\overline{w'v'} = -K(z) \partial v/\partial z \quad (3.1.38)$$

The mixing coefficients $K(z)$ are height dependent and are computed from simple mixing length models. Since it is likely that turbulence will be enhanced in an unstable atmosphere, damped in a stable one, and be larger in one with large vertical wind shear, we modify $K(z)$ to take these factors

into account. Several formulations are tested in order to satisfy ourselves that the model is not highly sensitive to the form of $K(z)$ that is used.

We do not distinguish between the exchange coefficients for heat, momentum and moisture in (3.1.35)-(3.1.38). This is likely to be an oversimplification, but the crude method used to compute $K(z)$ in this region does not warrant such detail.

The mixing length in the Ekman layer is obtained from Blackadar (1962),

$$l = k_0 z / \left(1 + \frac{k_0 f z}{.00027 U_0} \right) \quad (3.1.39)$$

where U_0 is the geostrophic wind and f is the Coriolis parameter. The denominator of this expression effectively limits the size of l at large z to a constant. This is reasonable, since we intuitively feel that the mixing length does not increase without bound, particularly in a stable boundary layer.

In addition to $K(z)=\text{constant}$, the follow^{ing} forms are tested:

(a) Unmodified mixing length:

$$K(z) = l^2 \left| \frac{\partial U}{\partial z} \right| \quad \text{for } Ri_B > 0 \quad (3.1.40)$$

(b) Mixing length with stability adjustment (after Estoque (1973)):

$$K(z) = l^2 \left| \frac{\partial U}{\partial z} \right| (1 - \alpha Ri_B)^{-2} \quad (3.1.41)$$

where α is a constant and $Ri_B = g \Delta z \Delta \theta_v / (\bar{\theta}_v \Delta U^2)$ and $\partial U / \partial z = \{ (\partial u / \partial z)^2 + (\partial v / \partial z)^2 \}^{1/2}$.

(c) Mixing length with stability adjustment (after Wu (1965)):

$$K(z) = \ell^2 \left[\left(\frac{\partial u}{\partial z} \right)^2 + \left(\frac{\partial v}{\partial z} \right)^2 - \frac{g}{\theta_v} \frac{\partial \theta_v}{\partial z} \right]^{1/2} \quad (3.1.42)$$

3.1.3.2 The Unstable Case

No adjustment is made on the exchange coefficient in the unstable case. The exchange coefficient in a convective atmosphere becomes so large that it is no longer possible to retain a reasonable time step t that will satisfy the diffusive computational stability criterion $\Delta t \leq \Delta z^2 / 2K$.

Instead we take advantage of the well known observations that under convective conditions the potential temperature θ is very nearly constant with height in an unsaturated atmosphere, while the equivalent potential temperature θ_E or wet-bulb potential temperature θ_w is nearly constant in a saturated atmosphere. This is the motivation for the so-called convective adjustment that is widely used in numerical modeling (Manabe and Strickler (1964), Gierasch and Goody (1970)). Computationally, this is achieved by checking the virtual potential temperature of two adjacent layers. If they are unstable with respect to each other, they are mixed so that entropy, momentum, and total water are conserved. This mixed layer must then be re-checked against the layers above and beneath it and mixing may occur with those layers. After $\partial \theta_v / \partial z$ is nowhere negative, the boundary layer is assumed to be convectively stable.

3.2 RADIATIVE TRANSFER

3.2.1 The "First Approximation"

The equation of transfer appropriate to a plane parallel atmosphere that emits, scatters and absorbs is

$$\mu \frac{d}{dz} I(\tau'(z), \mu, \phi) = I(\tau'(z), \mu, \phi) - (1 - \omega_0(z)) B'_v - \frac{1}{4\pi} \int_0^{2\pi} \int_{-1}^1 p(\mu, \phi, \mu', \phi') I(\tau'(z), \mu', \phi') d\mu' d\phi' \quad (3.2.1)$$

here I is the specific intensity, μ is the cosine of the zenith angle θ , ϕ is the azimuth, $p(\mu, \phi, \mu', \phi')$ is the phase function, and B'_v is the source function corresponding to the local temperature T . The extinction optical depth τ' is

$$\tau'(z) = \int_z^{\infty} (s(z) + k_c(z) + k_g(z)) dz \quad (3.2.2)$$

where $s(z)$ is the volume scattering coefficient for the cloud, and $k_c(z)$ and $k_g(z)$ are volume absorption coefficients for the cloud and gas respectively. The single scattering albedo is

$$\omega_0(z) = \frac{s(z)}{s(z) + k_g(z) + k_c(z)} \quad (3.2.3)$$

In the n^{th} approximation (Chandrasekhar, 1960, p.149) the phase function is expanded in a series of Legendre polynomials

$$p(\mu, \phi, \mu', \phi') = \sum_{l=0}^N \omega_l P_l(\mu, \phi, \mu', \phi') \quad (3.2.4)$$

The intensity I is expanded in a cosine series of the form

$$I(\tau', \mu, \phi) = \sum_{m=0}^N I^{(m)}(\tau', \mu) \cos m(\phi_0 - \phi) \quad (3.2.5)$$

and it can be shown that the phase function is

$$P(\mu, \phi, \mu', \phi') = \sum_{m=0}^N (2 - \delta_{0,m}) \left\{ \sum_{l=m}^N \omega_l \frac{(l-m)!}{(l+m)!} P_l^m(\mu) P_l^m(\mu') \right\} \cos m(\phi' - \phi) \quad (3.2.6)$$

where $\delta_{0,m} = 0$ for $m \neq 0$ and 1 for $m=0$, and where P_l^m are the associated Legendre polynomials. The maximum order N of the polynomials must satisfy $4n-1 > 2N$ in the n^{th} approximation.

The equivalent system of equations corresponding to (3.2.1) for the axially symmetric part of the intensity $I^{(0)}$ is

$$\mu_i \frac{dI_i^{(0)}}{d\tau'} = I_i^{(0)} - (1 - \omega_0) B_{\nu'}' - \frac{1}{2} \sum_{l=m}^N \omega_l \frac{(l-m)!}{(l+m)!} P_l^m(\mu_i) \sum_j a_j I_j P_l^m(\mu_j) \quad (3.2.7)$$

(i=+1, ..., +n)

Since we are interested only in the flux, which is an integrated property of the radiation field, we do not need to solve the system (3.2.7) for a large number of ordinates. In fact, the results of Goody (1964, p.60) and of Sagan and Pollack (1967) indicate that calculations with $n=1$ do not deviate significantly from the exact solution in certain cases where analytic solutions are available. The case $n=1$ is similar to the "two-stream approximation" and represents a field with one stream of radiation in the direction $\mu=1/3^{1/2}$ and another in the direction $\mu = -1/3^{1/2}$. With $n=1$, (3.2.7) yields

$$\mu_i \frac{dI_i^{(0)}}{d\tau'} = I_i^{(0)} - (1 - \omega_0) B_{\nu'}' - \frac{1}{2} \sum_{l=0}^N \omega_l P_l^0(\mu_i) \sum_j a_j I_j^{(0)} P_l^0(\mu_j) \quad (3.2.8)$$

with $P_0^0=1$, $P_1^0=\mu$, $a_j=1$, and $\mu_i = \pm 1/3^{1/2}$ we obtain

$$\frac{1}{\sqrt{3}} \frac{dI^+}{d\tau'} = I^+ - \frac{1}{2} \omega_0 (I^+ + I^-) - \frac{1}{2} \omega_0 \langle \cos \Theta \rangle (I^+ - I^-) - (1 - \omega_0) B_{\nu'}' \quad (3.2.9)$$

$$-\frac{1}{\sqrt{3}} \frac{dI^-}{d\tau'} = I^- - \frac{1}{2} \omega_0 (I^+ + I^-) + \frac{1}{2} \omega_0 \langle \cos \Theta \rangle (I^+ - I^-) - (1 - \omega_0) B_{\nu'}' \quad (3.2.10)$$

where I^+ and I^- denote the components of $I^{(0)}$ in the directions $\mu = 1/3^{1/2}$ and $\mu = -1/3^{1/2}$, respectively. We have also introduced the asymmetry factor $\langle \cos \theta \rangle$ defined by

$$\frac{\bar{\omega}_1}{3} = \bar{\omega}_0 \langle \cos \theta \rangle = \frac{1}{2} \int_{-1}^1 \mu p(\mu) d\mu \quad (3.2.11)$$

which is zero for isotropic scattering and unity for fully forward scattering.

Adding and subtracting (3.2.9) and (3.2.10) we obtain

$$\frac{1}{\sqrt{3}} \frac{d}{dz'} (I^+ - I^-) = (1 - \bar{\omega}_0)(I^+ + I^-) - 2(1 - \bar{\omega}_0) B_v' \quad (3.2.12)$$

$$\frac{1}{\sqrt{3}} \frac{d}{dz'} (I^+ + I^-) = (1 - \bar{\omega}_0 \langle \cos \theta \rangle)(I^+ - I^-) \quad (3.2.13)$$

Recalling that in a non-homogeneous atmosphere $\bar{\omega}_0 = \bar{\omega}_0(\tau')$ we define an absorption optical depth τ by

$$d\tau = (1 - \bar{\omega}_0) dz' = - (k_g(\nu) + k_c(\nu)) dz \quad (3.2.14)$$

eliminating $(I^+ + I^-)$ from (3.2.12) and (3.2.13) we obtain

$$\frac{d^2}{d\tau^2} (I^+ - I^-) = \beta^2 (I^+ - I^-) - 2\sqrt{3} \frac{dB_v'}{d\tau} \quad (3.2.15)$$

where

$$\beta^2 = \frac{3(1 - \bar{\omega}_0 \langle \cos \theta \rangle)}{(1 - \bar{\omega}_0)} \quad (3.2.16)$$

The quantity β is an important parameter that characterizes the radiation field in a cloudy atmosphere: It is a measure of the amount that the absorption path length of a photon is increased due to multiple scatterings. In a clear atmosphere (where $\beta = 3^{1/2}$) it is the traditional "diffusivity factor" (Elsasser, 1942).

3.2.2 Solar Radiation

In the near infrared portion of the solar spectrum (NIR) the source function B'_ν is effectively zero and (3.2.15) yields

$$\frac{d^2}{d\tau^2}(I^+ - I^-) - \beta^2(I^+ - I^-) = 0 \quad (3.2.17)$$

The flux F in the first approximation is

$$F = \frac{2\pi}{\sqrt{3}}(I^+ - I^-) \quad (3.2.18)$$

so that (3.2.17) becomes

$$\frac{d^2 F_s}{d\tau_s^2} = \beta^2 F_s \quad (3.2.19)$$

where the subscript S indicates that we are considering solar radiation.

3.2.2.1 Boundary conditions and solution

At the lower boundary $\tau_s = \tau_s^*$ with a surface reflectivity α the boundary condition is $I^+ = \alpha I^-$ and (3.2.18) together with (3.2.12), (3.2.13) and the change of variable (3.2.14) yield

$$\frac{dF_s}{d\tau_s} + \sqrt{3} \left(\frac{1+\alpha}{1-\alpha} \right) F_s = 0 \quad (\tau_s = \tau_s^*) \quad (3.2.20)$$

The direct solar beam enters the problem as a boundary condition at $\tau_s = 0$:

$$2\pi I^- = \sqrt{3} \mu_0 f(\nu) \quad (3.2.21)$$

and

$$\frac{dF_s}{d\tau_s} - \sqrt{3} F_s = 2\sqrt{3} \mu_0 f(\nu) \quad (\tau_s = 0) \quad (3.2.22)$$

where $f(\nu)$ is the solar irradiation at $\tau_s = 0$. The cosine of the solar zenith angle, μ_0 , is

$$\mu_0 = \sin \lambda \sin \delta + \cos \lambda \cos \delta \cos H \quad (3.2.23)$$

where λ is the latitude, δ is the declination, and H is the hour angle measured from local solar noon.

Equation (3.2.19) is a linear homogeneous second order differential equation, but with a non-constant coefficient since ω_0 and therefore β are functions of the independent variable τ_s . We circumvent this difficulty by replacing the non-homogeneous atmosphere with an atmosphere comprised of N discrete homogeneous layers. In each of the N homogeneous regions the solutions are exponential:

$$F_s(\tau_s^N) = C_{1,N} e^{+\beta^N \tau_s^N} + C_{2,N} e^{-\beta^N \tau_s^N} \quad (3.2.24)$$

The coefficients $C_{1,N}$ and $C_{2,N}$ constitute a set of $2N$ arbitrary constants. Two of the constants are provided by the boundary conditions (3.2.20) and (3.2.22) while the remaining $2N-2$ conditions are provided by requiring the continuity of F_s and $dF_s/d\tau_s$ at the $N-1$ interfaces. The constants are the solution of a system

$$A C = F \quad (3.2.25)$$

where A is a matrix that depends on the absorber concentrations, C is the vector of coefficients $C_{1,N}$ and $C_{2,N}$ and F is a vector whose only non-zero element is $2\mu_0 f_3^{1/2}$. This system can be inverted by standard numerical methods.

The system (3.2.24) is a convenient technique for calculating solar radiation in a cloudy atmosphere, but unfortunately is not of value in an atmosphere in which the gaseous and aerosol extinction coefficients vary with frequency. In particular, we are interested in the net solar flux F_s^{Net}

$$\begin{aligned}
 F_S^{Net} &= \int F_S d\nu \\
 &= \int (C_{1,N}(\nu) e^{+\beta(\nu)^N \tau_S(\nu)^N} + C_{2,N}(\nu) e^{-\beta(\nu)^N \tau_S(\nu)^N}) d\nu \quad (3.2.26)
 \end{aligned}$$

We seek a method which approximates the integral in (3.2.26) as a finite sum of frequency independent terms.

3.2.2.2 Gaseous Absorption

We assume that the only radiatively active gas present in the boundary layer is water vapor. Although there are absorption bands of CO_2 at 1.6, 2.0, 2.7, and 4.3 μ , and of O_2 at 0.69, 0.76, and 1.3 μ , the laboratory results of Burch et al. (1960) indicate that their integrated absorptances are relatively weak, and the analysis of Yamamoto (1962) shows that mean absorptivities which are computed only from the major water vapor bands differ by less than a percent from those computed using H_2O combined with CO_2 and O_2 . Consequently we will consider only the water vapor bands located at 0.72, 0.81, 0.94, 1.1, 1.38, 1.87, 2.7, 3.2, and 6.3 μ .

We ignore all radiative transfer at wavelengths less than 0.7 μ since there are no important H_2O bands in this region and since the contribution to the solar heating from any of the ozone bands is quite negligible in the lower troposphere.

With these simplifications we consider a method of relating the gaseous absorption coefficient k_g to a frequency averaged transmission $\bar{T}_{\Delta\nu}$, where

$$\bar{T}_{\Delta\nu} = \int_{\Delta\nu} \exp(-k_g(\nu) \Delta z) d\nu / \int_{\Delta\nu} d\nu \quad (3.2.27)$$

We transform the integral in (3.2.27) which is a function of ν into one which is a function of k_g :

$$\int_0^{\infty} \exp(-k_g \Delta z) d\nu = \int_0^{\infty} a(k_g) \exp(-k_g \Delta z) dk_g \quad (3.2.28)$$

and approximate the integral by a finite sum to obtain

$$\bar{T}_{\Delta\nu} = \sum_{i=1}^M a_i e^{-k_i \Delta z} \quad (3.2.29)$$

i.e., we approximate the spectrum as a sum of M discrete intervals of fractional extent a_i each having an absorption coefficient k_i . The a_i and k_i are obtained by a non-linear least-square analysis of theoretical or experimental measurements of $\bar{T}_{\Delta\nu}$. The problem is then equivalent to solving the grey problem M times. This method has been used by Cowling (1950), Kondrat'yev (1965, p.99) and more recently by Arking and Grossman (1972) and Lacis and Hansen (1974).

We have chosen to fit the sum of exponentials in (3.2.29) to the results of Yamamoto (1962) using the Levenberg-Marquadt (1944) algorithm. It is difficult to fit absorptivities, which are essentially logarithmic functions, to a sum of exponentials and expect the results to be valid over a wide range of absorber amounts. However, if we consider only the maximum total amount of water vapor found in the summertime Arctic ($\sim 1 \text{ g cm}^{-2}$) and some small amount characteristic of the mass between two grid points in the model ($\sim .01 \text{ g cm}^{-2}$), a very good fit can be obtained for $M=2$. The Yamamoto data and the 4-point fit are shown in Figure 3.4, and the coefficients are given in Table 3.4. The error may become large at short path lengths, but over moderate and long path lengths the fit is good to within one percent. Calculations were also performed with $M=4$ and $M=8$ and there was negligible variation in resultant fluxes.

This is an extremely useful result as it suggests that the water vapor spectrum in the near infrared can be adequately represented with

just two absorption coefficients. In fact, fully 91% of the spectrum can be characterized by the single grey coefficient k_1 . The remaining 8% has a comparatively smaller unit optical depth, and that part of the solar spectrum will be severely attenuated before it reaches the boundary layer.

Table 3.1

Coefficients for 4-Point Fit

a_1	0.91	k_1	$0.011\rho_w$
a_2	0.08	k_2	$2.55\rho_w$

It is important to bear in mind that we can construct a transform of the type (3.2.28) when k_g is a function only of the frequency ν . In a realistic atmosphere k_g will depend upon temperature, and more importantly upon the pressure.

Since we have restricted the problem to a 100mb deep boundary layer, this does not present a serious problem. The discussion of Goody (1964, p.127) indicates that weak lines are not affected by pressure broadening. Strong lines will vary as p/p_0 , but over 100mb this will give rise to a maximum error of only 10%.

However, the variation of line shape from the tropopause to the top of the boundary layer is significant, since there $p/p_0 \sim .1$. Since we have assumed that there are no clouds in the latter region, we can make a traditional pressure scaling correction on the total water vapor above the boundary layer, u_0 ,

$$u'_0 = u_0 \left(\frac{p}{p_0} \right)^n \quad (3.2.30)$$

We set $n=0.5$ to account for the intermediate-strength absorption in this region.

We also adjust u'_0 for the solar elevation with an air mass factor $M = 35/(1224\mu_0^{-2} + 1)^{1/2}$, after Rodgers (1967). The difference between M and μ_0^{-1} is trivial, however, except for extremely low solar elevations.

3.2.2.3 Aerosol Absorption

The cloud scattering coefficient s and cloud absorption coefficient k_c are related to the scattering efficiency factor Q_s and the absorption efficiency factor Q_a according to

$$s(\nu) = Q_s(\nu) N_0 \pi a^2 \quad (3.2.31)$$

$$k_c(\nu) = Q_a(\nu) N_0 \pi a^2 \quad (3.2.32)$$

where N_0 is the volume concentration of scatterer, and a is the particle radius. We compute Q_s , Q_a , and the extinction efficiency $Q_e = Q_s + Q_a$ from an asymptotic form of Mie theory in Appendix B. Although those results indicate that Q_s and Q_a are rather rapidly varying functions of frequency, we shall attempt to treat the cloud as a grey scatterer and absorber by defining Planck mean efficiencies for solar radiation, $\overline{Q_s^S}$ and $\overline{Q_a^S}$, over the frequency interval $\Delta\nu$ by

$$\overline{Q_s^S} = \frac{\int_{\Delta\nu} B_\nu Q_s(\nu) d\nu}{\int_{\Delta\nu} B_\nu d\nu} \quad (3.2.33)$$

$$\overline{Q_a^S} = \frac{\int_{\Delta\nu} B_\nu Q_a(\nu) d\nu}{\int_{\Delta\nu} B_\nu d\nu} \quad (3.2.34)$$

where the efficiencies have been weighted by the Planck function B_ν corresponding to a 6000 K source. These results are shown in Table 3.2 for several values of the particle radius a .

No effort is made to solve for the asymmetry factor $\langle \cos \theta \rangle$ as defined in (3.2.11). The calculations of Irvine and Pollack (1968) show that in the near infrared $\langle \cos \theta \rangle$ varies rapidly neither with wavelength λ

nor with radius for particles in the 3-10 μ range. Their results for a 10 μ particle are used to compute a Planck mean value of $\langle \cos \theta \rangle$ of 0.85.

We are now in a position to consider a mean scattering parameter $\bar{\beta}$, which we may write as

$$\bar{\beta}^2 = 3 \left[\frac{\overline{Q_s^S} (1 - \langle \cos \theta \rangle)}{\overline{Q_a^S} + \frac{k_g}{N_o \pi a^2}} + 1 \right] \quad (3.2.35)$$

where k_g is now one of the grey gaseous absorption coefficients k_1 or k_2 . $\bar{\beta}$ appears as the coefficient of the absorption optical depth in (3.2.24), and determines the effective path length of a photon in a gaseous scattering atmosphere. In Fig.3.5, $\bar{\beta}$ is plotted against the non-dimensional parameter $\gamma = k_g / N_o \pi a^2$. In a sufficiently tenuous cloud $\gamma \rightarrow \infty$ and $\bar{\beta}$ approaches $3^{1/2}$, its value in a clear atmosphere. This limit is also approached in a non-scattering cloud ($\overline{Q_s^S} = 0$), or in one with a completely forward phase function ($\langle \cos \theta \rangle = 1$). If the cloud is imbedded in a very transparent gas, $k_g \rightarrow 0$, and $\bar{\beta}$ approaches its maximum value of $\overline{Q_s^S} (1 - \langle \cos \theta \rangle) / \overline{Q_a^S}$.

For typical values of N_o , a and ρ_w observed in Arctic stratus, $\bar{\beta} \approx 8$ in the transparent region ($k_1 = .01 \rho_w$) and $\bar{\beta} \approx 2$ in the opaque region ($k_2 = 2.6 \rho_w$). This result is particularly interesting since $\bar{\beta}$ appears as a multiplier in the expression for the cloud heating rate

$$Q_{rad}^S = \bar{\beta}^N (k_c + k_g) (c_{1,N} e^{+\beta^N \tau^N} - c_{2,N} e^{-\beta^N \tau^N}) \quad (3.2.36)$$

Consequently, large values of $\bar{\beta}$ will be accompanied by large heating rates within the interior of the cloud.

The notion that there may be substantial near infrared heating rates within a cloud is not a new one. The calculations of Fritz (1958) showed that insufficiently thick clouds as much as 40% of the incident

radiation could be absorbed by the gas and aerosol within the cloud. (Fritz also noted that since the unit optical depth for NIR radiation was larger than that for longwave radiation, convective instability might occur within the cloud. This is an important notion that we will use later.)

In the transparent region $k_1 \sim 3 \times 10^{-8} \text{ cm}^{-1}$, while $Q_a^S \pi a^2 \sim 8 \times 10^{-7} \text{ cm}^{-1}$ which implies that cloud is a more effective absorber than the gas in the near infrared. In the opaque region $k_2 \sim 8 \times 10^{-6} \text{ cm}^{-1}$, and the situation is reversed. The combined effect of the two processes is obtained from the definition of the absorption optical depth, (3.2.14). With (3.2.35) we can write approximately

$$\beta dz \sim (3 \alpha (1 - \langle \cos \theta \rangle) (k_g + k_c))^{1/2} dz \quad (3.2.37)$$

so that in a scattering atmosphere the optical depth varies as the square root of the effective absorption coefficient, whereas the variation is linear in a non-scattering atmosphere.

Table 3.2

Planck Mean Cloud Efficiencies (Solar Spectrum)

	$a = 5\mu$	6.5μ	10μ	15μ	50μ
$\overline{Q_a^S}$.014	.016	.020	.023	.040
$\overline{Q_s^S}$	2.008	2.004	1.974	1.972	1.960

3.2.2.4 Sample calculations

With the notation that F^+ and F^- refer to the upward and downward fluxes of near infrared radiation and that subscripts B and T refer to the base and top of the cloud, respectively, we define cloud reflectivities R_c

and cloud transmissivities T_c in the two-stream approximation as

$$R_c = F_T^+ / F_T^- \quad \text{and} \quad T_c = F_B^- / F_T^- \quad (3.2.38)$$

The behavior of R_c and T_c as a function of the geometrical depth of the cloud is illustrated in Fig.3.6. We consider several values of the product $N_o \chi_a^S = N_o \pi a^2 \overline{Q_a^S}$ to test the sensitivity of the calculation to our assumptions about droplet concentration, drop size distribution and absorption efficiency. For reference, $N_o \chi_a^S = 5 \times 10^{-7}$ corresponds to $\overline{Q_a^S} \sim .01$, $a \sim 6.5$ and $N_o \sim 40$, which are fairly typical of mid-latitude and Arctic stratus (Case II).

As they are defined in (3.2.38), the reflectivity and transmissivity are those of the cloud-gas mixture alone; the surface reflectivity has been set equal to zero, so there is no contribution from radiation that has been multiply reflected between the cloud base and the surface. This particular assumption makes it difficult to compare the results of the first approximation with those of experiments (Neiburger (1949), Griggs (1968), Paltridge (1974), Koptev and Voskresenskii (1962)). In those experiments the cloud albedo depended upon the surface reflectivity since the radiation reflected at the surface had not been removed from F_T^+ or F_B^- .

Transmissivity decreases rapidly with geometrical thickness in the strong region since there $k_g > k_c$ and gaseous absorption dominates. The reflectivity is low for all $N_o \chi_a^S$, and reaches its limiting value in relatively thin clouds. However, this spectral region is not particularly characteristic of real clouds since radiation there is rapidly attenuated before it reaches the cloud top by the superincumbent water vapor.

The conditions in the weak region are more typical of what is actually observed. Reflectivities are about 60% in case II, which is

very typical of cloud albedos measured over dull surfaces such as the ocean. The absorption of a 1 km cloud in case II is about 8%, which is consistent with the measurements of Neiburger and of Fritz, and is also within 2% of the absorptivities estimated for Arctic stratus by Koptev and Voskrezenskii.

Absorptions of 8% will imply fairly intense heating rates within the interior of a cloud. In extreme cases ($N_o \chi_a^S = 5 \times 10^{-5}$) it can reach 100 degrees per day, although 3 degrees per day is more typical of Arctic stratus conditions. The heating profiles for a boundary layer with 3 g kg^{-1} of water vapor are illustrated in Fig.3.7. Large increases in $N_o \chi_a^S$ decrease the heating in the sub-cloud region and slightly increase it in the supra-cloud region, but cause order of magnitude changes within the cloud layer itself.

The heating rate within a cloud that overlays ice should be larger than that in a cloud over the ocean. In Fig.3.8 we have computed the heating within a 500m deep cloud of $N_o \chi_a^S = 5 \times 10^{-7}$ for a non-reflecting surface ($\alpha=0$) and for a highly reflecting surface ($\alpha=.80$). The heating rate is typically twice as large in the highly reflective situation.

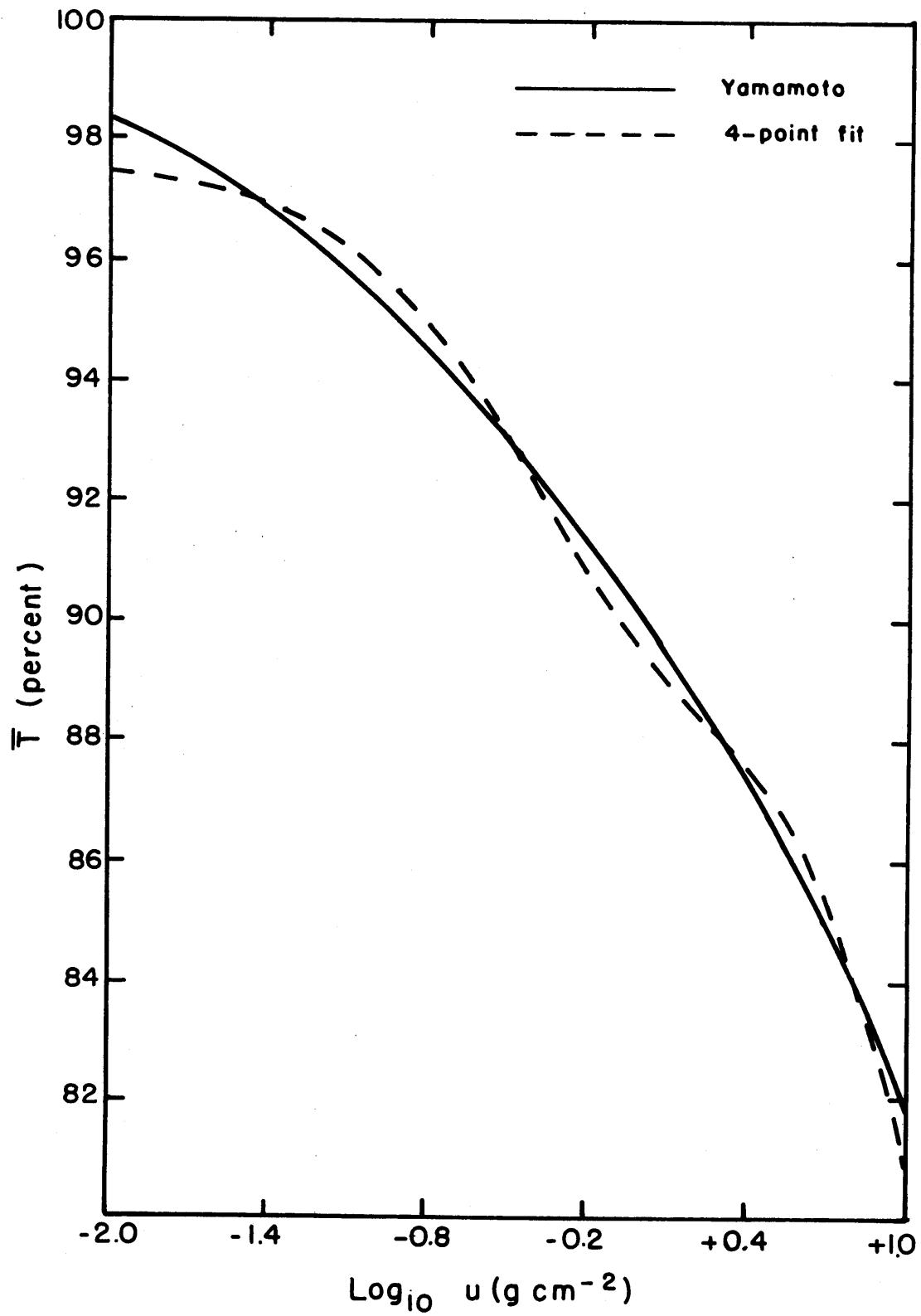


Fig. 3.4 Empirical fit to the absorption data of Yamamoto (1962).

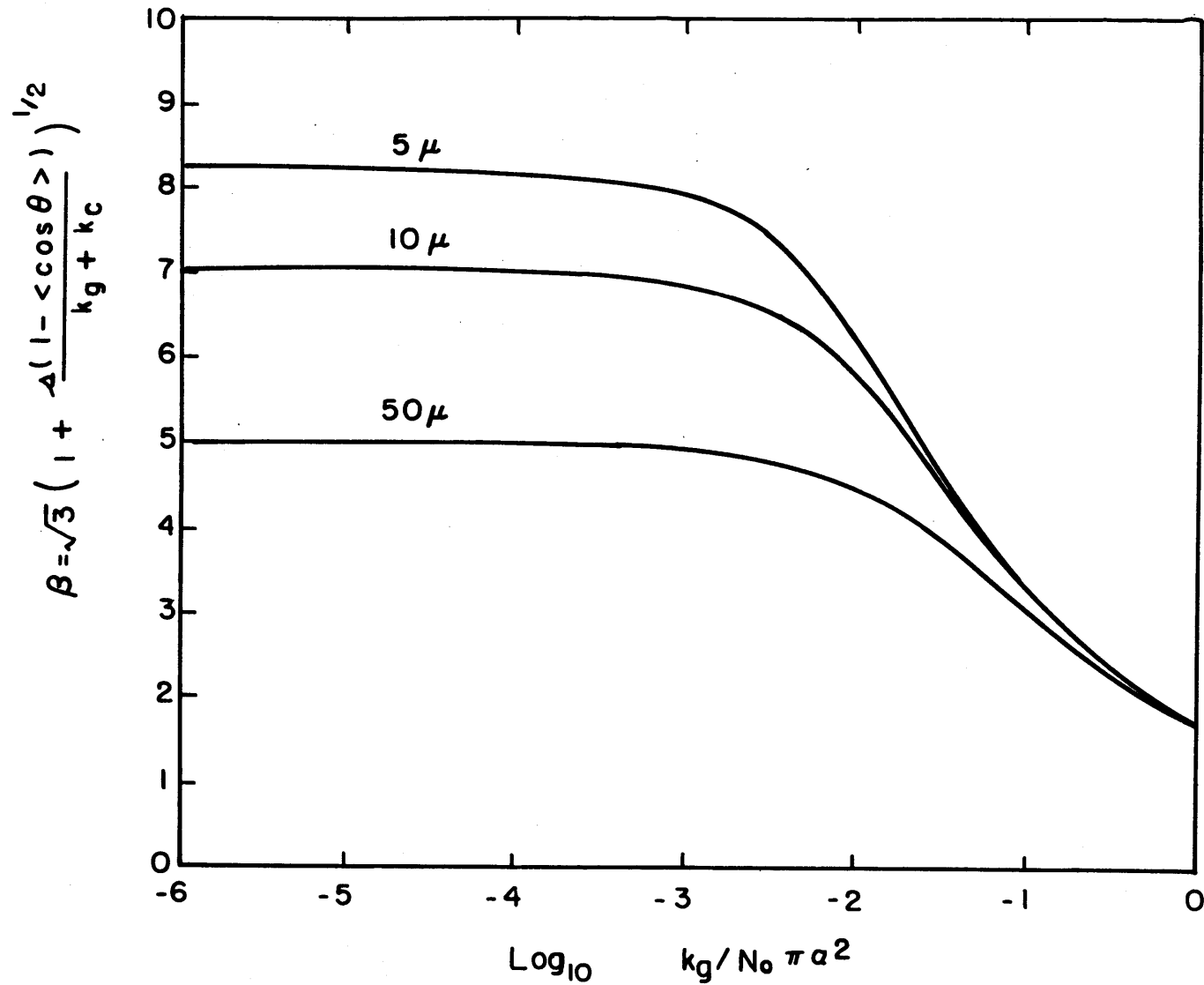


Fig. 3.5 Behavior of the scattering parameter β for selected particle radii as a function of the parameter $k_g / N_0 \pi a^2$. Extinction parameters are Planck mean values computed with (3.2.33) and (3.2.34).

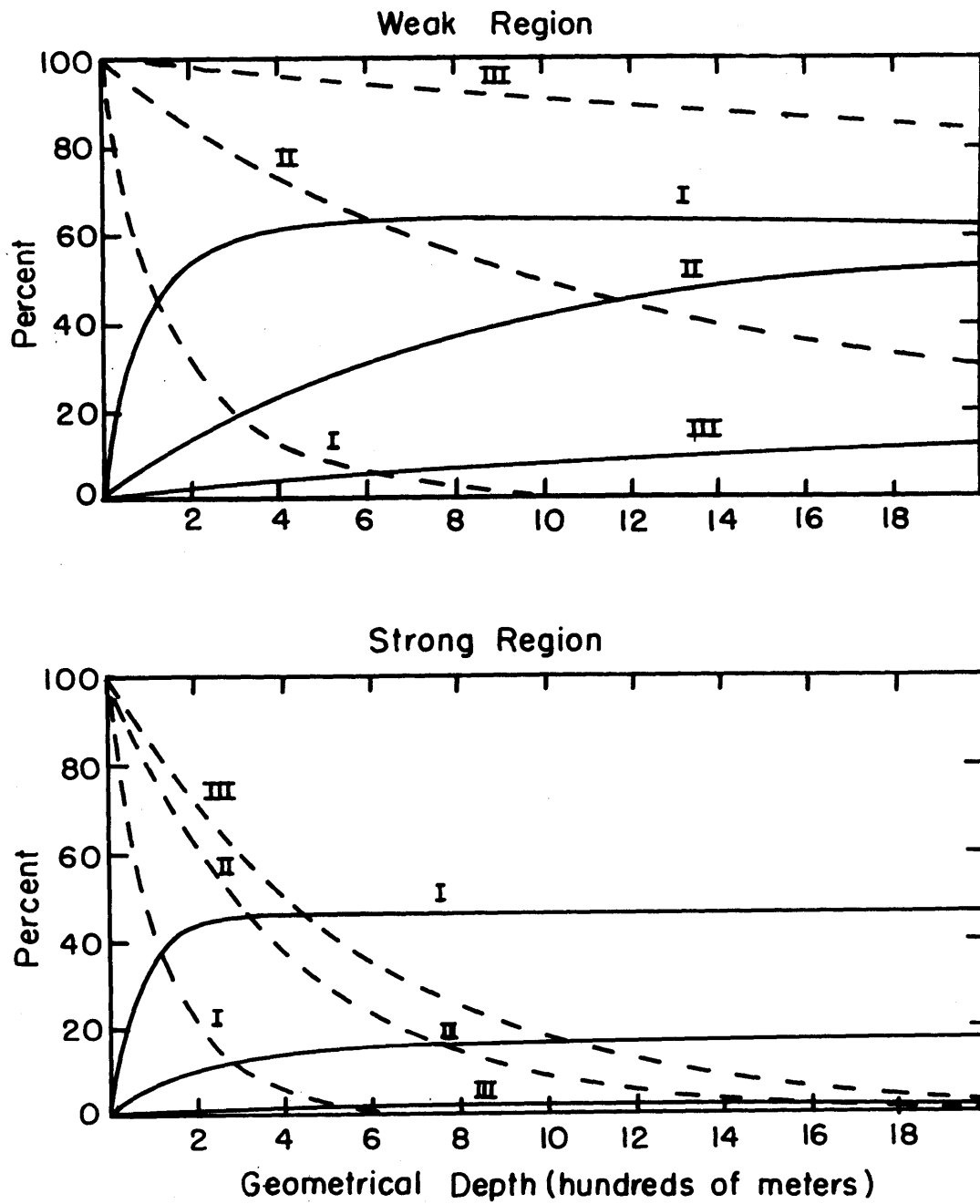


Fig. 3.6 Reflectivities (solid line) and transmissivities (broken line) as a function of cloud geometrical depth. Cases I, II, and III correspond to $N_o \chi_a^s = 5 \times 10^{-6}$, 5×10^{-7} , and 5×10^{-8} , respectively.

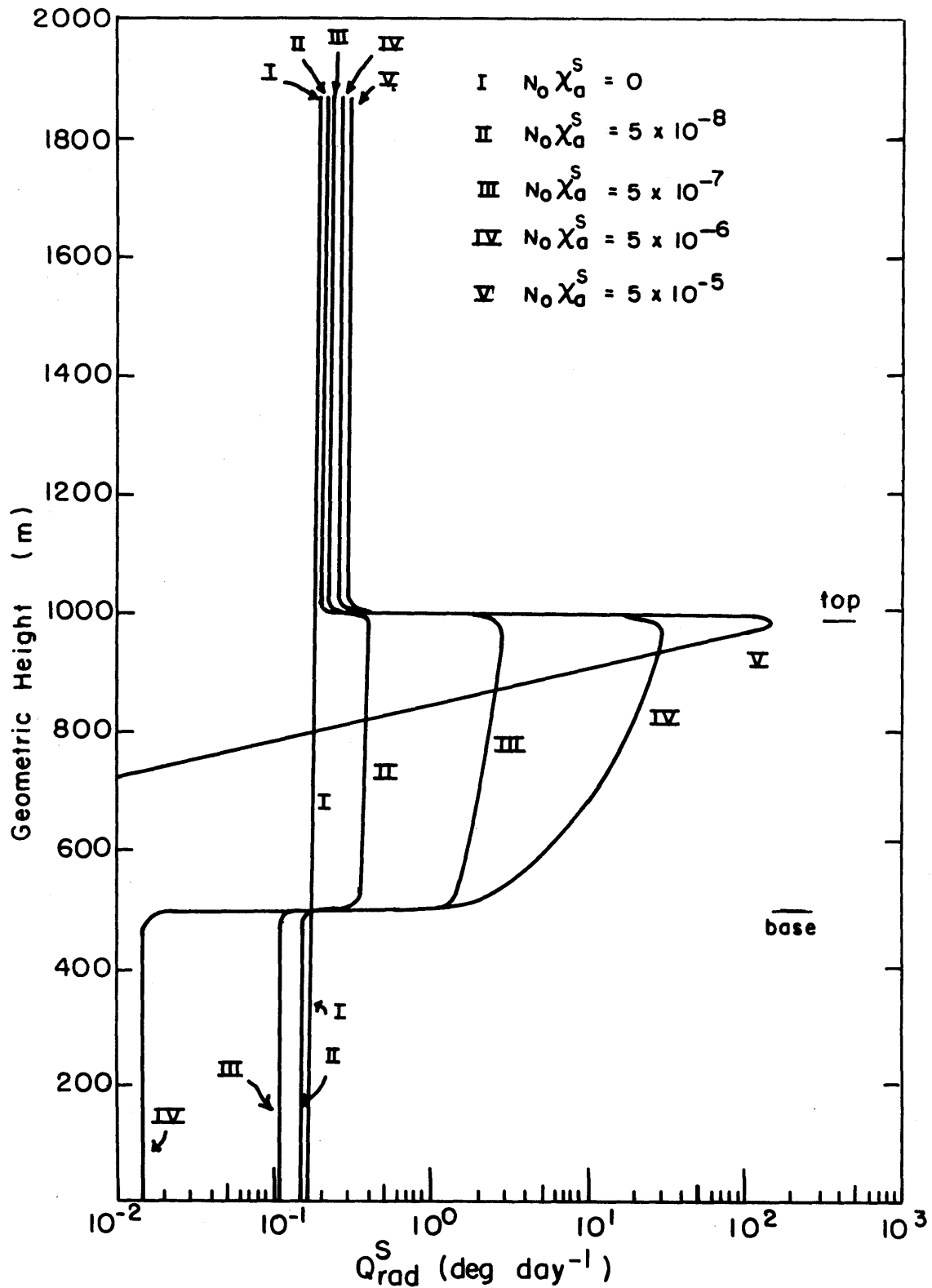


Fig. 3.7 Sample heating rates for a cloud layer between 500 and 1000 m for selected values of the parameter $N_0 \chi_a^S$. In this example the surface reflectivity was 0.40 and the solar zenith angle was 74° . It was assumed that the cloud was embedded in $3 \sigma \text{ kg}^{-1}$ of water vapor.

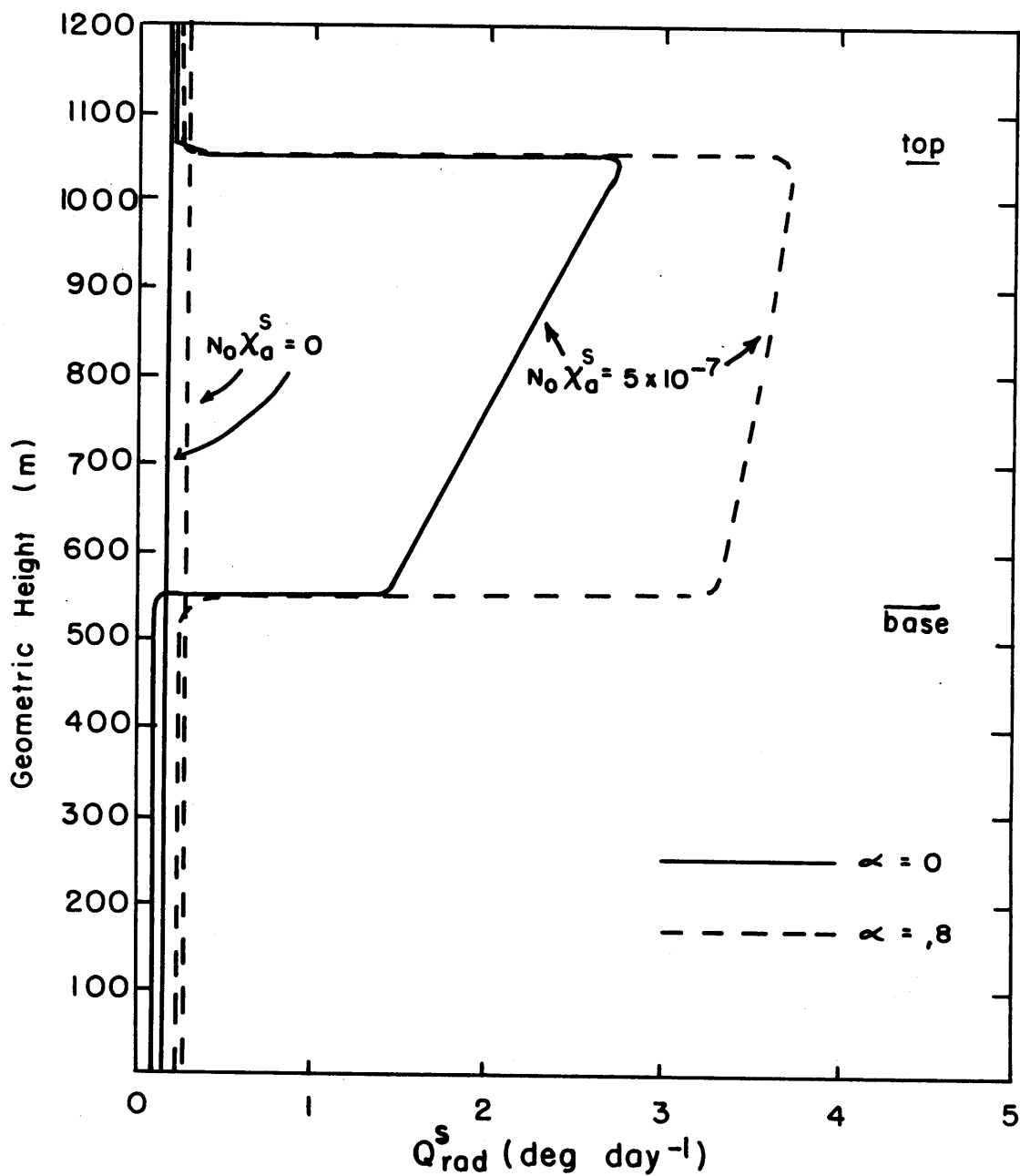


Fig. 3.8 Sample cloud heating rates for extreme values of the surface reflectivity α for $N_0 \chi_a^S$ of 0, and 5×10^{-7} . All other conditions were as in Fig. 3.7.

3.2.3 Thermal Radiation

Retaining the source function in (3.2.15) we have

$$\frac{d^2}{dz_T^2} (I^+ - I^-) = \beta^2 (I^+ - I^-) - 2\sqrt{3} \frac{dB_\nu'}{dz_T} \quad (3.3.1)$$

where the thermal absorption optical depth is defined by

$$dz_T = dz_T(\nu) = -(k_g(\nu) + Q_a(\nu) N_0 \pi a^2) dz \quad (3.3.2)$$

where the subscript T indicates that we are considering thermal radiation.

We first consider the effect of scattering in this region of the spectrum by computing the scattering parameter $\beta^2 = 3(1-\bar{\omega}_0 \langle \cos\theta \rangle) / (1-\bar{\omega}_0)$. We compute Planck mean scattering efficiencies \bar{Q}_s^T and absorption efficiencies \bar{Q}_a^T according to Equations (3.2.33) and (3.2.34) for a 273 K source. These values are given for selected particle radii in Table 3.3.

Table 3.3

Planck Mean Cloud Efficiency (Thermal Spectrum)

	a=5 μ	6.5 μ	10 μ	15 μ	50 μ
\bar{Q}_a^T	.6176	.6902	.7945	.8707	.9797
\bar{Q}_s^T	.8461	1.048	1.219	1.178	1.026

With these values $\bar{\beta}$ is calculated for several particle densities in several regions of the longwave spectrum. These results are shown in Table 3.4. In no case does $\bar{\beta}$ deviate markedly from its non-scattering value of $3^{1/2}$. Only in the water vapor continuum does scattering cause some increase in the absorption path length. Even in that case the increase is only on the order of 10%, and we can therefore ignore scattering in this region of the spectrum.

Table 3.4
Scattering Parameter $\bar{\beta}$

Gas	k_g (cm^{-1})	Mixing Ratio (g/g)	$\bar{\beta}$ (5 μ drops)	
			$N_o=10$	$N_o=100$
H ₂ O (band centers)	$203\rho_w$.003	1.733	1.743
	$203\rho_w$.01	1.732	1.735
H ₂ O (continuum)	$0.21\rho_w$.003	1.879	1.899
	$0.21\rho_w$.01	1.844	1.893
CO ₂	$96\rho_w$.00049	1.745	1.811

The definition of flux (3.2.18) which is used in the first approximation yields the correct black body flux of πB_ν , where B_ν is the Planck function, only if the source function B'_ν is defined with

$$B'_\nu = \frac{\sqrt{3}}{2} B_\nu \quad (3.3.3)$$

With this substitution, and with $\beta \equiv 3^{1/2}$, (3.3.1) yields using the definition of the flux (3.2.18),

$$\frac{d^2 F}{d\tau_T^2} - 3F_T + 2\pi\sqrt{3} \frac{dB_\nu}{d\tau_T} = 0 \quad (3.3.4)$$

where again $3^{1/2}$ is equivalent to the "diffusivity factor". With $I^- = 0$ at $\tau_T = 0$, and $I^+ = B_\nu^*$ at $\tau_T = \tau_T^*$ the boundary conditions are

$$\frac{dF_T}{d\tau_T} - \sqrt{3}F_T = -2\pi\sqrt{3} B_\nu \quad \text{at } \tau_T = 0 \quad (3.3.5)$$

$$\frac{dF_T}{d\tau_T} + \sqrt{3}F_T = 2\pi\sqrt{3} (B_\nu^* - B_\nu) \quad \text{at } \tau_T = \tau_T^* \quad (3.3.6)$$

where B_ν^* is the black body intensity at the lower boundary $\tau_T = \tau_T^*$. Equation (3.3.4) is a linear, second order, non-homogeneous differential equation that is readily solved by the variation of parameters method (Hildebrand, 1962, p.25). We have

$$\begin{aligned}
F_T(\tau) = & \int_{\tau_T}^{\tau_T^*} \pi B_\nu(t) \exp \left[-\sqrt{3}(t - \tau_T) \right] \sqrt{3} dt \\
& + \int_{\tau_T}^{\infty} \pi B^* \exp \left[-\sqrt{3}(t - \tau_T) \right] \sqrt{3} dt \\
& - \int_0^{\tau_T} \pi B_\nu(t) \exp \left[\sqrt{3}(t - \tau_T) \right] \sqrt{3} dt
\end{aligned} \tag{3.3.7}$$

The first term represents the flux emerging from the atmospheric layers below τ_T , the second term is the boundary flux, and the final term is the flux from the layers above τ_T .

3.2.3.1 Absorption in the Non-Grey Atmosphere

It is more convenient to work with the geometrical coordinate z , which is obtained from (3.3.2). We also define absorber amounts u for the gas and m for the cloud according to

$$u(z, z') = \left| \int_z^{z'} \rho_w(z'') dz'' \right| \quad (\text{g cm}^{-2}) \tag{3.3.8}$$

$$m(z, z') = \left| \int_z^{z'} N_o(z'') dz'' \right| \quad (\text{droplets cm}^{-2}) \tag{3.3.9}$$

The flux equation then becomes

$$\begin{aligned}
F_T(z) = & \int_0^z \pi B_\nu(z') d \left\{ \mathcal{I}_c(\sqrt{3} m(z, z')) \mathcal{I}_g(\sqrt{3} u(z, z')) \right\} \\
& + \pi B_\nu^* \mathcal{I}_c(\sqrt{3} m(z, 0)) \mathcal{I}_g(\sqrt{3} u(z, 0)) \\
& + \int_z^\infty \pi B_\nu(z') d \left\{ \mathcal{I}_c(\sqrt{3} m(z, z')) \mathcal{I}_g(\sqrt{3} u(z, z')) \right\}
\end{aligned} \tag{3.3.10}$$

where we have used cloud and gaseous transmissivities defined as

$$\mathcal{I}_c(\sqrt{3} m) = \exp(-\sqrt{3} \pi a^2 Q_a(\nu) m) \tag{3.3.11}$$

$$\mathcal{I}_g(\sqrt{3} u) = \exp(-\sqrt{3} k'_g u) \tag{3.3.12}$$

where k'_g is the mass absorption coefficient for the gas ($\text{cm}^2 \text{g}^{-1}$).

To compute the net thermal flux F_T^{Net}

$$F_T^{Net} = \int F_T d\nu \quad (3.3.13)$$

we consider the cloud emissivity

$$\epsilon_c(\sqrt{3}m) = \int B_\nu (1 - \mathcal{T}_c(\sqrt{3}m)) d\nu / \int B_\nu d\nu \quad (3.3.14)$$

and the gaseous emissivity

$$\epsilon_g(\sqrt{3}u) = \int B_\nu (1 - \mathcal{T}_g(\sqrt{3}u)) d\nu / \int B_\nu d\nu \quad (3.3.15)$$

and obtain

$$\begin{aligned} F_T^{Net} = & - \int_0^z \pi B(z') d\epsilon_M(\sqrt{3}m(z, z'); \sqrt{3}u(z, z')) \\ & + \pi B^*(1 - \epsilon_M(\sqrt{3}m(z, 0); \sqrt{3}u(z, 0))) \\ & - \int_z^\infty \pi B(z') d\epsilon_M(\sqrt{3}m(z, z'); \sqrt{3}u(z, z')) \end{aligned} \quad (3.3.16)$$

where $\pi B = \sigma T^4$, and the mixed emissivity ϵ_M is defined with

$$1 - \epsilon_M(m; u) = \left\{ 1 - \epsilon_g(u) \right\} \times \left\{ 1 - \epsilon_c(m) \right\} \quad (3.3.17)$$

Equation (3.3.10) implied that we could write a cloud-gas transmissivity \mathcal{T}_M as the product of the transmissivity of the components $\mathcal{T}_c \times \mathcal{T}_g$, and this was strictly true since we were considering monochromatic radiation. Equation (3.3.16) assumes that the mean transmissivity of the mixture $\overline{\mathcal{T}}_M$ can also be expressed as a product $\overline{\mathcal{T}}_c \times \overline{\mathcal{T}}_g$, a condition that is satisfied only if the spectra of liquid water and the gaseous constituents are uncorrelated over some wide range of frequency, or if the cloud absorption is extremely weak.

We further simplify the problem by assuming that the cloud is a

grey absorber in this region of the spectrum, and replace the absorption efficiency $Q_a(\nu)$ in (3.3.11) with its Planck mean value $\overline{Q_a^T}$, computed in Appendix B.

3.2.3.2 Gaseous absorption.

In practice only two optically active bases, CO_2 and H_2O , are considered in the infrared. There is some radiation emitted in the $9.6\mu \text{O}_3$ band, but its contribution to the heating rate in the boundary layer is about 0.1 deg day^{-1} and is negligible (Doplick, 1972; Rodgers, 1967).

The emissivities of water vapor are taken from the calculations of Rodgers (1967a). We use

$$\epsilon(\sqrt{3} u_{\text{H}_2\text{O}}) = \sum_1^N a_n u_{\text{H}_2\text{O}}^{n/2} \quad u_{\text{H}_2\text{O}} < 10^{-3} \text{ g cm}^{-2} \quad (3.3.18)$$

$$\epsilon(\sqrt{3} u_{\text{H}_2\text{O}}) = \sum_0^N b_n (\ln u_{\text{H}_2\text{O}})^n \quad u_{\text{H}_2\text{O}} > 10^{-3} \text{ g cm}^{-2} \quad (3.3.19)$$

Although the coefficients a_n and b_n are temperature dependent, we assume Rodgers' 250 K values in this calculation. Similarly for carbon dioxide,

$$\epsilon(\sqrt{3} u_{\text{CO}_2}) = \sum_1^N c_n u_{\text{CO}_2}^{n/2} \quad u_{\text{CO}_2} < .01 \rho_{\text{CO}_2} \text{ g cm}^{-2} \quad (3.3.20)$$

$$\epsilon(\sqrt{3} u_{\text{CO}_2}) = \sum_0^N d_n (\ln u_{\text{CO}_2})^n \quad u_{\text{CO}_2} > .01 \rho_{\text{CO}_2} \text{ g cm}^{-2} \quad (3.3.21)$$

We assume a carbon dioxide concentration of $.49\text{g/kg}$. The total water vapor in the region between z_T and $z=\infty$ is u_0 , and we use several climatological mean values to test the models' sensitivity to this parameter.

In Figures 3.9 and 3.10 we have plotted the variation of the mixed emissivity ϵ_M with particle concentration and water vapor path length. The influence of the droplets is illustrated in Fig.3.9. For very thick clouds ($m \sim 10^7$) the mixed emissivity approaches unity and

the cloud acts as a black body as is usually assumed. Similarly as $m \rightarrow 0$, ϵ_M is the standard water vapor emissivity curve. The intermediate region corresponds to "non-black" clouds. The depth of a typical Arctic stratus is $\sim 300\text{m}$ and $N_0 \sim 30\text{cm}^{-3}$ so $m \sim 9 \times 10^5$. This implies that Arctic stratus clouds have emissivities that deviate somewhat from unity, a result already anticipated by Marshunova (1961), who suggests emissivities as low as .85.

Even in tenuous clouds the emissivity is kept high by small amounts of water vapor, as shown in Fig.3.10. In fact, it is the water vapor within the cloud that places a lower bound on the mixed emissivity.

Detailed calculations of a non-grey water cloud immersed in a non-grey water vapor gas were carried out by Yamamoto et al. (1970, 1971) and included the effects of scattering as well as absorption and emission. Their results confirm our belief that scattering plays a negligible role: The reflectivity of their thickest clouds was only $\sim 2\%$ in the $5\text{-}50\mu$ region. The emissivity of their clouds also approached unity at $m \sim 10^7$, which is consistent with the results of our simple model.

3.2.3.3 An Approximate Expression for the Cloudless Atmosphere

The integrals in (3.3.10) can only be evaluated numerically in a realistic atmosphere, and we seek a convenient approximation to them for later discussions involving thermal radiation.

Differentiating (3.3.16) with respect to z , and with $m=0$ we obtain

$$\frac{\partial F_{\text{Net}}}{\partial z} = - \int_0^z \pi B(z') d \left(\frac{\partial}{\partial z} \epsilon(u(z, z')) \right) - \pi B^* \frac{\partial}{\partial z} \epsilon(u(0, z)) - \int_z^\infty \pi B(z') d \left(\frac{\partial}{\partial z} \epsilon(u(z, z')) \right) \quad (3.3.22)$$

with $\rho_w(z) = \partial u / \partial z$, and $\epsilon' = d\epsilon(u)/du$ (3.3.22) can also be written

$$\frac{\partial F_{Net}}{\partial z} = -\rho_w \int_0^z \pi B(z') d\epsilon'(u(z, z')) - \pi \rho_w B^* \epsilon'(u(0, z)) - \rho_w \int_z^\infty \pi B(z') d\epsilon'(u(z, z')) \quad (3.3.23)$$

The significance of the terms in this equation are illustrated with a Brooks (1950) radiation diagram. The abscissa is linear in the fourth power of T, and the ordinate is the derivative of the emissivity $\epsilon'(u)$. The area under the curve in Fig.3.11 is the graphic solution to (3.3.23). The profile shown here is a typical July Arctic sounding obtained from Rodgers (1967a), and the level $u=0$ corresponds to 850mb (~ 2 km). A 5 K temperature discontinuity is also assumed at the surface.

The largest contributions come from direct loss to space (Region I) and exchange with relatively opaque layers above and below (Region III). The boundary term (Region II) is large in this case, but its area varies in direct proportion to $(B^* - B(0))$. The contribution from transparent regions is everywhere negligible. (The sign of the contribution from the area to the left of the dotted line is, of course, opposite in sign to that from the right.)

Regions I and II are rectangles with areas $B(z)\epsilon'(u(z, \infty))$ and $(B(0) - B(z))\epsilon'(u(z, 0))$, respectively, while Region III is approximately a triangle.

Considering only exchange with space and exchange with the boundary, we have

$$\rho_c \frac{\partial T}{\partial t} = -\rho_w(z) \pi B(z) \epsilon'(u(z, \infty)) + \rho_w(z) \pi (B_0 - B(z)) \epsilon'(u(z, 0)) \quad (3.3.24)$$

and with $\partial T / \partial t = (4\sigma T^3)^{-1} \partial B / \partial t$, (3.3.24) expresses the cooling rate as a simple first order linear differential equation.

3.2.3.4 Sample Calculations

We consider typical longwave heating rate profiles for a boundary layer with a 500 m deep cloud for several values of the parameter $N_o \chi_a^T$. For illustrative purposes we assume that the temperature is adiabatic with $T(0) = T^* = 273$ K, and that the mixing ratio is uniform in the boundary layer at 3g/kg. These profiles are shown in Fig.3.12.

Cooling occurs in a clear atmosphere ($N_o \chi_a^T = 0$) and is about one degree per day. A tenuous cloud ($N_o \chi_a^T = 5 \times 10^{-6}$) has more cooling throughout the depth of the cloud, and less cooling in the sub-cloud region. A very opaque cloud ($N_o \chi_a^T = 5 \times 10^{-4}$) has intensive cooling at the cloud top and intensive heating at the cloud base. The former is about -130 K day^{-1} and the latter about $+50$ K day^{-1} . These large rates are confined to relatively thin layers at the top and base, and fall to zero in the cloud interior. A less opaque cloud ($N_o \chi_a^T = 5 \times 10^{-5}$) has substantial cooling (~ 10 K day^{-1}) throughout the depth of the cloud, but is still warmed at the base. The conditions of this last case appear to be most typical of summertime Arctic stratus.

Large cooling rates at the top of stratiform clouds have in fact been observed in experimental studies. Although few details of the measurements are given, Markosova and Shlyakhov (1972) quote cooling rates of 1.0 ± 0.5 degrees K per hour at the top of Sc and St type clouds.

The large heating rates at and beneath the cloud base are a consequence of our assumptions about the temperature distribution in the sub-cloud region. In an atmosphere with a negative lapse rate the cloud base will be heated by the warmer region below even if there is no temperature discontinuity. Only if the atmosphere and lower boundary are isothermal will there be no heating at the base.

These results and those of Section 3.2.2.3 have important implications for the dynamics of Arctic stratus. A cloud with $N_o \chi_a^T$ of 5×10^{-5} will undergo substantial cooling over a layer of depth $(3^{1/2} N_o \chi_a^T)^{-1}$ or about 100m. Solar radiation will be absorbed over a depth $\sim (\beta N_o \chi_a^S)^{-1}$ or about 700m. Thus, since the uppermost layers of the cloud are cooling rapidly while the interior is being heated, the cloud should be convectively unstable in the absence of other processes. Rapid overturning should occur even if the atmosphere were otherwise stable.

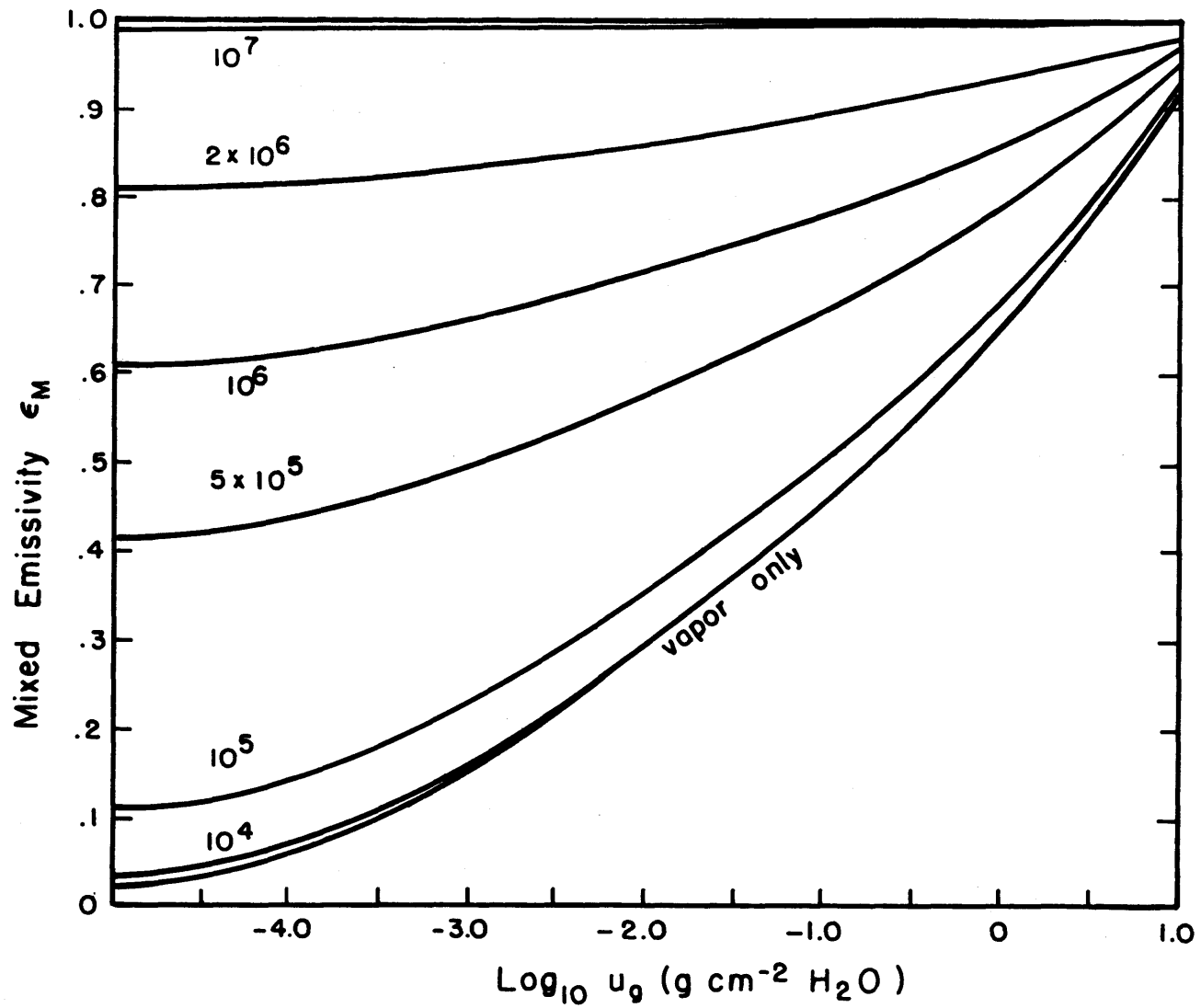


Fig. 3.9 Mixed emissivity ϵ_M as a function of water vapor path length u_g for selected values of the particle path length m .

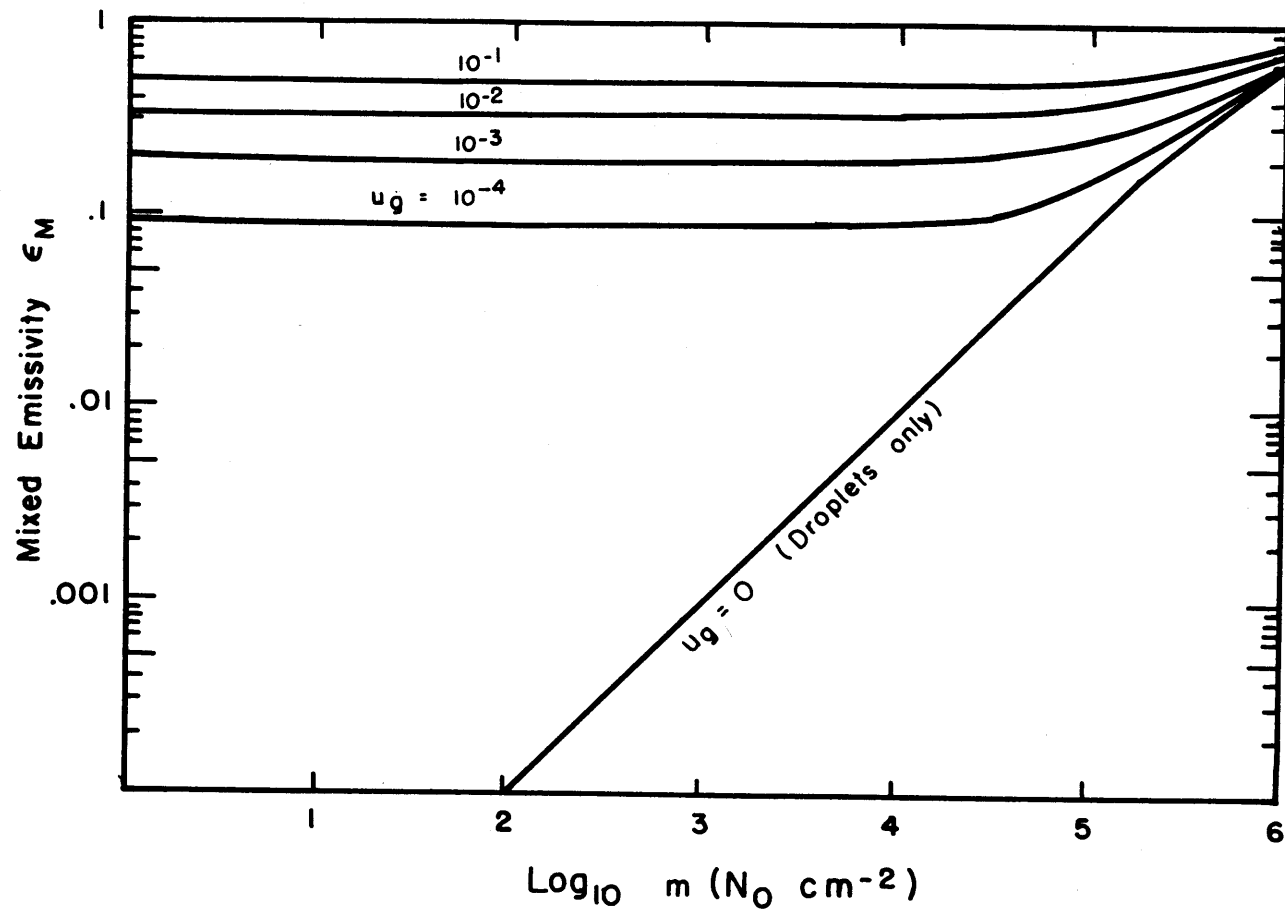


Fig. 3.10 Mixed emissivity ϵ_M as a function of m for selected water vapor path lengths.

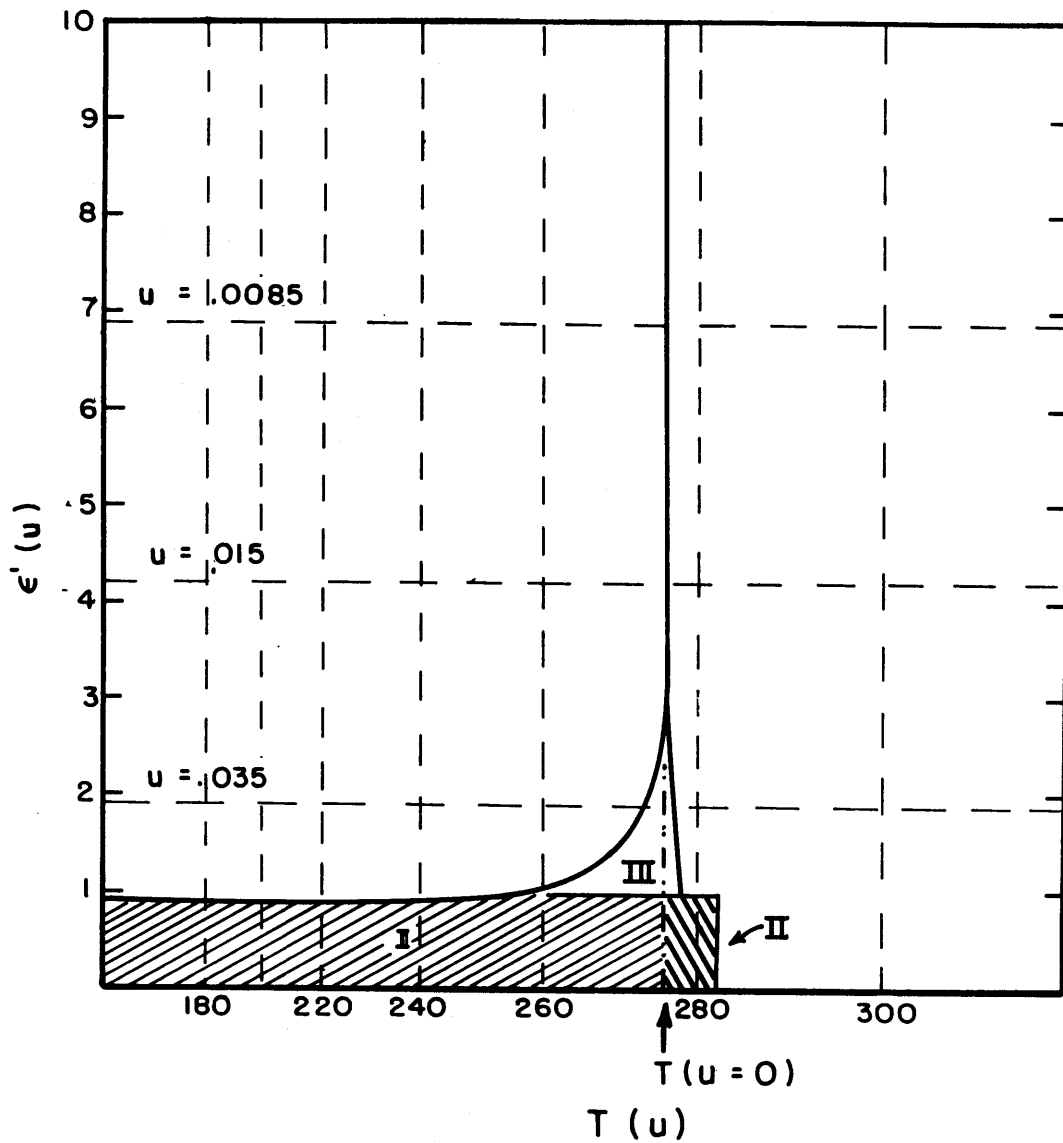


Fig. 3.11 Graphic representation of the heating rate equation (3.3.23). Region I represents cooling to space, Region II represents exchange with the lower boundary, and Region III represents exchange with the regions above and below $u=0$.

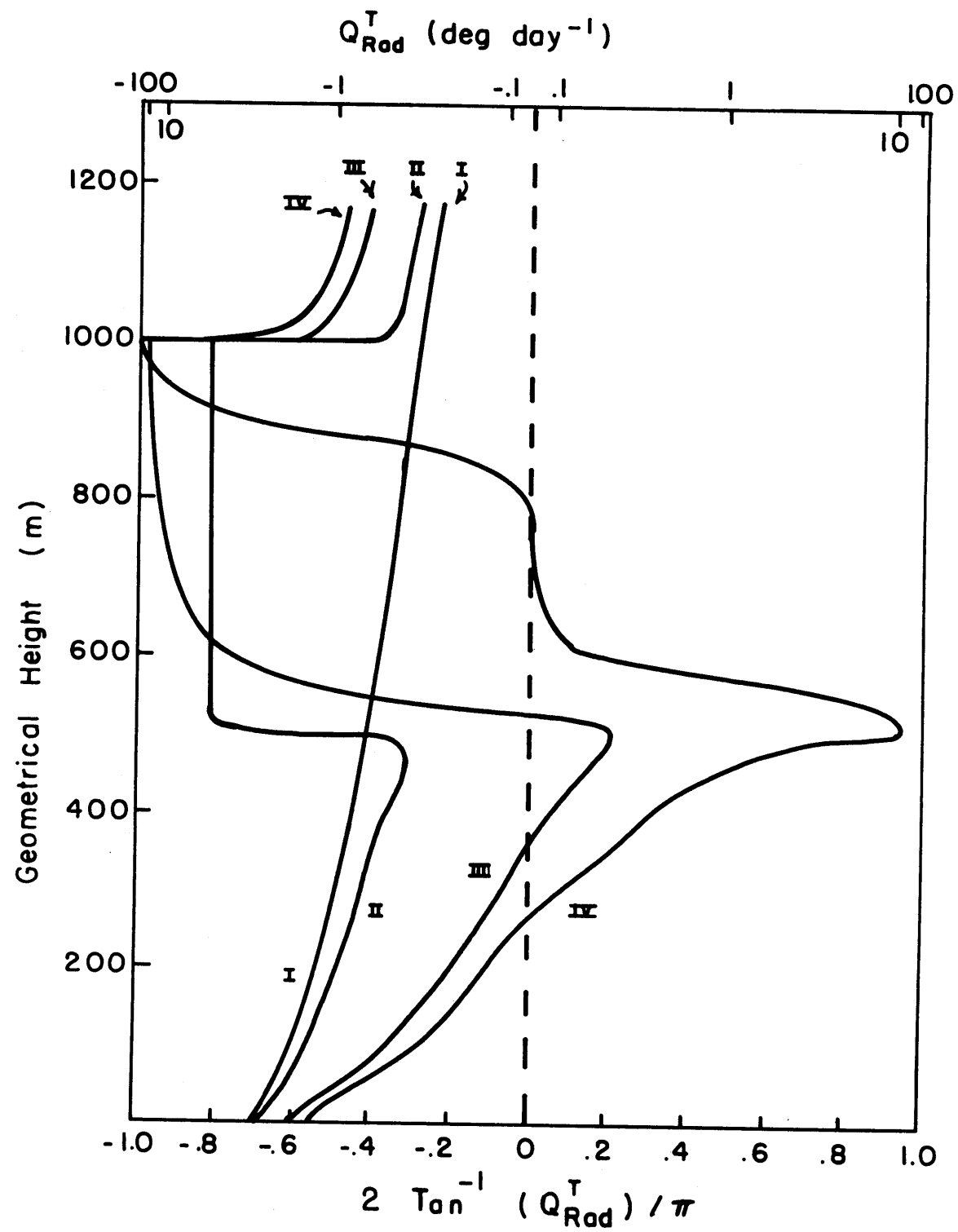


Fig. 3.12 Long wave heating rate profiles in a 500 m thick cloud over-
 laying a 273 K surface. Cases I through IV represent $N_{0, \lambda}^T =$
 $0, 5 \times 10^{-6}, 5 \times 10^{-5},$ and 5×10^{-4} , respectively. Abscissa
 is the arctangent of the heating rate to illustrate the wide
 range of positive and negative values.

4. RESULTS AND DISCUSSION

4.1 MECHANISM AND STRUCTURE

4.1.1 The Basic States

To provide standards against which the model's response to systematic variations of its parameters could be tested, the results for "typical" non-convective and convective atmospheres were arbitrarily defined as basic states (Cases I and II). We define a non-convective state as that which occurs when the air is initially warmer than the ice surface, and a convective state as that which occurs when the air is initially colder than the ice surface. The initial conditions, boundary conditions, and parameterizations of turbulence and radiation were chosen to correspond as nearly as possible to what were assumed to be the actual conditions of the summertime Arctic. The conditions in the basic states were as follows:

Boundary conditions. The temperature at the lower boundary ($z=0$) remained constant in time at the equilibrium temperature of melting fresh-water ice, 273 K. The surface was saturated with respect to liquid water at this temperature. The surface reflectivity α was 0.40, which is typical of a melting ice surface with crusted snow and meltwater ponds. A mean surface roughness z_0 of 0.1 cm was assumed. At the top of the boundary layer ($z=z_T$) we assumed $\partial\theta_E/\partial z=0$, $\partial r/\partial z=0$, $u=0$, and $v=0$. At the lower boundary we assumed $\theta_E=\theta_E(0)$, $r=r_s(0)$, $u+U_0=0$, and $v=0$.

We append a heating term due to subsidence to (2.2.6) of the form $w\partial\theta_E/\partial z$, where w is a mean vertical velocity. Admittedly this procedure is not strictly valid since (2.2.6)-(2.2.9) do not allow for a divergent wind field. However, the error is quite small. In the Arctic $\partial w/\partial z \sim 10^{-7} \text{ sec}^{-1}$.

Over a horizontal scale of 3000km this would imply that the velocity changes by only 30 cm sec^{-1} . We therefore retain the subsidence term to test its effect on cloud development, a procedure that was also followed by Lilly (1968) under less valid conditions.

The mean subsidence during the summer at 80°N according to the calculations of Newell et al. (1972, p.57) at 700mb ($\sim 3 \text{ km}$) is $+0.32 \times 10^{-4} \text{ mb sec}^{-1}$, or about $-0.04 \text{ cm sec}^{-1}$. The mean vertical velocity w was assumed to decrease linearly to zero at $z=0$ from its value at 3 km, i.e., $w = Az$ where $A = -1.4 \times 10^{-7} \text{ sec}^{-1}$.

Initial conditions. For the non-convective case we assumed $\theta(0) = 277 \text{ K}$ and $\partial\theta_E/\partial z = +1 \text{ deg km}^{-1}$ which corresponds to a stable column of air that is initially 4°C warmer than the surface. For the convective case we assumed $\theta(0) = 270 \text{ K}$ and $\partial\theta_E/\partial z = +5 \text{ deg km}^{-1}$ corresponding to a stable column of air that is initially 3°C colder than the surface. The initial relative humidity was 90% throughout the depth of the boundary layer, and the initial wind profile was a balanced Ekman spiral corresponding to a constant eddy diffusivity of $2.5 \times 10^4 \text{ cm}^2 \text{ sec}^{-1}$.

Radiative conditions. The diurnal cycle of solar radiation was not included in the basic state and a mean solar zenith angle of 74° was used. For the purpose of computing extinction parameters all drops were assumed to be 6.5μ in radius. We use $\overline{Q_a^T} = 0.690$, $\overline{Q_s^S} = 2.004$, and $\overline{Q_a^S} = 0.016$. The superincumbent water vapor u_o remained fixed at 0.5 g cm^{-2} .

Ekman layer turbulence. In all calculations, except in those specifically designed to test the sensitivity of the model to the parameterization of turbulence above the surface layer, we computed the eddy diffusivity $K(z)$ from the unmodified mixing-length formulation (3.1.40).

The fall velocity w_f for a 6.5μ drop computed according to Stokes' Law is 0.5 cm sec^{-1} .

Case I. The results of a seven-day integration of the non-convective case are shown in Figure 4.1, where the liquid water content of the boundary layer is shown as a function of height and time.

Condensation initially occurred after 34 hours at 500 m. The base of the cloud remained at a constant level throughout most of the integration, while the top rose slowly and attained a quasi-stationary height in about five days. The most striking feature of the cloud was that after 66 hours the uniformly cloudy region divided into two well-defined cloud layers separated by a very distinct interstice. The bases and tops of both layers approached stationarity in about five days.

The upper layer was the more dense, with a maximum liquid water content of 0.34 g kg^{-1} at the top (about $.37 \text{ g m}^{-3}$). The lower layer was more tenuous, and had a maximum content of 0.04 g kg^{-1} (about $.05 \text{ g m}^{-3}$). The liquid water content decreased uniformly from top to base in the upper layer, but in the lower layer maximum liquid water was found in the center of the cloud and diminished toward both the base and the top.

At equilibrium the base and top of the lower layer (hereafter referred to as h_1 and h_2 , respectively) were located at 500 m and 1050 m, and the base and top of the upper layer (hereafter referred to as h_3 and h_4 , respectively) were located at 1450 m and 1700 m. The interstice was 400 m deep.

Case II. The case of initially colder air flowing over relatively warmer ice is illustrated in Figure 4.2. In the convective case condensation occurred much earlier, after only 8 hours. The main body of the cloud again separated, although after 50 hours. A stationary distribution of

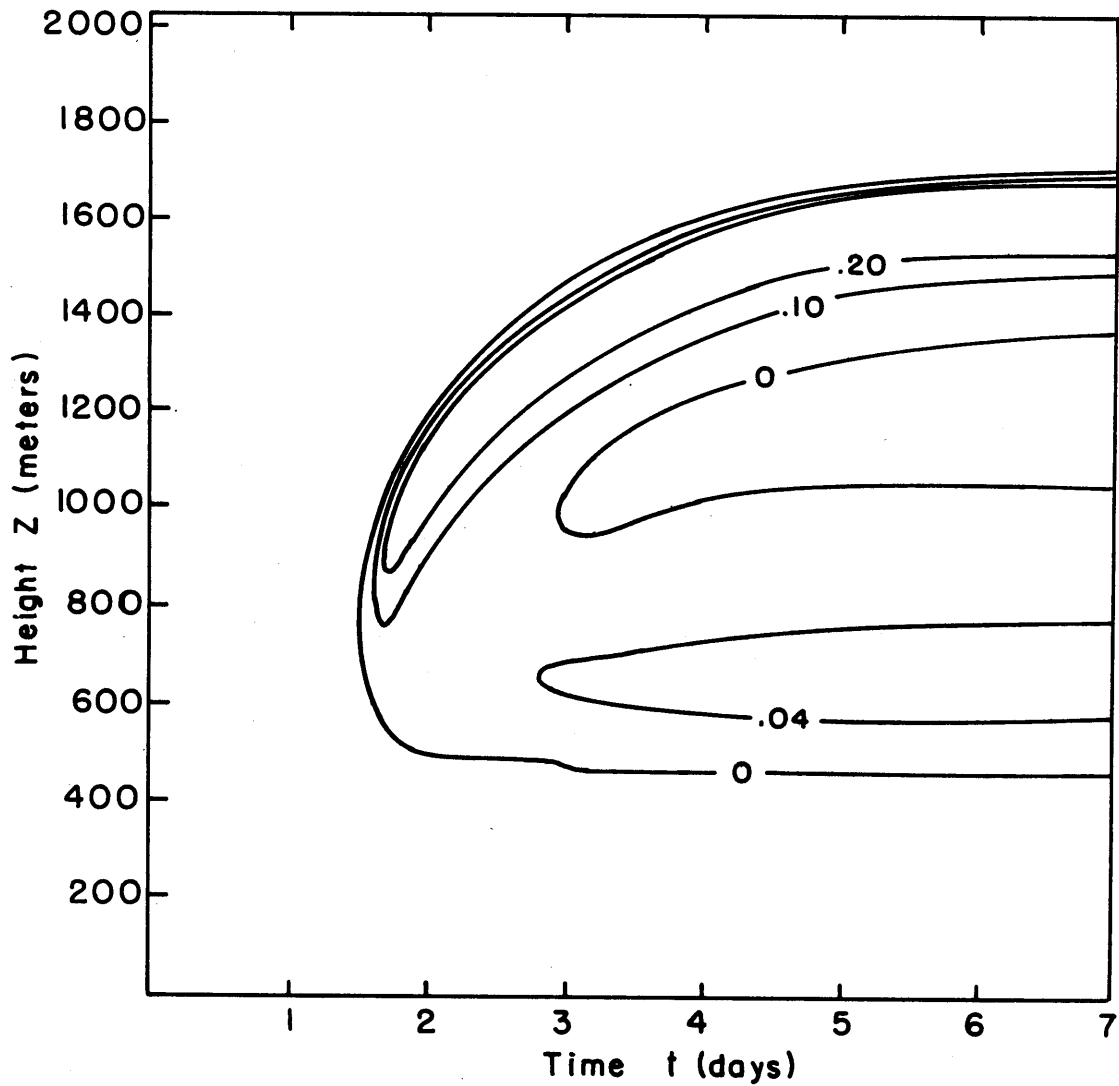


Fig. 4.1 Liquid water distribution as function of height and time for Case I, air initially 4°C warmer than surface, and initial relative humidity of 90%. Isolines are g kg^{-1} .

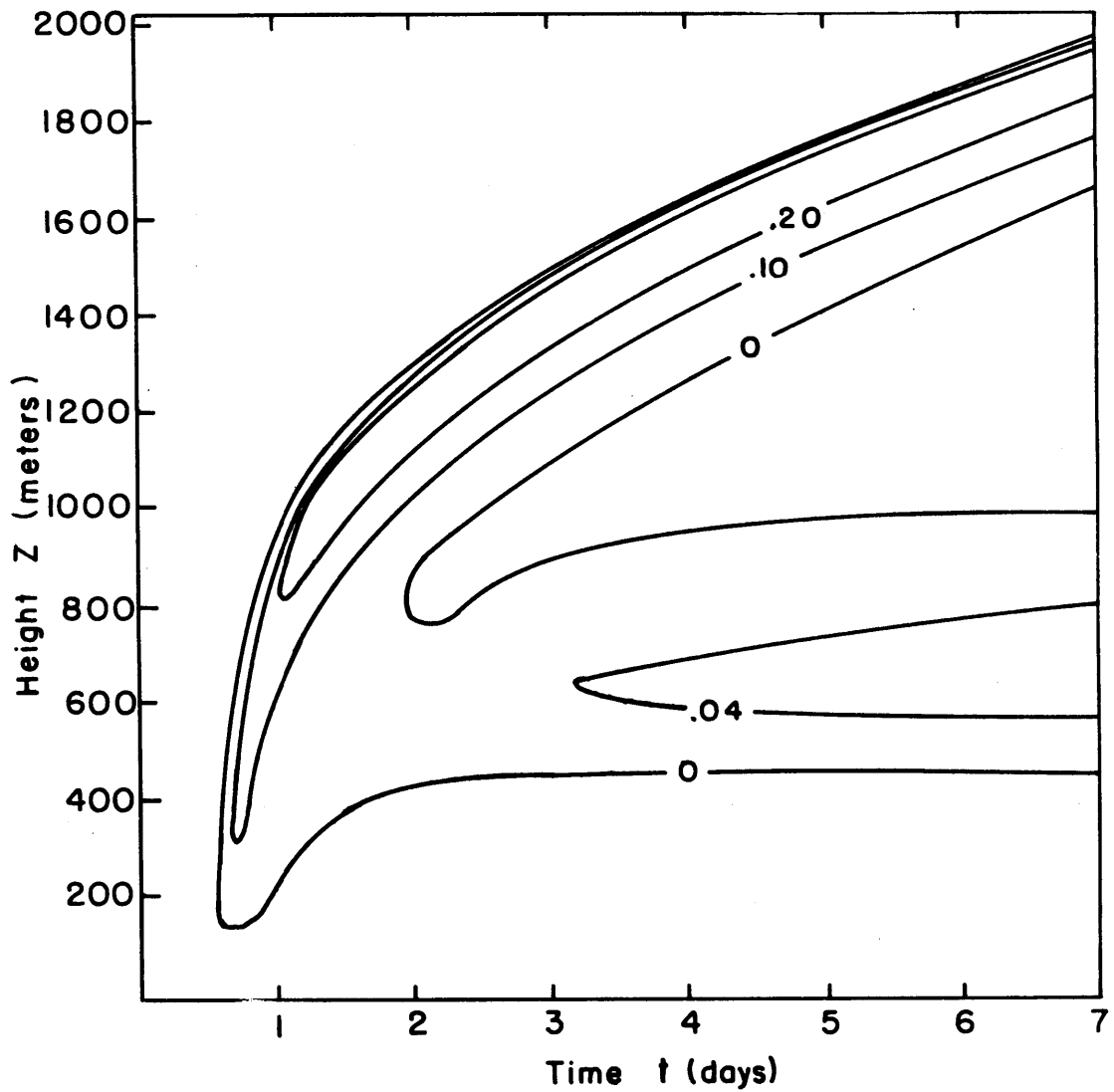


Fig. 4.2 Liquid water distribution as function of height and time for Case II, air initially 3°C colder than surface and initial relative humidity of 90%. Isolines are g kg^{-1} .

liquid water was reached in the lower cloud layer, but unlike Case I the upper cloud layer continued to lift slowly even after five or six days. The difference is probably associated with a process that we will refer to as the radiative lifting of a cloud top, and will be discussed in more detail in Sect.4.1.6. Except this, many aspects of a cloud that was formed from warm air streaming over cold ice were similar to one that was formed from colder air flowing over relatively warmer ice. Although observations indicate that it is the former process that most frequently occurs in the summertime Arctic, we included a consideration of the latter process to illustrate that the quasi-equilibrium cloud conditions are to some extent independent of the initial difference between the surface temperature and the temperature of the pack ice.

4.1.2 Initiation of Condensation

We inquire into the mechanisms which bring a previously unsaturated stratum of air to saturation. We assume that there are an adequate number of condensation nuclei present, and that a liquid water condensate forms when the computed total water content $r(z)$ exceeds the saturation mixing ratio at the ambient temperature $r_s(T(z), p(z))$. This process of supersaturation can be brought about by cooling a stratum of moist air to its dew point by radiation or turbulence, or by introducing more water vapor into it than it can accommodate by evaporation at the surface or by turbulent mixing.

Combining the Clausius-Clapeyron equation, the definition of mass mixing ratio, and the hydrostatic equation we have,

$$dr_s = \left(\frac{p}{p_0}\right)^{\kappa} \left(\frac{0.622}{p} \left(\frac{L_v e_s}{R_v T^2}\right)\right) d\theta + \left(\frac{0.622 p g e_s}{p^2} - \frac{0.622 L_v e_s g}{p R_v T^2 C_p}\right) dz \quad (4.1.1)$$

where L_v is the latent heat of vaporization of water, R_v is the gas constant for water, $\kappa = R/C_p$, and e_s is the saturation vapor pressure at the

temperature T . At a fixed level z we may write approximately

$$\left(\frac{\partial r_s}{\partial t}\right)_z = a \left(\frac{\partial \theta}{\partial t}\right)_z \quad (4.1.2)$$

where $a = 0.622 L_v e_s (p/p_0)^K / (p R_v T^2)$, and may be treated as a constant in the neighborhood of 263 K. The equivalent potential temperature is approximately

$$\theta_E \approx \theta + \frac{L r_s}{C_p} \quad (4.1.3)$$

which combined with (4.1.2) yields

$$\frac{\partial r_s}{\partial t} = b \frac{\partial \theta_E}{\partial t} \quad (4.1.4)$$

where $b = (L/C_p + 1/a)^{-1}$. To change the saturation mixing ratio by some amount Δr_s we change the equivalent potential temperature by $\Delta \theta_E$. We may write approximately

$$\frac{\Delta \theta_E}{\tau_c} \approx -\frac{\partial}{\partial z} (\overline{w' \theta_E'}) + \frac{\theta_E}{\rho C_p T} Q_{rad}^S + \frac{\theta_E}{\rho C_p T} Q_{rad}^T - w \frac{\partial \theta_E}{\partial z} \quad (4.1.5)$$

where τ_c is a condensative time scale, and is the time over which the change $\Delta \theta_E$ occurs.

We consider the characteristic time scales associated with each of the four terms on the left hand side of (4.1.5) as follows:

In the eddy-diffusive approximation

$$-\frac{\partial}{\partial z} (\overline{w' \theta_E'}) = K \frac{\partial^2 \theta_E}{\partial z^2} \sim \left(\frac{K}{D^2}\right) \Delta \theta_E \quad (4.1.6)$$

where D is the length scale of the mixing process. This defines a time scale for mixing $\tau = D^2/K$. For $K = 5 \times 10^4 \text{ cm}^2 \text{ sec}^{-1}$ and $D = 500 \text{ m}$, $\tau = 14 \text{ hours}$.

$$\begin{aligned} & \left(\frac{K}{H^2}\right) \sim \left(\frac{K}{H^2}\right) \sim \left(\frac{K}{H^2}\right) \\ & \frac{1}{\tau} \sim \frac{1}{H^2} + \frac{1}{2\tau} \\ & \text{good when } H^2 \gg 2\tau^2 \end{aligned}$$

In a moist convective layer of depth D we may assume that the equivalent potential temperature is constant with height and therefore that the flux of θ_E is linear with respect to height. We may write for the convective case,

$$\frac{\partial}{\partial z}(\overline{w'\theta'_E}) \approx \frac{(\overline{w'\theta'_E})_0}{D} \quad (4.1.7)$$

and computing the surface flux $(\overline{w'\theta'_E})_0$ with bulk transfer coefficients we have

$$\frac{1}{\Delta\theta_E} \frac{\partial}{\partial z}(\overline{w'\theta'_E}) = C_u C_\theta u_a / D \quad (4.1.8)$$

where u_a is the anemometer level wind. This defines a time scale for convective mixing of $D/(C_u C_\theta u_a)$, or 9.2 hours for $C_u C_\theta = 3 \times 10^{-3}$ and $u_a = 5 \text{ m sec}^{-1}$.

For the subsidence term,

$$w \frac{\partial \theta_E}{\partial z} \sim A \Delta\theta_E \quad (4.1.9)$$

since we had assumed $w=Az$. This defines a time scale for subsidence of $|A|^{-1}$ or 1984 hours in a summertime Arctic atmosphere. In the California coastal stratus problem (Lilly, 1968), $A = -5.5 \times 10^{-6} \text{ sec}^{-1}$ or $\tau = 50$ hours. This is an important distinction between Arctic stratus and California stratus: Dynamical lifting or subsidence associated with large-scale horizontal divergence is unimportant in the former case, but acts on the same time scale as radiation and turbulence in the latter.

The amount of solar radiation absorbed in a cloudless layer of depth D over a non-reflecting surface is $\mu_0 f(1-\exp(-k_1 u^*(D)))$ so that we may write approximately

$$Q_{\text{rad}}^S \sim \rho_0 \mu_0 f \frac{(1 - \exp(-k_1 u^*(D)))}{D} \quad (4.1.10)$$

and define a characteristic time scale τ for solar radiation

$$\tau^{-1} = \frac{Q_{\text{rad}}^S}{\rho C_p \Delta\theta_E} \quad (4.1.11)$$

which yields $\tau = 230$ hours for $\Delta\theta_E = 1^\circ\text{C}$, $D = 500\text{m}$, $\mu_0 = 74^\circ$, and $u^*(D) = 0.2 \text{ g cm}^{-2}$.

The same value for a mean solar zenith angle of 45° is 88 hours.

With the approximation (3.3.24) the longwave radiative term Q_{rad}^T is expressed in terms of boundary exchange and cooling to space. The latter is

$$Q_{\text{rad}}^T(\text{space}) = \pi p_w B(z) \epsilon'(u_\infty^*) \quad (4.1.12)$$

and with $\epsilon'(u_\infty^*) = .1 \text{ cm}^2 \text{ g}^{-1}$ and $r_v = .003$, the time scale for cooling to space is

$$\tau^{-1} = \frac{Q_{\text{rad}}^T(\text{space})}{\rho C_p \Delta\theta_E} \quad (4.1.13)$$

and yields a characteristic time of 8.9 hours for $\Delta\theta_E = 1^\circ\text{C}$.

The boundary term represents an increase of equivalent potential temperature if the surface is warmer than the atmosphere and a decrease if it is colder. At 500 m we have $u_u^* = 0.2 \text{ g cm}^{-2}$, and $\epsilon' = .3 \text{ cm}^2 \text{ g}^{-1}$ and

$$\tau^{-1} = \frac{4\sigma \bar{T}^3 (T_0 - T) \epsilon'(u_u^*) r_v}{\Delta\theta_E C_p} \quad (4.1.14)$$

This yields a time τ of 230 hours for a 3°C temperature difference. However, ϵ' increases rapidly as u_u^* decreases, and closer to the boundary, say at 10 m, $\epsilon' \sim 17 \text{ cm}^2 \text{ g}^{-1}$ and $\tau = 4$ hours.

These results suggest that in a stratum of air in a stable atmosphere the temperature and therefore the saturation mixing ratio change most

rapidly due to cooling to space and diffusion, since the time scales for these processes are the fastest. Once a condensate has formed, it can persist because the heating due to solar radiation and subsidence is effective over time scales that are an order of magnitude longer.

In an unstable situation the convective time scale is the fastest, although cooling to space is still somewhat important. We have chosen an example with a moderately weak surface temperature flux which is typical of the summertime Arctic. Under more intensely convective conditions such as in the tropics, $(\overline{w'\theta'_E})$ may be 5-10 times as large as in the present example, and θ_E and r would change almost exclusively due to convection.

We are now able to explain the initiation times for Cases I and II. Beginning with a relative humidity of 90%, r_v or r_s must change by about $.4 \text{ g kg}^{-1}$ at 273 K. With $a=.2 \text{ g kg}^{-1} \text{ deg}^{-1}$, cooling to space should bring about condensation in about 20 hours, and convective mixing in about 9 hours. These were approximately the results obtained with the model.

4.1.3 Development

To first assure ourselves that the overall structure of the results were independent of the parameterization of the eddy diffusivity factor K , calculations were done for several types of K dependencies. Case I was computed with a mixing length formulation (3.1.40) that was not modified for stability, but that did force K to become small at the top of the Ekman layer. In Case III (Fig.4.3) K was calculated with a stability correction suggested by Estoque (Eq.3.1.41) while in Case IV K was held constant throughout the calculation at $10^3 \text{ cm}^2 \text{ sec}^{-1}$. The results differed from Case I in detail but not in general form.

In Case III condensate first formed at the surface as an advective fog, but the base rapidly lifted to an equilibrium height of 200 m. The

original cloud layer again showed the characteristic separation after 3 days, and the top cloud layer climbed to a quasi-stationary height of about 1400 meters. The depth of the interstice was comparable to that in Case I. The reason a cloud could form at the surface was that initially the strong positive temperature gradient associated with the four degree temperature discontinuity at the surface generated K 's only on the order of $5-10 \times 10^2$ in the lowest layers, and longwave radiative exchange with the surface dominated turbulent mixing. As the air became less stable (3.1.41) allowed K to become larger and the base of the cloud was effectively lifted.

A calculation was also done with the stability factor of Wu (Eq.3.1.42), and did not differ markedly from Case III.

Case IV was computed with a constant eddy diffusivity, but still resembled Cases I and III in many respects. As in Case III the condensate formed at the surface due to the relatively small value of K that had been chosen, and the base did not lift any higher than 75 m since there was no mechanism for K to increase as neutrality was approached. The most unrealistic aspect of a constant K formulation, of course, is that K should diminish toward the top of the Ekman region, particularly in the stable case. Consequently the upper cloud layer did not reach a quasi-stationary level but lifted to the upper boundary of the model, a feature that also was exhibited by the cloud in some convective cases.

Cases III and IV illustrate an important feature that is well known to forecasters of fog and stratus; namely, that the wind speed at anemometer level is an important factor in deciding whether a condensate will occur as a ground fog or be lifted into a stratus cloud. If the turbulent transport is fast enough, water vapor will be transported down the humidity gradient to the surface and supersaturation will not occur in the

lowest layers. But if this transport cannot keep up with the rate of radiative cooling, a condensate will form in the surface layer. This effect is illustrated by Case V (Fig.4.4), which was identical to Case I except that U_0 was only 2 m sec^{-1} rather than 10 m sec^{-1} . In this case the lower layer rested on the surface as an advective fog for the duration of the integration, although separation and lifting of a second layer did occur even in this case.

We may note parenthetically at this point that Sverdrup did report fog almost every day during July and August from the Maud's location near the edge of the pack ice. It is difficult to say whether this corresponds to the Case III situation of an advective fog lifted to stratus cloud level. Sverdrup used the terms "fog" and "low stratus" synonymously, and it is therefore not possible to infer details about the evolutionary process from his data.

Finally, we consider a hypothetical atmosphere (Case VI) in which there were no turbulent or dynamical fluxes whatsoever. The eddy diffusivity K was everywhere set equal to zero, and no convective adjustments were made on superadiabatic gradients. Moreover u_* , r_{v*} , and $u_*\theta_*$ were set to zero to eliminate fluxes of heat and moisture from the surface, and subsidence was likewise ignored. The results for this purely radiative model are shown in Fig.4.5. The basic structure of the multilayered cloud is preserved even in the absence of turbulent fluxes.

The clear interstice is indicative of a region in which the ambient temperature exceeds the dew point temperature corresponding to the local specific humidity. This characteristic cold-hot-cold structure of the boundary layer is partially due to the differing optical properties of the cloud in the NIR and longwave portions of the spectrum, and partially

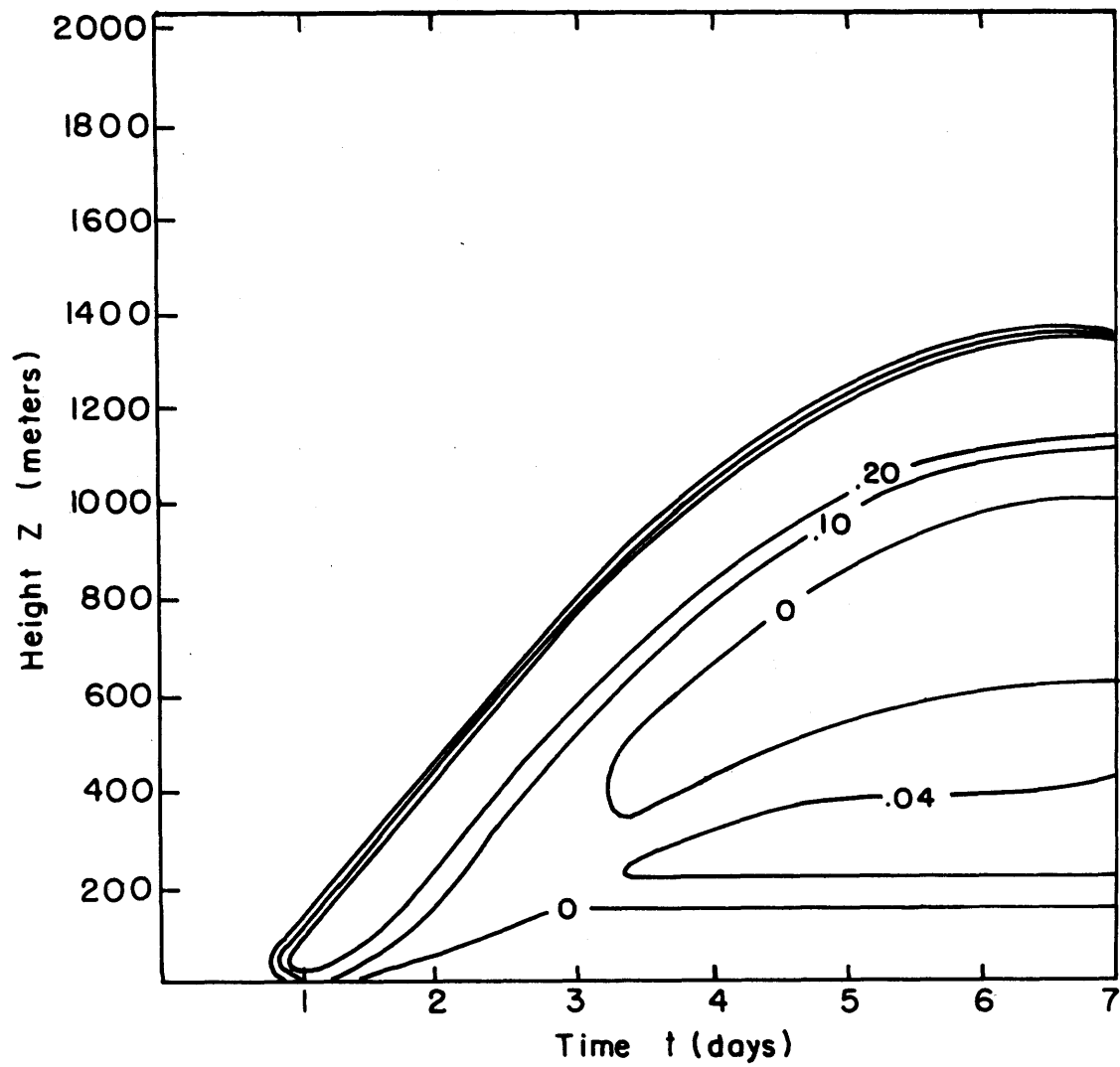


Fig. 4.3 Liquid water distribution for calculation performed with the stability adjusted eddy diffusivity of Estoque (Case III). Isolines are g kg^{-1} .

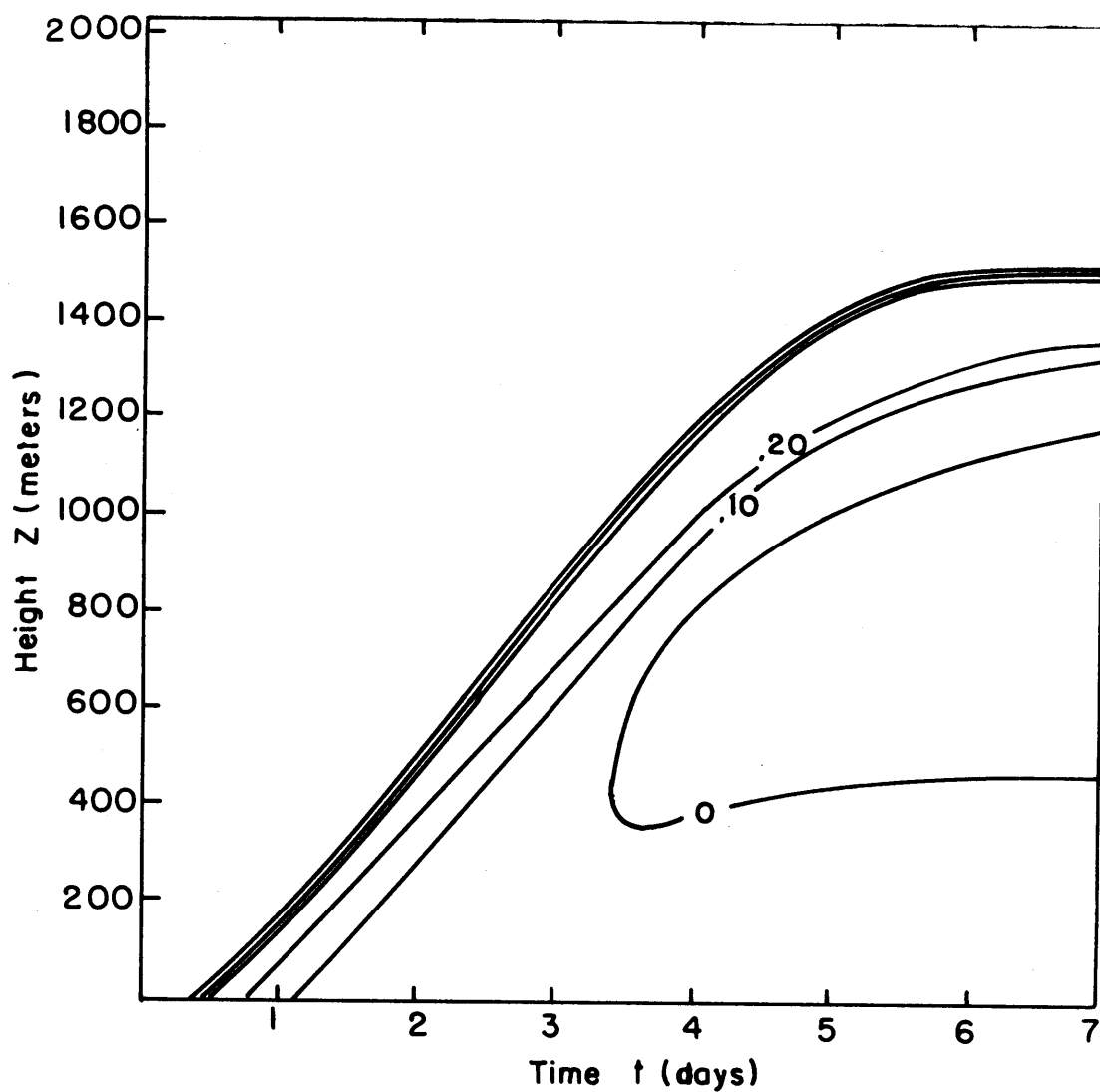


Fig. 4.4 Liquid water distribution computed for Case V, warmer air flowing over colder surface, but basic current of only 2 m sec^{-1} . Lower layer rests on surface as an advective fog. Isolines are g kg^{-1} .

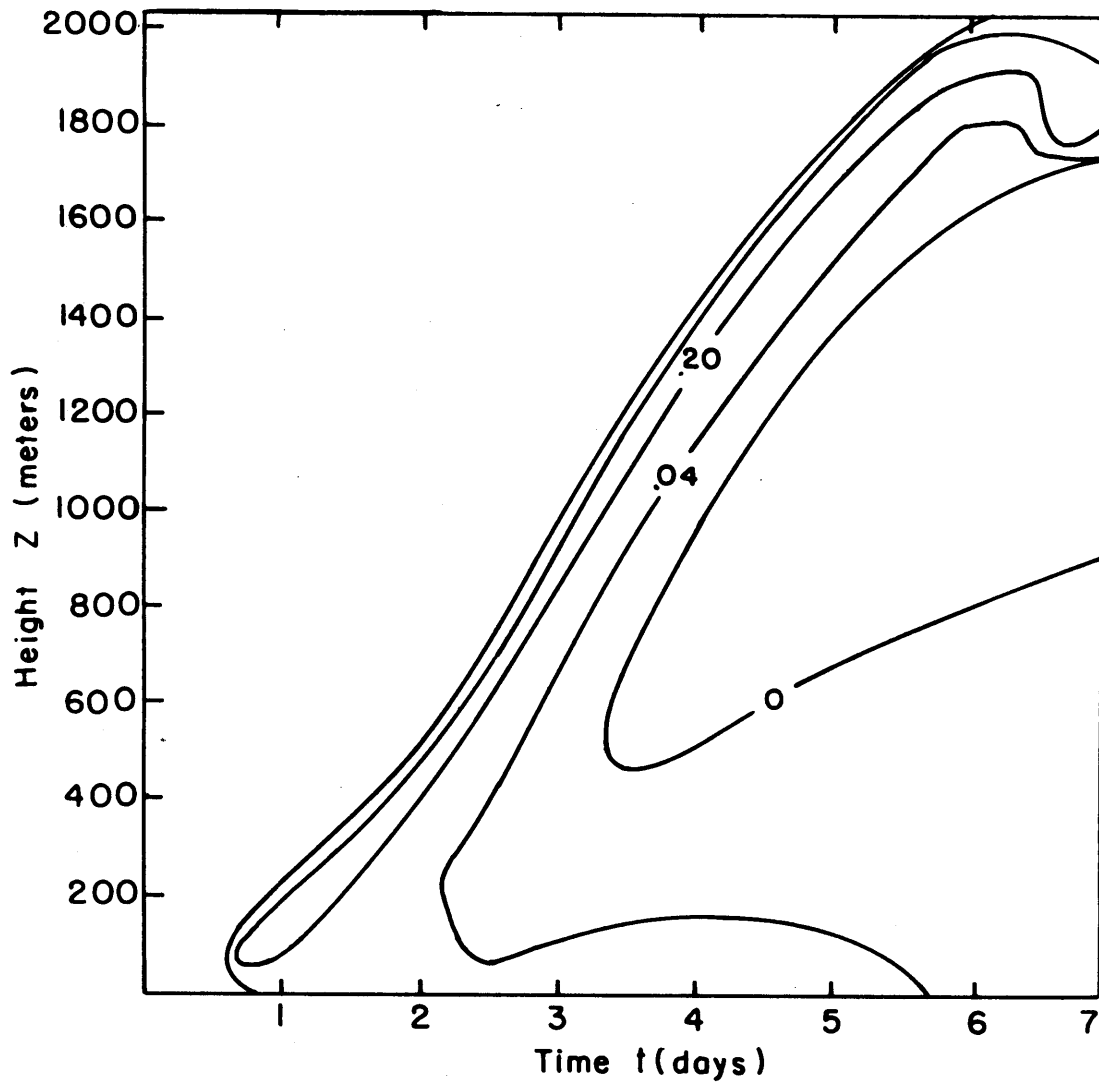


Fig. 4.5 Liquid water distribution for a hypothetical atmosphere with no turbulent or dynamical fluxes. Eddy diffusivity K was zero, as were u_* , r_{v*} , and $u_*\theta_*$.

due to the fact that we have constrained the surface temperature to remain at 0°C, as demonstrated by the following argument:

Consider a homogeneous cloud layer of finite optical depths τ_S^* and τ_T^* resting on a surface of constant temperature T^* . For simplicity assume that the gas within the cloud can be described by the single absorption coefficient k_1 in the solar, but that it does not absorb in the infrared. The latter assumption is needed to avoid complications caused by the non-grey character of the water vapor spectrum in the longwave. Unlike in the NIR, exchange occurs over a wide range of path lengths in the longwave, and no single coefficient describes the absorption. Deep within the interior of the cloud absorption occurs mostly in the band centers, but near the upper boundary exchange occurs mostly in the transparent wings of the water vapor bands. A Planck mean coefficient would be suitable in the former situation, while a Rosseland mean would be needed in the latter. Since the two coefficients differ by three orders of magnitude, we ignore the gaseous absorption completely rather than complicate the argument by trying to patch the two regions together.

In radiative equilibrium $\partial F/\partial z=0$, and $F = \text{constant}$. We have

$$F = F_S + F_T \quad (4.1.15)$$

and in a homogeneous atmosphere

$$F_S = c_1 e^{\beta \tau_S} + c_2 e^{-\beta \tau_S} \quad (4.1.16)$$

where

$$c_1 = 2\sqrt{3} \mu_0 f \left(\sqrt{3} \left(\frac{1+\alpha}{1-\alpha} \right) - \beta \right) e^{-\beta \tau_S^*} / \Delta \quad (4.1.17)$$

$$c_2 = -2\sqrt{3} \mu_0 f \left(\sqrt{3} \left(\frac{1+\alpha}{1-\alpha} \right) + \beta \right) e^{-\beta \tau_S^*} / \Delta \quad (4.1.18)$$

and where

$$\Delta = (\sqrt{3}-\beta)\left(\sqrt{3}\left(\frac{1+\alpha}{1-\alpha}\right)-\beta\right)e^{-\beta z_s^*} - (\sqrt{3}+\beta)\left(\sqrt{3}\left(\frac{1+\alpha}{1-\alpha}\right)+\beta\right)e^{+\beta z_s^*} \quad (4.1.19)$$

We have also from (3.3.4)

$$\frac{d^2 F_T}{dz_T^2} = 3F_T - 2\pi\sqrt{3} \frac{dB}{dz_T} \quad (4.1.20)$$

Applying the operator $(\partial^2/\partial\tau_T^2 - 3)$ to both sides of (4.1.15) and using (4.1.20),

$$-3F = \left(\frac{d^2}{dz_T^2} - 3\right)F_s - 2\pi\sqrt{3} \frac{dB}{dz_T} \quad (4.1.21)$$

In a homogeneous atmosphere $\tau_S = \gamma\tau_T$, and (4.1.21) can be integrated once using (4.1.16) to yield

$$2\pi B = \left(\frac{\beta\gamma}{\sqrt{3}} - \frac{\sqrt{3}}{\beta\gamma}\right) \left(c_1 e^{\beta\gamma z_T} - c_2 e^{-\beta\gamma z_T}\right) + \sqrt{3}Fz_T + a_0 \quad (4.1.22)$$

where a_0 is a constant of integration, and is determined along with F from the boundary conditions at $\tau_T=0$ (3.3.5) and at $\tau_T=\tau_T^*$ (3.3.6). They are given by the solution of the system

$$\begin{pmatrix} 1 & \sqrt{3}z_T^*+1 \\ & -1 \end{pmatrix} \begin{pmatrix} a_0 \\ F \end{pmatrix} = \begin{pmatrix} 2\pi\beta^* + c_1 e^{\beta\gamma z_T^*} \left(1 + \frac{\sqrt{3}}{\beta\gamma}\right) + c_2 e^{-\beta\gamma z_T^*} \left(1 - \frac{\sqrt{3}}{\beta\gamma}\right) \\ c_1 \left(\frac{\sqrt{3}}{\beta\gamma} - 1\right) - c_2 \left(\frac{\sqrt{3}}{\beta\gamma} + 1\right) \end{pmatrix} \quad (4.1.23)$$

The solutions to (4.1.22) and (4.1.23) depend only on the opacity of the cloud τ_T^* , the temperature of the lower boundary T^* , and the parameter $\beta\gamma/3^{1/2}$. In most of our calculation $\beta\gamma/3^{1/2} \sim 0.07$ and our solutions are characteristic of a greenhouse-type atmosphere (Gierasch and Goody, 1970), and occur when solar heating occurs significantly below the region of maximum thermal emission.

The radiative equilibrium temperature profiles corresponding to

the solution of (4.1.22) are plotted in Fig.4.6 for several values of τ_T^* . The temperature T^* of the lower boundary is fixed at 273 K, $\beta\gamma/3^{1/2} = .07$, and $\alpha=0$.

In equilibrium the upper regions of the cloud become progressively warmer with increasing τ_T^* , and the interior becomes very warm as less longwave radiation is able to escape to space. For $\tau_T^* \gtrsim 7.5$ the interior actually becomes warmer than 273 K, but the temperature decreases as the lower boundary is approached. In these cases the solar radiation is trapped in the interior to cause heating, but cannot penetrate far enough into the cloud to counteract the cooling at the boundary. Consequently, a cold-warm-cold structure develops, and if the interior becomes so warm that $T(\tau_T) \gtrsim T_d(\tau_T)$, that portion of the cloud must evaporate since, by definition, a cloud is said to exist wherever $T < T_d$.

The broken line in Fig.4.6 illustrates the lapse rate of T_d in an atmosphere with constant mixing ratio. From (4.1.1)

$$\left(\frac{\partial T_d}{\partial z} \right)_{r_v} = -\frac{g}{L_v} \frac{R_v}{R} T \quad (4.1.24)$$

or about -1.7 K km^{-1} for $T = 263$. The actual dew point profile would be displaced by some constant value depending upon the absolute value of r_v . That portion of the cloud that exceeds the dew point temperature will simply burn out.

Although this is a very oversimplified picture insofar as the radiative equilibrium profiles will change once the cloud becomes inhomogeneous, it does suggest a plausible mechanism for the generation of a clear interstice. Longwave cooling exceeds solar heating at the top of the cloud and is therefore able to maintain a state of condensation, while at the same time the interior is heated past its saturation temperature and evaporates.

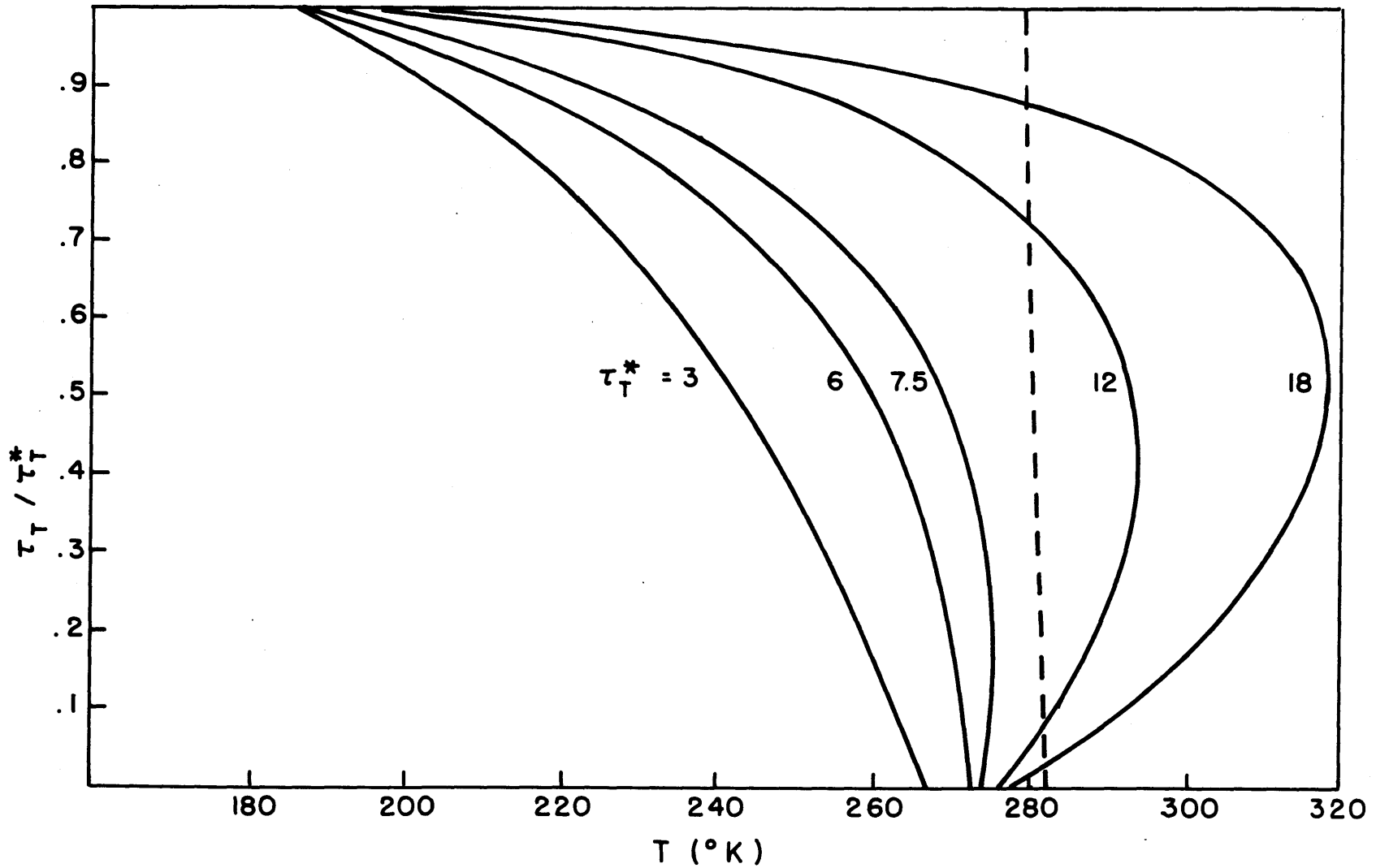


Fig. 4.6 Radiative equilibrium temperature profiles. Profiles are for selected values of the thermal optical depth τ_T^* . In this calculation $\beta\gamma/\sqrt{3} = .07$ and $T^* = 273$ K. The broken line illustrates the slope of the saturation temperature in an atmosphere with constant mixing ratio.

We may speculate that it is perhaps fortuitous that we observe such a thing as a liquid water stratus cloud at all. If the optical properties of liquid water were such that solar radiation were absorbed over relatively smaller thermal optical depths ($\beta\gamma/3^{1/2} > 1$) clouds could not exist because infrared radiation would be unable to balance the solar heating at the top. The cloud would simply burn off from the top.

4.1.4 Radiative Processes

The results from Case VI suggest that the role of turbulence in initiating and maintaining a multilayered stratus cloud may be secondary to that of radiation. The radiation field consists of longwave radiation by both the cloud and the gas, and solar radiation that is scattered and absorbed by the cloud droplets and absorbed by the gas. In order to discover which component or components are responsible for the structure of the clouds, we consider a set of hypothetical atmospheres for which the conditions are identical to those in Case I except for selected components of the radiation field.

Case VII. No radiation. In this case (Fig.4.7) the atmosphere had realistic turbulent fluxes of heat and moisture, but the extinction coefficients of the cloud were set to zero, as were the gaseous absorption coefficients. Condensation occurred at 600 meters and could only be due to the eddy-diffusive transport of heat down to the colder surface. The cloud became slightly more dense with time, but the maximum liquid water mixing ratios were only half of those found at the top of the radiating clouds. The cloud base slowly descended with time as a result of particles falling into the colder sub-cloud region.

Since cooling to space was absent in this case it took approximately two days longer for condensation to first occur, a result that was

suggested by analysis of Sect.4.1.2.

No layering or separation occurred.

Case VIII. Radiatively inactive gas. Here the cloud was assigned its Planck mean extinction parameters, but the absorption coefficients of the gas remained equal to zero. Condensation occurred at the same time as in Case VII since the mechanism for initiation was the same. The cloud top cools directly to space at a rate $Q_{\text{rad}}^T \sim -\pi(N_o \pi a^2 \overline{Q_a^T})B$ or about 30 deg K hour⁻¹. This extreme cooling was distributed through the sub-cloud region to the surface by convection, and the entire 2 km layer was rapidly brought to condensation. Convective turbulence was particularly intense in this cloud since it was driven by both a large heat flux into the base of the layer and a large flux out of the top.

The cloud became progressively denser as the cooling continued, and separation did not occur.

Case IX. Radiatively inactive condensate. The extinction efficiencies $\overline{Q_s^S}$, $\overline{Q_a^T}$ and $\overline{Q_a^S}$ were set to zero in this case, but the longwave emissivities and water vapor absorption coefficients in the NIR were calculated as usual. The cloud condensed early since the water vapor was able to cool to space, but the explosive growth of the cloud that was seen in Case VIII did not occur since the longwave emissivity of the layer was unaffected by the presence of the droplets. Liquid water mixing ratios remained close to those obtained in the basic state, and their relatively slow increase with time reflects the difference in the cooling to space time constants for a clear and cloudy atmosphere. The top of the cloud was tenuous since new condensate was continually being formed there; the droplet density throughout the rest of the cloud was fairly uniform and showed no tendency to thin out or separate.

Case X. Gas inactive in terrestrial spectrum. Here the gas absorbed solar but not longwave radiation, and the droplets were active in both regions. A cloud formed after six days and persisted but did not separate. The initiation of condensation was retarded because cooling to space was absent and solar heating counteracted the diffusive cooling to the surface.

Case XI. Gas inactive in solar spectrum. In this case the gas absorbed longwave radiation but not shortwave. The results here were most similar to the basic state in that a condensate rapidly formed and separated shortly thereafter. The analysis of the non-turbulent case (VI) suggested that continuous solar heating of the cloud interior could cause evaporation of the condensate there. That this heating should occur mostly in the droplets is not surprising, since we have already seen that the cloud absorption coefficient k_c exceeds the gaseous absorption coefficient k_g by a factor 27 over most of the spectrum. The only important differences caused by neglecting NIR gaseous absorption are that condensation occurred six hours earlier since the atmosphere was not heated as strongly, and that the rate of rise of the top layer was slightly retarded.

Case XII. Droplets inactive in solar spectrum. This further illustrates the importance of the droplet extinction of solar radiation. The results are similar to Case VIII in which longwave gaseous absorption was also neglected. Once the cloud had formed rapid growth occurred since there was no heating by the cloud droplets to compensate for the longwave loss from the top. Since the gaseous solar absorption was so weak compared to cooling to space of the droplets, the cloud persisted, became denser, and showed no tendency to separate. However, the important difference between this and Case VIII was that the cloud top rapidly lifted with time,

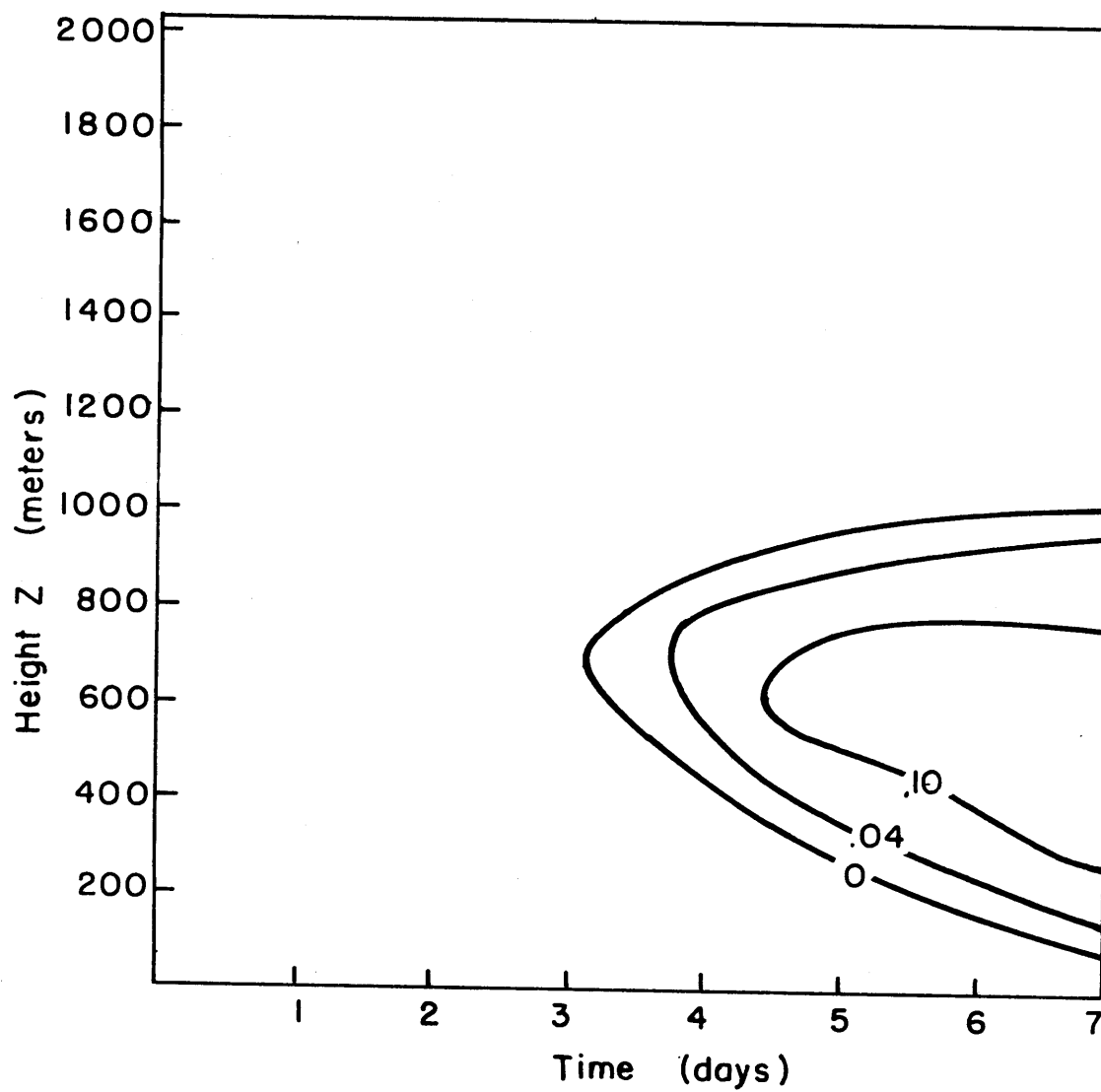


Fig. 4.7 Liquid water distribution for a hypothetical atmosphere with radiatively inactive constituents.

a feature that will later be attributed to longwave gaseous exchange.

The results of these hypothetical cases are summarized as follows: In the stable atmosphere condensation first occurred due to longwave emission to space by water vapor and diffusive cooling to the lower boundary, and solar gaseous absorption retarded condensation but did not prevent it. Once the condensate had formed the radiative regime was radically altered as the emission to space of the cloud droplets became important. This cooling was distributed through the cloud by convective turbulence and was only slightly diminished by the absorption of the gas within the cloud. Droplet absorption of solar radiation substantially compensated for the longwave loss in all regions except close to the cloud top, and was so great within the interior of the cloud that the droplets themselves evaporated.

These features are illustrated in Fig.4.8 in which we indicate the dominant two terms in the heat equation (2.2.6) for the various regions of the time vs. altitude domain, or alternatively, the horizontal distance vs. altitude domain.

Fig.4.8 corresponds to Case I, which is warmer air flowing over a colder surface. The terms heating and cooling refer to the local time rate of change of equivalent potential temperature; diffusive refers to the divergence of the flux of shear driven turbulence, while convective refers to the divergence of the flux of convective turbulence. The terms solar and IR refer to the divergences of the net solar flux F_S^{Net} and net thermal flux F_T^{Net} . The solar and IR zones in principle could both be subdivided to illustrate the relative contribution from the gases and from the cloud particles. This is not done in the present analysis, nor do we distinguish between the absorptive and emissive components of the IR term.

The IR-cooling zone of the upper left hand corner is the cooling of the upper regions of the boundary layer by direct longwave exchange with space. Diffusive-cooling and IR-cooling cool the boundary layer to condensation in slightly more than a day, and a zone of near-equilibrium between IR boundary exchange and diffusion is rapidly established close to the surface.

Once the condensate has formed the radiative regime is greatly altered by the absorptive properties of the droplets. The upper cloud layer becomes unstable due to the intensive longwave loss from the top of the cloud. A quasi-radiative-convective equilibrium state is established in the cloud layer, with convective warming balancing radiative cooling at the top, while the convective cooling balances the heating due to solar absorption in the interior. A region of intense radiative heating forms within the cloud interior by the greenhouse mechanism discussed earlier, and it is this that allows the development of the clear interstice.

After approximately three days the heating and cooling terms become small, and several quasi-equilibrium zones are established. Note especially that there are two radiative equilibrium zones located between radiative-diffusive or radiative-convective zones.

We may also note at this point that the concept of radiative zones separating radiative-turbulent zones has already been applied to other situations. In particular, it has been speculated that the Venus cloud layer may separate into two distinct turbulent regions separated by a radiative zone early in its solar day (Gierasch and Goody, 1970). However, in the Venus problem the radiative zone was caused by the diurnal variation of the solar heating and surface temperature. Our radiative equilibrium zones are associated with the absence of a diurnal cycle and the constancy of the

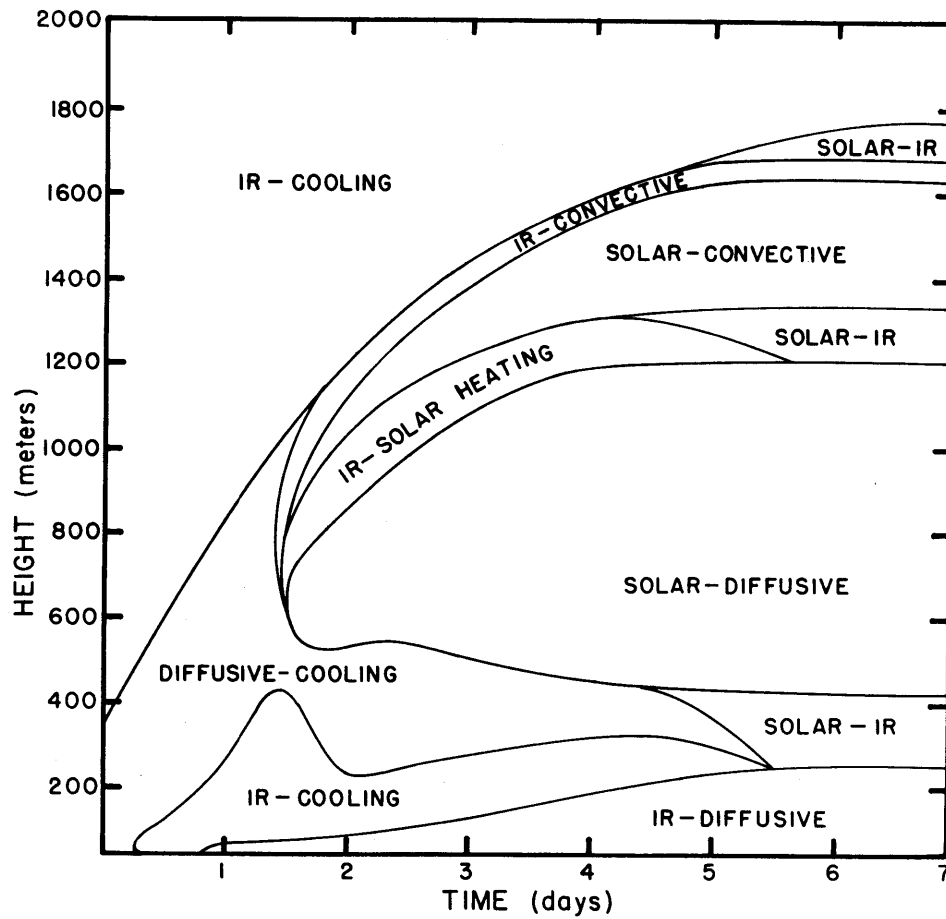


Fig. 4.8 Components of the radiative and turbulent regimes computed by model for Case I, warmer air flowing over a colder surface. Regions of diagram indicate dominant two terms in the entropy equation (2.2.6).

surface temperature in the summertime Arctic.

This diagram also serves to illustrate the validity of our linear set of equations (2.2.1)-(2.2.4). In the lowest 25m, where the departures from the basic current U_0 are the largest, the time derivative becomes small after about 18 hours, and this lowest layer comes under radiative and diffusive control. Although the transformation (2.2.5) is not strictly valid for this lowest layer, it is not important for most of the integration since radiation and diffusion are the dominant terms.

4.1.4.1 Diurnal Cycle

We have hitherto ignored the time variation of the solar zenith angle μ_0 to simplify the analysis. Including a time dependent μ_0 calculated with (3.2.23) alters some details but not the gross features of the results (Fig.4.9). At 80°N during July μ_0 is always positive, and the cloud is continually illuminated by solar radiation. The oscillation of μ_0 during the day causes a variation in the depth of the interstice and a slight variation in the height of the base. The interstice is widest at local solar noon and contracts to a minimum separation 12 hours later, and simply reflects the diurnal variation of the solar heating function. It will later be shown that it is the lack of a significant diurnal cycle in the summertime Arctic that allows the generation of a clear interstice. In seasons or at latitudes where approximate stationarity is never attained because of a large diurnal variation in the solar heating function, the cloud becomes dense at night and it not heated long enough during the day for the interior to evaporate.

4.1.4.2 Temperature Profiles

We have illustrated some of the temperature profiles obtained after 3 days of integration in Fig.4.10a, and the isotherms associated with Case I are shown in Fig.4.10b. The intensity of the inversion was most

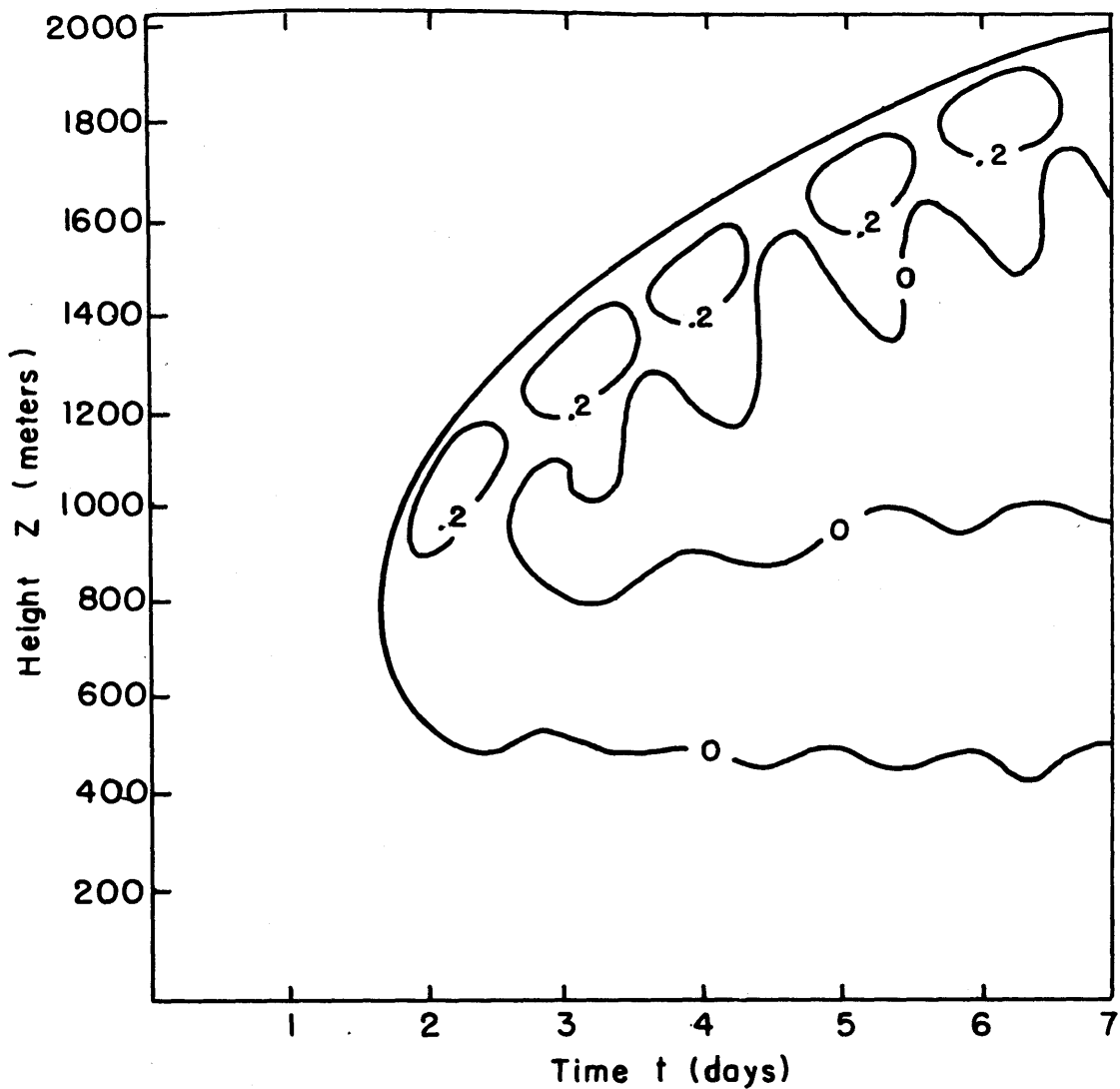


Fig. 4.9 Liquid water distribution as function of height and time for atmosphere with realistic variation of solar zenith angle corresponding to 80°N on July 15. Isolines are g kg^{-1} .

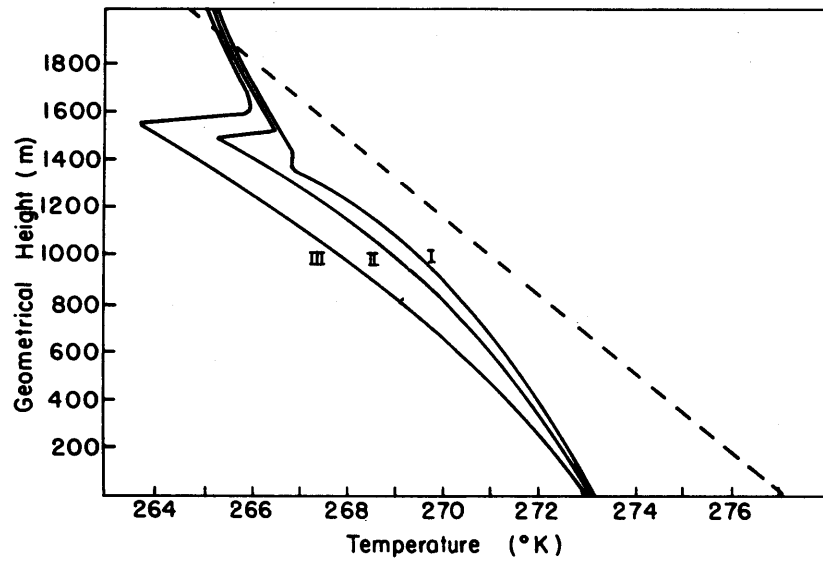


Fig. 4.10a Vertical temperature profiles obtained after 3 days of integration.

Curves I, II, and III correspond to $\chi_a^S = 2.9 \times 10^{-8} \text{ cm}^2$, $1.43 \times 10^{-8} \text{ cm}^2$, and $5.72 \times 10^{-9} \text{ cm}^2$, respectively.

Dotted line is initial temperature profile.

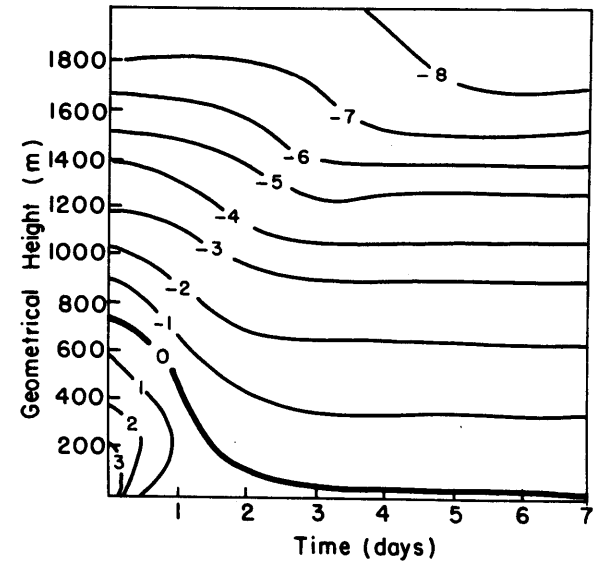


Fig. 4.10b Isotherms ($^{\circ}\text{C}$) corresponding to Case I.

closely related to our choice of the extinction parameter χ_a^S and this dependency is illustrated by curves I-III in Fig. 4.10a. Since the inversion is formed primarily due to the net cooling at the cloud top, factors which tend to increase the solar heating there should decrease the inversion strength. In fact, for $\chi_a^S = 3 \times 10^{-8}$, no inversion occurs, and only a shallow isothermal region is formed.

4.1.5 Variation of Parameters

To assure ourselves that we understand all of the variables that are important for the production and maintenance of a multi-layered stratus cloud we consider the systematic variation of the following parameters:

Longwave absorption cross-section χ_a^T (Table 4.1). The occurrence and initiation of condensation are, of course, independent of χ_a^T (and χ_a^S and χ_s^S as well). The initiation of layering is independent of χ_a^T for values larger than the Planck mean value computed according to (3.2.23), but is inhibited by smaller values. The depth of the cloud that cools strongly to space is $(N_o \chi_a^T)^{-1}$, or about 100 m for $N_o = 100$. Large χ_a^T isolate the cloud interior from the cooling at the top, and the solar heating dominates. As χ_a^T diminishes the interior is kept colder and separation is delayed. In fact at one tenth of the Planck mean value of χ_a^T it does not occur at all. Note also that the width of the interstice decreases at very large χ_a^T . This occurs because the cooling at the cloud top is so large that convection can penetrate to regions that were previously heated by solar radiation.

Solar absorption cross section χ_a^S . The importance of droplet absorption in determining the structure of the cloud is further illustrated in Table 4.2. With no droplet absorption and for very small values of χ_a^S the entire atmosphere rapidly becomes filled with liquid water. We have

suggested before that this is due to the fact that the large longwave cooling at the top is not compensated for by local heating within the cloud. As χ_a^S increases solar radiation is more effective in keeping the cloud warm, and droplet densities closer to what has been observed are obtained. For very large χ_a^S an extremely tenuous ($r_\ell \sim 0.01 \text{ g kg}^{-1}$) condensate forms, but cannot maintain itself against the strong solar heating. A very brief separation occurs, but does not persist since the entire cloud is thinning and will eventually dissipate in a longer integration.

These results suggest that the predicted structure of Arctic stratus rests rather precariously on a narrow range of values of the single parameter χ_a^S . We have computed χ_a^S from the data of Irvine and Pollack convoluted onto a 6000 K black body curve, and it is fair to ask how well such an approximation represents the true absorptive properties of a stratus cloud. We feel that we have adequately represented the cloud for the following reasons:

First, our calculated absorptance of 8% is within the range measured by Neiburger (7%) and by Koptev and Voskrezenskii (10%).

Second, in a set of calculations not shown here we attempted to calibrate our model against the heuristic model of Lilly (1968) of California coastal stratus. Using the same boundary and initial conditions that he used, but with our own radiative parameters we were able to generate a California stratus cloud that was consistent with Lilly's model and with the observations of Neiburger.

Finally, we may argue that our values of χ_a^S are an adequate representative of the radiative conditions in Arctic by the very fact that we obtain results consistent with the observed liquid water contents when we use our Planck mean value of χ_a^S , but obtain clouds that are much too dense

$(1 - 2g \text{ kg}^{-1})$ for smaller values, and clouds that are too tenuous for larger values.

Surface reflectivity α . Although the surface reflectivity rapidly diminishes with the onset of the melting season, the structure of the clouds is only slightly altered as seen in Table 4.3. Condensation occurs regardless of surface conditions, although it is negligibly faster over a dark surface and 3 hours slower over a bright one. Separation occurs in all cases, but is faster and produces a larger gap over a bright surface due to the increased solar radiation that is reflected back to the cloud.

Surface roughness z_0 (Table 4.4). The effect of varying the surface roughness, which would ultimately affect the fluxes of heat and moisture into the atmosphere, is negligible. Condensation is slightly inhibited over a very smooth surface since the downward transport of heat by mechanical turbulence is slower.

Mean vertical velocity w (Table 4.5). The mean rate of subsidence (or lifting) is an extremely uncertain parameter and was included in the model mainly because the results of Lilly (1968) indicated that w was an important parameter in determining the quasi-equilibrium structure of California maritime stratus, and we felt that its importance needed to be tested in the Arctic.

Earlier it was demonstrated that the time scale for heating or cooling due to large scale vertical motion in Arctic was very long compared to the radiative or turbulent time scales, although this was not the case at lower latitudes. The effect on the cloud structure is illustrated in Table 4.5. For weak subsidence or even weak lifting the layered structure is maintained although the fine structure is slightly altered by the extra heating or cooling. However, with the value of w that Lilly needed to

Table 4.1

Cloud conditions for various absorption cross section, $\chi_a^T = \overline{Q_a^T} \pi a^2$

Absorption cross section ($\chi_a^T = 9.16 \times 10^{-7} \text{ cm}^{-2}$)

	$10\chi_a^T$	$2\chi_a^T$	χ_a^T	$\frac{1}{2}\chi_a^T$	$\frac{1}{10}\chi_a^T$	0
I. Development						
a) Occurrence of condensation	+	+	+	+	+	+
b) Initiation of condensation (hrs)	34	34	34	34	34	34
c) Occurrence of layering	+	+	+	+	-	-
d) Initiation of layering (hrs)	66	66	66	75	-	-
II. Quasi-equilibrium structure						
a) h_1	550	500	500	350	350	450
b) h_2	1200	1050	1050	1050	—	—
c) h_3	1350	1450	1450	1350	—	—
d) h_4	1700	1700	1700	1700	1250	1250
e) Cloud top temperature °C	-8.7	-8.2	-8.2	-8.0	-6.2	-4.1

Table 4.2

Cloud conditions for various solar absorption cross-sections $\chi_a^S = \overline{Q_a^S} \pi a^2$

Absorption cross section ($\chi_a^S = 2.86 \times 10^{-8} \text{ cm}^2$)

	$10\chi_a^S$	χ_a^S	$\frac{1}{2}\chi_a^S$	$\frac{1}{5}\chi_a^S$	$\frac{1}{10}\chi_a^S$	0
I. Development						
a) Occurrence of condensation	+	+	+	+	+	+
b) Initiation of condensation (hrs)	34	34	34	34	34	34
c) Occurrence of layering	+	+	+	—	—	—
d) Initiation of layering (hrs)	125*	66	83	—	—	—
II. Quasi-equilibrium structure						
a) h_1	550	500	200	550	0	0
b) h_2	—	1050	1200	—	—	—
c) h_3	—	1450	1400	—	—	—
d) h_4	900	1700	1900	2050*	2050**	2050**
e) Cloud top temperature °C	-2.8	-8.2	-10.3	-15	-16	-18

* layering occurs but does not persist

** upper boundary of model

Table 4.3

Cloud conditions for varying surface reflectivity α

	$\alpha =$.01	.4	.95
I. Development				
a) Occurrence of condensation		+	+	+
b) Initiation of condensation (hrs)		33	34	37
c) Occurrence of layering		+	+	+
d) Initiation of layering (hrs)		66	66	58
II. Quasi-equilibrium structure				
a) h_1		450	500	600
b) h_2		1100	1050	900
c) h_3		1450	1450	1550
d) h_4		1700	1700	1750
d) Cloud top temperature °C		-8.3	-8.2	-8.3

Table 4.4

Cloud conditions for varying surface roughness z_o

	$z_o = .1 \text{ cm}$		
	$10 z_o$	z_o	$z_o/100$
I. Development			
a) Occurrence of condensation	+	+	+
b) Initiation of condensation (hrs)	34	34	35
c) Occurrence of layering	+	+	+
d) Initiation of layering (hrs)	66	66	66
II. Quasi-equilibrium structure			
a) h_1	500	500	500
b) h_2	1100	1050	1000
c) h_3	1450	1450	1450
d) h_4	1700	1700	1700
e) Cloud top temperature °C	-8.2	-8.2	-8.2

Table 4.5

Cloud conditions for varying mean vertical velocities, w

$$w(z) = Az$$

$$A = \quad -5 \times 10^{-6} \quad -4 \times 10^{-7} \quad -1.4 \times 10^{-7} \quad 0 \quad +1.4 \times 10^{-7}$$

I. Development

a) Occurrence of condensation	—	+	+	+	+
b) Initiation of condensation (hrs)	—	37	34	32	31
c) Occurrence of layering	—	+	+	+	+
d) Initiation of layering (hrs)	—	58*	66	66	58

II. Quasi-equilibrium structure

a) h_1	—	550	500	500	450
b) h_2	—	900	1050	1200	1300
c) h_3	—	1100	1450	1800	1750
d) h_4	—	1400	1700	2000**	2000**
d) Cloud top temperature °C	—	-6.9	-8.2	-9.5	-9.3

* layers do not persist

** upper boundary of model

Table 4.6

Cloud conditions for various initial stabilities, $N^2 = g/\theta \partial\theta(z,0)/\partial z$

	$N^2 =$	3.6×10^{-5}	3.6×10^{-4}	1.8×10^{-4}
I. Development				
a) Occurrence of condensation		+	+	+
b) Initiation of condensation (hrs)		34	44	39
c) Occurrence of layering		+	+	+
d) Initiation of layering (hrs)		66	66	92
II. Quasi-equilibrium structure				
a) h_1		500	450	450
b) h_2		1050	1300	1200
c) h_3		1450	1650	1700
d) h_4		1700	2050	2050
e) Cloud top temperature °C		-8.2	-2.2	-7.0

maintain equilibrium in his model, we were unable even to induce condensation. That value of w was computed for a latitude at which the vertical motion due to the sinking branches of the Hadley and Ferrel cells was near a maximum, whereas at high latitudes even the sign of w is uncertain. It is interesting to speculate at this point that a multilayered stratus cloud can persist for so long in the summertime Arctic and not elsewhere partly because the mean vertical velocities there are so small. If the direct polar cell was substantially more intense, Arctic stratus would simply dissipate.

Initial stability, N^2 (Table 4.6). Cloud conditions under quasi-steady conditions are relatively independent of our assumptions about the initial stability of the air mass, although the initiation of separation is somewhat retarded under extremely stable conditions.

4.1.6 Properties of the Upper Cloud Layer

All models that contained both radiatively active gases and condensates had the peculiar feature that the height of the upper boundary could never reach a stationary state, but instead lifted very slowly with time. In a convective cloud layer we would expect the cloud top to grow with the mixed layer, and this is borne out by the calculations of Lilly (1968, Fig.1) and others. However, this is also a persistent feature in most of the non-convective calculations, and in fact even occurs in a purely radiative atmosphere (Case VI).

Since this appears to be a radiative effect, we consider the approximate expression (3.3.24) for the rate of cooling of the supra-nebulous region in the presence of solar radiation,

$$\rho C_p \frac{\partial T(z,t)}{\partial t} = -\rho_w(z) \pi [B(z) (\epsilon'(u_w^*) + \epsilon'(u_u^*)) + B_c(z) \epsilon'(u_u^*)] + Q_{rad}^s(z) \quad (4.1.25)$$

Since the lower boundary is now the upper surface of the cloud, $\epsilon'(u_u^*)$ is the derivative of the emissivity between the level z , and at the cloud top, $\pi B_c = \sigma T_c^4$ where T_c is the cloud top temperature. This may also be written

$$\frac{\partial B(z,t)}{\partial t} = \frac{G\Gamma_v(z)}{c_p} \left\{ -B(z,t)(\epsilon'(u_{u_0}^*) + \epsilon'(u_u^*)) + B_c(t)\epsilon'(u_u^*) \right\} + Q_{rad}^S(z) \quad (4.1.26)$$

here $G = 4\sigma\bar{T}^3$, where \bar{T} is some mean temperature. The solution to (4.1.26)

is*

$$B(\bar{T}, z) \exp\left(\frac{G\Gamma_v(z)}{c_p} \int_0^{\bar{T}} (\epsilon'(u_{u_0}^*(t')) + \epsilon'(u_u^*(t'))) dt'\right) - B(0, z) \\ = \int_0^{\bar{T}} dt \left[\frac{G\Gamma_v}{c_p} B_c(t)\epsilon'(u_u^*(t)) + \frac{GQ_{rad}^S}{\pi p c_p} \right] \exp\left(\frac{G\Gamma_v(z)}{c_p} \int_0^t (\epsilon'(u_u^*(t')) + \epsilon'(u_{u_0}^*(t'))) dt'\right) \quad (4.1.27)$$

Here $B(\bar{T}, z)$ corresponds to the temperature at some time \bar{T} , and the arguments of the exponentials on both sides of (4.1.27) account for the fact that the distance from z to the height of the top of the cloud z_c is changing with time in the terms $\epsilon'(u_u^*)$.

Equation (4.1.25) implies, of course, that if the net cooling due to exchange with space and exchange with the boundary of the cloud exceeded the solar heating functions Q_{rad}^S the local temperature would decrease. Since, however, the air above the cloud contains some non-zero water vapor concentration, after some period of time it too will be brought to condensation and therefore the cloud boundary will effectively be lifted to some new height.

When the cloud top is at some height $z_c(t)$ we have $B_c(t) \leq B_d(z_c(t))$ where B_d corresponds to the dew point temperature T_d . This follows

* The solution to 4.1.26 and the following asymptotic forms were kindly provided by Professor R.M. Goody.

since we have defined a cloud to exist when supersaturation is reached. The inequality will generally hold since the cloud itself will in most cases be cooling to space, but we shall assume $B_c = B_d$. Moreover, at some later time $\tilde{\tau}$ the cloud will arrive at $z = z_c(\tilde{\tau})$ when $B(\tilde{\tau}, z) = B_d(z_c(\tilde{\tau}))$. The time $\tilde{\tau}$ it takes the cloud to reach some level z is thus given by

$$\begin{aligned}
 & B_d(z_c(\tilde{\tau})) \exp \frac{G \Gamma_v(z)}{c_p} \int_0^{\tilde{\tau}} [\epsilon'(u_{\infty}^*(z_c(\tilde{\tau}))) + \epsilon'(u_n^*(z_c(\tilde{\tau}), z_c(t')))] dt' - B(0, z_c(\tilde{\tau})) \\
 &= \int_0^{\tilde{\tau}} dt \left[\frac{G \Gamma_v(z)}{c_p} (B_d(z_c(t)) \epsilon'(u_n^*(z_c(\tilde{\tau}), z_c(t))) + \frac{G Q_{rad}^s(z_c(t))}{\pi p c_p} \right] \times \quad (4.1.28) \\
 & \exp \frac{G \Gamma_v(z_c(\tilde{\tau}))}{c_p} \int_0^t (\epsilon'(u_{\infty}^*(z_c(\tilde{\tau}))) + \epsilon'(u_n^*(z_c(\tilde{\tau}), z_c(t')))] dt'
 \end{aligned}$$

Although this equation can be solved by standard iterative techniques, we consider short time periods such that the arguments of the exponentials in (4.1.28) are small, whence

$$\begin{aligned}
 & B_d(z_c(\tilde{\tau})) \left(1 + \frac{G \Gamma_v}{c_p} \epsilon'(u_{\infty}^*(z_c(\tilde{\tau}))) \tilde{\tau} - B(0, z_c(\tilde{\tau})) \right) \\
 &= \int_0^{\tilde{\tau}} dt \frac{G \Gamma_v}{c_p} \left\{ (B_d(z_c(t)) - B_d(z_c(\tilde{\tau}))) \epsilon'(u_n^*(z_c(\tilde{\tau}), z_c(t))) + \frac{Q_{rad}^s(z_c(t))}{\pi p w} \right\} \quad (4.1.29)
 \end{aligned}$$

if exchange with the lower boundary and solar heating are small compared with cooling to space, the right hand side of (4.1.29) can be ignored, and

$$\tilde{\tau} = \frac{B(0, z_c(\tilde{\tau})) - B_d(z_c(\tilde{\tau}))}{\frac{G \Gamma_v}{c_p} B_d(z_c(\tilde{\tau})) \epsilon'(u_{\infty}^*(z_c(\tilde{\tau})))} \quad (4.1.30)$$

For example, we may consider the time $\tilde{\tau}$ it would take a cloud top to extend itself 500 m if it were initially at 1000 m if the dew point depression at $z_c(\tilde{\tau})$ were 2 K. Here $\epsilon'(u_{\infty}^*) \sim .2 \text{ cm}^2 \text{ g}^{-1}$, and we let $T_d = 260 \text{ K}$. With $r_v = .003$ we obtain $\tilde{\tau} = 36$ hours.

Alternatively, if boundary exchange and solar heating were large, we could ignore the term involving $\epsilon'(u_{\infty}^*)$. However, we first note that for

moderately long path lengths $\varepsilon \sim A_0 \log u$, so $\varepsilon'(u) \sim A_0/u$, where A_0 is a constant equal to about 0.1. Also $u_w^* = \rho_w(z_c(\bar{T}) - z_c(t))$. The variation in B is linearized by writing

$$B_d(z_c(t)) - B_d(z_c(\bar{T})) = \overline{dB_d/dz} (z_c(t) - z_c(\bar{T})) \quad (4.1.31)$$

where $\overline{dB/dz}$ is some mean gradient. Then

$$B_d(z_c(\bar{T})) - B(0, z_c(\bar{T})) = \int_0^{\bar{T}} dt \frac{G \tau}{c_p} \left[\frac{Q_{rad}^s(z_c(t))}{\pi \rho_w} - \frac{A_0}{\rho_w} \frac{dB_d}{dz} \right] \quad (4.1.32)$$

or

$$\bar{T} = \rho_w c_p \frac{B_d(z_c(\bar{T})) - B(0, z_c(\bar{T}))}{G \left(\frac{Q_{rad}^s}{\pi} - A_0 \frac{dB_d}{dz} \right)} \quad (4.1.33)$$

Since $B_d < B(0, z_c(\bar{T}))$ in the clear atmosphere and $\overline{dB/dz}$ is normally negative, this implies a negative value for \bar{T} . Solar radiation and boundary exchange thus tend to counteract the loss to space, and retard radiative lifting. Combining the two contributions we obtain

$$\frac{B(0, z_c(\bar{T})) - B_d(z_c(\bar{T}))}{\bar{T}} = \frac{G A_0 B_d(z_c(\bar{T}))}{\rho_w c_p} \left\{ \frac{\rho_w}{u_{\infty}^*(z_c(\bar{T}))} + \frac{1}{B_d(z_c(\bar{T}))} \frac{dB_d}{dz} - \frac{Q_{rad}^s}{\pi A_0 B_d(z_c(\bar{T}))} \right\} \quad (4.1.34)$$

In a typical Arctic atmosphere $\rho_w/u_{\infty}^* \sim 7.5 \times 10^{-6} \text{ cm}^{-1}$. In the absence of solar heating this implies a critical lapse rate of dew point temperature of $\overline{T}_{\rho_w}/4u_{\infty}^*$, or about 44 K km^{-1} . Alternatively, solar heating in excess of $A_0 B_d \rho_w/u_{\infty}^*$ or about $0.2 \text{ ergs cm}^{-3} \text{ sec}^{-1}$ ($1.6 \text{ deg K day}^{-1}$) would prevent the cloud top from rising. The former condition is almost always satisfied since $B_d^{-1} \partial B_d / \partial z \sim 10^{-7}$ in an atmosphere with constant mixing ratio at 263 K. However, the small solar heating rates that would allow radiative lifting effectively limit this process to a polar atmosphere, where the heating rates are small because the solar elevation is so low, or to the night time when solar

heating is zero.

4.2 GEOGRAPHICAL EFFECTS

4.2.1 Persistence

Having considered the processes which determine the structure of Arctic stratus, we are now in a position to consider explanations that may account for some of the large-scale features of Arctic Stratus. In particular, what should be peculiar to the physics of the summertime Arctic that allows stratus clouds of horizontal extent of up to 2000 km to persist for periods of time so long that they appear as quasi-permanent climatological features?

We approach this question by considering the processes that act to destroy stratus clouds; namely, they may precipitate out, be dissipated due to the absorption of solar radiation, evaporate due to convective heating of the boundary layer, or be destroyed or altered by large scale synoptic activity.

The first process should not be an important factor in the life cycle of Arctic stratus. Precipitation that often accompanies Arctic stratus is usually in the form of mist or drizzle, and should not represent a significant sink of liquid water. In fact, the measurements of Sverdrup indicate that the 24 hour precipitation under Arctic stratus was often less than 0.1 mm. These small precipitation rates are a consequence of the low temperatures, small drop sizes, and shallow vertical depths of Arctic stratus. The first factor prohibits high liquid water concentrations, while the latter two factors are unfavorable for the formation of drops large enough to precipitate to the surface (Mason, 1957, p.235). For comparison we may note that the mean evaporation for the total Polar Ocean for June, July, and August from the data of Vowinckel and Orvig (1970) is 0.25 mm/day.

The water vapor advected into the Polar Ocean during that same period and from the same data source is 0.37 mm/day. The depletion of total water due to precipitation is therefore small but non-negligible compared to the evaporative and advective sources.

The ubiquitousness of Arctic stratus can thus be explained on the following basis: The invasion of warm air masses from the south is a frequent occurrence in the summertime Arctic, and in these air masses condensation is induced in slightly more than one day by cooling to space and diffusive cooling to the surface. Once the condensate forms, it must remain, since the dissipative mechanisms that are present in mid-latitudes are either absent or weakened in the Arctic: Precipitation is slight, solar radiation is too weak to burn off the cloud, the melting ice surface prohibits convection, and synoptic activity is sluggish compared to other latitudes.

The second and third processes are difficult to separate in most situations because the incident solar radiation will act to heat the cloud layer directly as well as heat the surface. This is evident in the diurnal cycles of both the California coastal fogs and the wintertime fogs of the California valleys. The former has been described by Neiburger (1944) and the latter by Lockhart (1943). In both cases the liquid water content is greatest at night, but decreases uniformly with increasing solar elevation. The valley fogs, moreover, follow a seasonal cycle of insolation: They occur most frequently during the winter when insolation is weakest, but do not occur during the other seasons.

In the summertime Arctic, however, the surface temperature remains fixed regardless of the amount of solar radiation deposited, since all of the energy is expended in melting the ice. Convection due to surface heating does not occur, and any dissipation is due to solar absorption.

The lack of dissipative processes is evident in our calculations by the fact that the clouds persist. Moreover, we considered an additional case (XIII) in which all of the conditions of Case I were retained, except that the mean solar zenith angle was set at 55° . The resulting condensate did not completely burn off, but the integrated liquid water at equilibrium was only .27 of that obtained when we considered the solar elevation of Case I. Absorption of solar radiation by the cloud is therefore an important component of the dissipation process, and its effects will be augmented by surface heating.

The final dissipative process, large-scale synoptic systems, is difficult to assess for reasons that were discussed in Chapter 2. However, stationarity in the synoptic flow favors persistence, and the analyses of Hare and Orvig (1958, p.98) and of Reed and Kunkel (1960) indicate that persistence is indeed the case in the Arctic. In fact, in the former analysis a value of six days was quoted as the period of persistence of the large-scale flow.

4.2.2 Separation

Having suggested an explanation for the peculiar features of summertime Arctic stratus we are obviously forced into the position of determining why these conditions are apparently limited to the Arctic, and are not found elsewhere. In particular, why do mid-latitude stratus clouds not exhibit layering?

We have already suggested that a multilayered stratus cloud can be viewed as a single stratus cloud layer that has suffered incomplete dissipation by solar radiation. The failure of mid-latitude fogs and stratus to layer is therefore likely to be associated with differences of the solar radiation fields within clouds at high and mid-latitudes. There are a

number of possibilities.

First, the optical properties of the water drops could be different, but surprisingly, this is not the case. Neiburger (1949) regularly found that the drop diameters in California stratus had a single well-pronounced mode in the 13-15 μ group, and this is exactly what has been measured in Arctic stratus (Table 1.3). It is likely that California stratus has more dry aerosol embedded in it, but this would probably augment solar heating rather than diminish it.

Second, California stratus clouds tend to be more opaque since they ordinarily have more liquid water in them. Neiburger obtained an average value of 0.40 g m⁻³ for all of his flights, while the values in the Arctic are about one-half of that. It is conceivable that a very opaque cloud could shield its interior from solar dissipation, but when we considered a hypothetical arctic atmosphere (Case XIV) with surface temperature and specific humidity that were typical of Southern California, layering still occurred. (In this particular calculation we used $T_o = 283$ K, $r_{v_o} = r_s(283)$.) A factor of two in the opacity is therefore too small to make an important difference.

Third, the maximum intensity of solar radiation is much greater in the California case since μ_o is large. We can see the effect of the solar flux by performing a non-convective calculation with a mean solar zenith angle of 42° (Case XV). A layered cloud still resulted, although the depth of the layers and the droplet densities were both somewhat diminished in the two layers. The magnitude of the solar flux does not therefore appear to be a significant factor for generating an interstice.

Finally, there is the duration of the solar radiation. We have seen from Chapter 1 that at 80°N the sun remains above the horizon for 24

hours a day from May through August, while at 40°N the sunlit day is only about 12 hours in June. Consequently, a large diurnal effect is to be expected.

We saw in Fig.4.9 that the small oscillation of the solar zenith at 80°N caused an oscillation in the depth of the interstice and also of the height of the base. The mechanism is straightforward: The cloud interior is heated less strongly at low solar elevations, and the cooling at the top can be carried farther into the interior by convective mixing. If the cooling at the top is strong enough, and if the solar heating is weak enough, the upper layer will merge with the lower layer and no interstice will appear.

Hence at more southerly latitudes solar heating within the cloud interior is zero for a substantial part of the day. In the absence of large-scale dynamical effects the cloud would become thicker at this time, and might become so thick that solar radiation could not dissipate it within the next 12 hour period. It is this diurnal behavior of the radiation field, for example, that gives rise to the peculiar periodicity in the thickness of the wintertime inversion fog that is frequently encountered in the San Joaquin and Sacramento Valleys.

The effect of the diurnal cycle is illustrated by Cases XVI and XVII, and these results are shown in Fig.4.11a and 4.11b. In the former case we applied the solar flux sinusoidally over a 12 hour period so that when integrated over a 24 hour day the total flux would be the same as in Case I. The resultant cloud layer remains thick and unbroken for the duration of the integration, except for a number of small, transient clear regions that appear. In the latter case we set the latitude equal to 40°N in the calculation of $\mu_0(t)$, and did not require that the integral fluxes

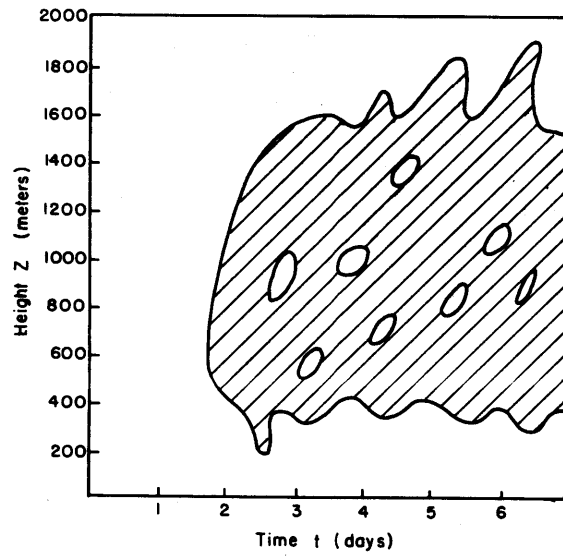


Fig. 4.11a Cloud distribution for same integrated flux as Case I, but applied sinusoidally over 12 hour period.

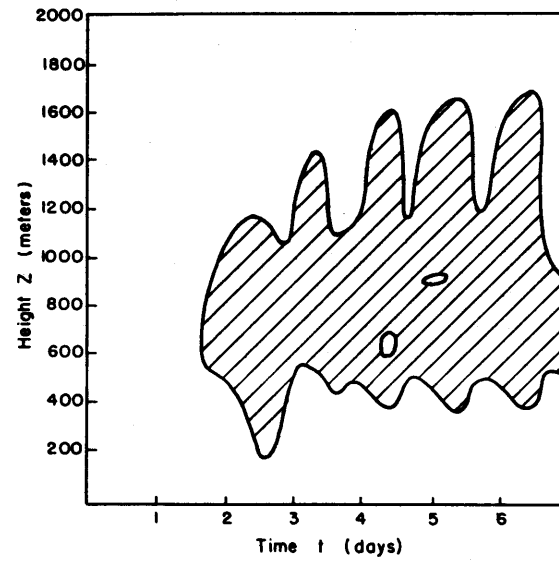


Fig. 4.11b Cloud distribution for solar zenith angle corresponding to 40°N in July.

be equal. The results are similar to Case XVI, except for the faster rate of rise of the upper surface. The oscillatory behavior of the upper boundary reflects the radiative expansion of the cloud layer when the sun goes below the horizon by the mechanism discussed in Sect.4.1.6.

It therefore appears that it is the near-steady conditions of the radiation field in the summertime Arctic that allows the development of clear interstices within a stratus layer.

4.2.3 Other effects

In addition to the near constancy of the solar elevation, it is likely that the quasi-steady cloud conditions are also due in part to the relatively minor role that large scale dynamics plays. We have already seen that intense subsidence would inhibit the formation of Arctic stratus, while in a convective marine layer it is a necessary element of the steady state. Neiburger has suggested that the diurnal behavior of the marine layer of stratus near the coast is dominated by local circulations such as the sea breeze. We might expect such processes to be important near the Arctic coast, since a substantial temperature discontinuity does exist between the cold polar oceans and the adjacent continents. This is a very local process, however, and would be limited to a horizontal scale of only 10-20 km, as the results of Walsh (1975) have indicated.

It is reasonable to ask why stratus clouds are not a persistent feature of the climates of Greenland or Antarctica, since their surfaces also consist of melting ice during their summer seasons. It is likely that orography is the dominating factor in these cases since a steady cloud would be difficult to maintain in the presence of katabatic winds. Moreover the Greenland continent is characterized by a strong anticyclone, which would imply a region of intense large-scale subsidence, and it also lies mostly

south of the Arctic Circle so that there would be a substantial diurnal cycle in its radiation field. We have seen that neither of these factors are favorable for the initiation or maintenance of stratus layers.

4.3 SEASONAL BEHAVIOR

In seeking to explain the annual march of low cloudiness in the Arctic (Fig.1.1) it is tempting to appeal to the annual march of surface temperature which almost certainly exerts an influence on the liquid water content of the atmosphere. The surface temperature should be important since the saturation vapor pressure at the surface follows the Clausius-Clapeyron equation. The temperature effect is illustrated in Fig.4.12 in which all other factors retained their basic state values, except the temperature at the surface. The solid curve is the annual march of surface temperature over the pack ice, and the dotted line is the integrated liquid water of the boundary layer, R , given by

$$R = \int_0^{z_T} r_l(z') dz' \quad (4.1.35)$$

which was computed with the model. Admittedly there is not a great deal of correspondence between the total water in a vertical column and the frequency of cloudiness, but this example does illustrate that very low temperatures are associated with extremely low liquid water contents. This explanation for the seasonality of Arctic stratus has already been offered by Sverdrup.

There are other meteorological parameters that show pronounced seasonality in the Arctic, and not all of them can be treated with this simple boundary layer model since they are problems associated with the general circulation. For example, the mean specific humidity at 75° (Oort and Rasmussen, 1971) is a maximum in July (1.6 g kg^{-1}) and a minimum in

January (0.3 g kg^{-1}), which is reasonable since the mean temperature for the lowest 500 mb is -1.8°C in July and -25.4°C in January. If we attempt to associate the annual variation of cloudiness with the variation of tropospheric temperatures, we are then confronted with the more difficult problem of explaining the seasonal variation in the atmospheric heat transports.

There is another contributing factor, but unfortunately we cannot simulate it with the present model because the surface temperature is specified rather than computed as a function of the surface energy balance. It is possible that extensive layers of stratus do not form during the other seasons because then the normal dissipative mechanisms are, in fact, operating. The calculations of Vowinckel and Taylor (1965) indicate that the sensible heat flux over the Polar Ocean, which we infer as an index of convective activity, is a maximum during the spring and fall. This occurs when the sun is above the horizon, but before and after the melting season. These circumstances may generate convective heating of the boundary layer, a condition which we have already suggested is unfavorable for the maintenance of stratus. During the winter months evaporation is very small or negative, and thus there is no local source of water present. Moreover, even if there were an evaporative source, it is likely that there would be no mechanism for transporting the water vapor into the surface layer. The surface layer in the winter is characterized by a very intense surface inversion and we have seen in Chapter 3 that large, positive temperature gradients suppress shear turbulence. Although radiation could still transfer heat, there could be no turbulent transport of water vapor.

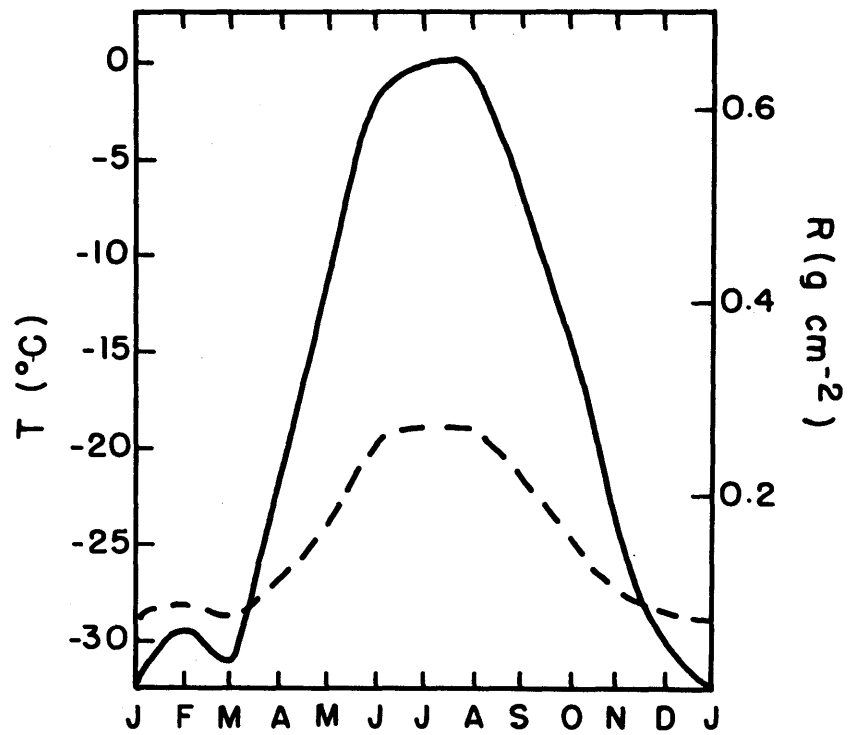


Fig. 4.12 Annual march of the temperature of the pack ice (solid line), and the integrated liquid water content R computed by model (broken line).

APPENDIX A; MOIST THERMODYNAMICS

The relationship between the specific entropy and the equivalent potential temperature is illustrated by the following consideration:

For a pseudo-adiabatic process (so called because we do not consider the thermodynamic properties of the liquid water which may be present) we have (von Bezold, 1888)

$$(1+r_v)(C_p' d \ln T - R' d \ln p) + L_v d \left(\frac{r_v}{T} \right) = 0 \quad (\text{A1})$$

where r_v is the saturation mixing ratio at temperature T and pressure p , L_v is the latent heat of vaporization of water, and C_p' and r' are the specific heat and gas constant for moist air, respectively. We have

$$C_p' = \left(\frac{1 + 1.869 r_v}{1 + r_v} \right) C_p \sim C_p \quad (\text{A2})$$

and

$$R' = \left(\frac{1 + 1.609 r_v}{1 + r_v} \right) R \sim R \quad (\text{A3})$$

where C_p and R are the values for dry air. Then approximately,

$$C_p d \ln T - R d \ln p + L_v d \left(\frac{r_v}{T} \right) = 0 \quad (\text{A4})$$

Integrating from some reference state, which we denote by the subscript "oo"

$$C_p \ln T/T_{oo} - R \ln p/p_{oo} + L_v \left(\frac{r_v}{T} - \frac{r_{v_o}}{T_{oo}} \right) = \text{constant} \quad (\text{A5})$$

If we define the reference state as one in which all water vapor has condensed out, then

$$T_{oo} = T \left(\frac{p_{oo}}{p} \right)^k \exp \frac{L_v r_v}{C_p T} = \theta_E \quad (\text{A6})$$

where θ_E is the equivalent potential temperature.

Alternatively we could have defined the reference state T_{oo} as the wet bulb temperature at $p=p_{oo}$ to obtain a definition of the pseudo-wet bulb potential temperature θ_w

$$T_{oo} = T \left(\frac{p_{oo}}{p} \right)^K \exp \frac{L_v}{c_p} \left[\frac{r_v}{T} - \frac{r_{v_o}}{T_{w_o}} \right] = \theta_w \quad (A7)$$

where T_{w_o} and r_{v_o} are the wet bulb temperature and saturation mixing ratio at p_{oo} . Eq. (A6) is strictly true for a saturated process. For an unsaturated process we would write formally

$$\theta_E = \theta \exp \frac{L_v r_v}{c_p T_c} \quad (A8)$$

where T_c is the temperature at the level at which condensation first occurs. We seek a thermodynamic variable which is approximately conserved in both the saturated and unsaturated regimes, and this would eliminate the need to calculate the temperature of the condensation level at each time step. If we write

$$\theta_E = \theta \exp \frac{L_v r_v}{c_p T_o} \quad (A9)$$

where T_o is a constant, then the error in θ_E will be $-L_v r_v \theta_E (T-T_o)/c_p T_o^2$. For $(T-T_o)=5^\circ$, $\theta_E=273$, $r_v=.003$, the error in θ_E will be about 0.14° , which is quite acceptable for our purposes.

The saturation vapor pressure r_s is computed from the definition of equivalent potential temperature and the Clausius-Clapeyron equations,

$$e_s(T) = e_{s_o} \exp \frac{L_v}{R_v} \left[\frac{1}{T_o} - \frac{1}{T} \right] \quad (A10)$$

$$\theta_E = T \left(\frac{p_{oo}}{p} \right)^K \exp \frac{L_v r_v}{c_p T_o} \quad (A11)$$

and
$$r_s = 0.622 e_s / (p - e_s) \quad (A12)$$

Here e_{s_0} is the saturation vapor pressure at some temperature T_0 . Equations (A10)-(A12) are solved numerically in advance to yield unique values of r_s and T given θ_E and p .

APPENDIX B: EXTINCTION PARAMETERS

The absorption efficiency Q_a and extinction efficiency Q_e are computed from an approximation to the exact Mie theory for large spherical particles as $|N \rightarrow 1|$ which is discussed by Van de Hulst (1957, Ch.11). We let N_r denote the real part of the index of refraction N , and N_i the imaginary part; a is the particle radius and λ is the wavelength. With $\chi = 2\pi a/\lambda$ and $\rho = 2\chi(N_r - 1)$ we have

$$Q_e = 2 - 4 \exp(-\rho \tan \beta) \frac{\cos \beta}{\rho} \sin(\rho - \beta) - 4 \exp(-\rho \tan \beta) \left(\frac{\cos \beta}{\rho}\right)^2 \cos(\rho - 2\beta) + 4 \left(\frac{\cos \beta}{\rho}\right) \cos 2\beta \quad (B1)$$

$$Q_a = 2 K(2 \rho \tan \beta) \quad (B2)$$

where $\tan \beta = N_i/(N_r - 1)$ and the function $K(y)$ is

$$K(y) = \frac{1}{2} + e^{-y}/y + (e^{-y} - 1)/y^2 \quad (B3)$$

Q_e and Q_a are plotted as a function of λ for several particle sizes in Figs. B1 and B2, along with the Planckian weighting function, B_λ . The indices of refraction were taken from the compilation of Irvine and Pollack (1968). In the near infrared $N_r \sim 1.3$ and $N_i \ll 1$ and we would expect B1 and B2 to give only fair agreement with the exact Mie theory. However, the location of important maxima and minima should be well represented,

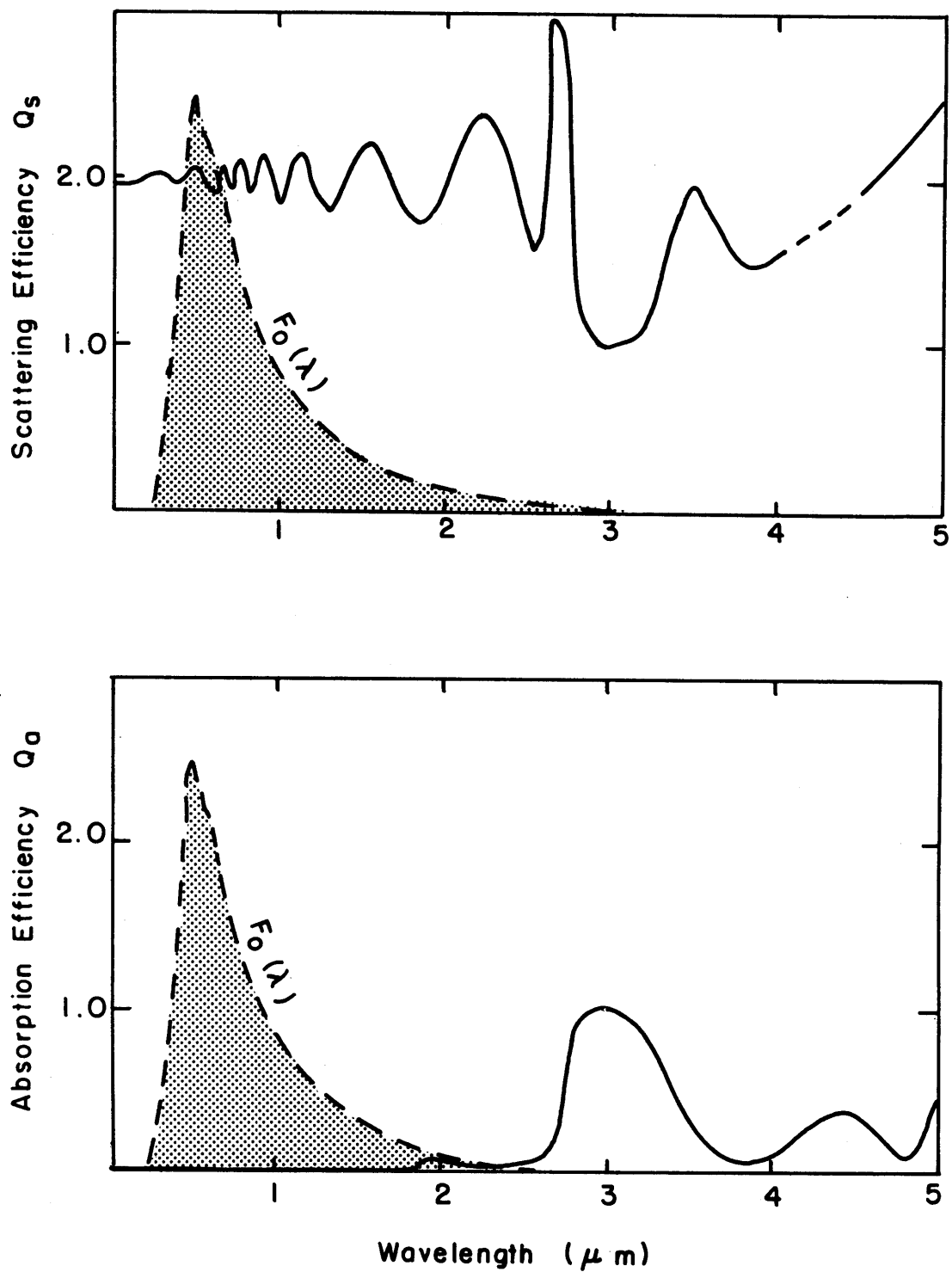


Fig. B1 Extinction parameters and blackbody curve (6000 K) for solar spectrum.

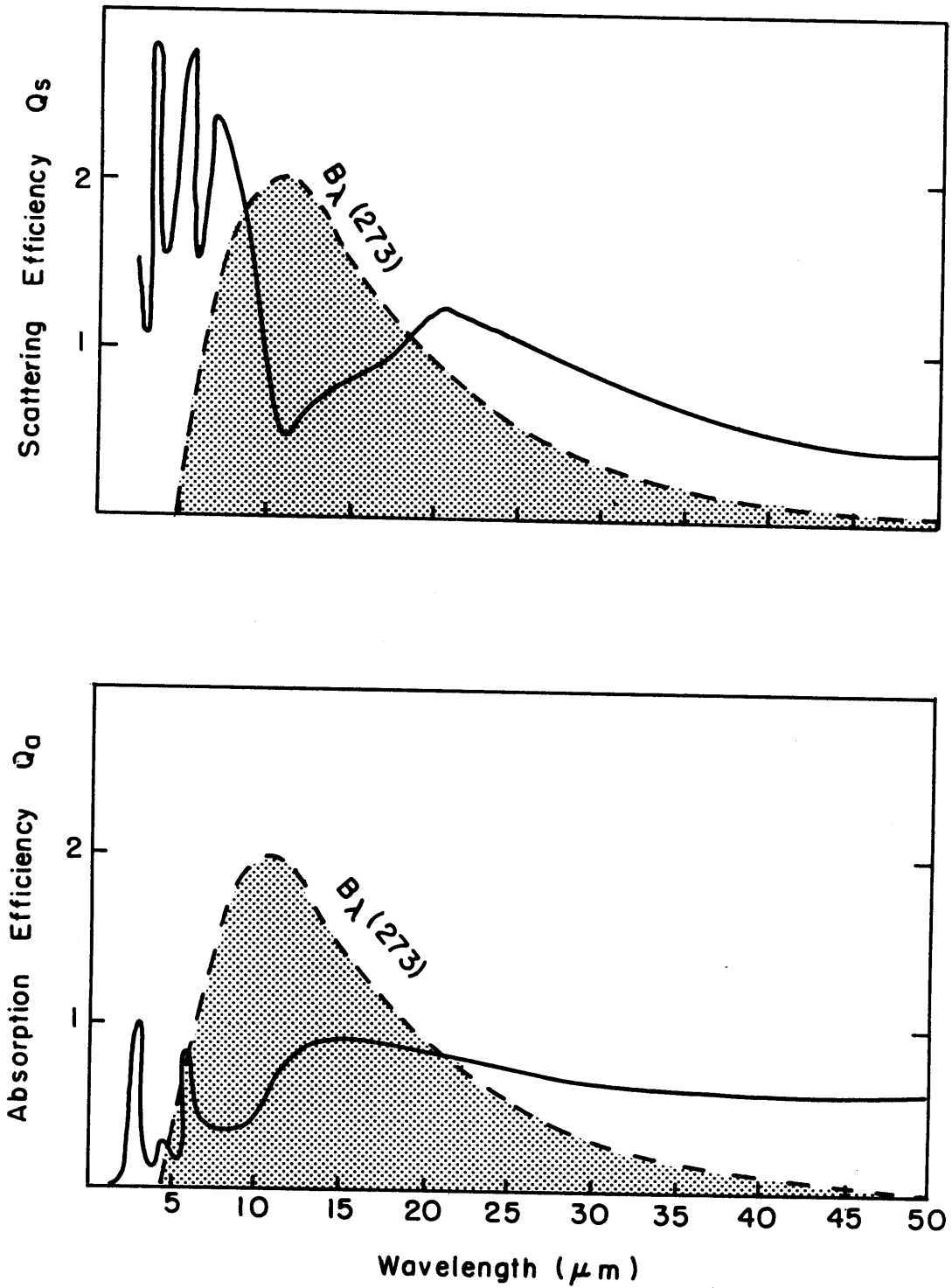


Fig. B2 Extinction parameters are blackbody curve in infrared spectrum.

and our crude representation of the drop-size distribution does not warrant a more detailed treatment.

APPENDIX C: THE FINITE DIFFERENCE MODEL

C1. Time Marching Equations

The system (2.2.6)-(2.2.9) is solved as a time marching problem in the domain $t=0$ to $t=t^*$ and $z=0$ to $z=2050$ m. With $t=n\Delta t$ and $z=(k-1)\Delta z$, the finite difference equivalents of (2.2.7)-(2.2.10) are

$$\begin{aligned} \theta_E^{k,n+1} = & \theta_E^k + \Delta t \left[\frac{1}{\Delta z^2} (K^{k+1,n} (\theta_E^{k+1,n} - \theta_E^{k,n}) - K^{k,n} (\theta_E^{k,n} - \theta_E^{k-1,n})) \right. \\ & \left. - \frac{1}{4\Delta z} (\omega^{k+1} + \omega^k) (\theta_E^{k+1,n} - \theta_E^{k-1,n}) \right] \end{aligned} \quad (C1)$$

$$\begin{aligned} r^{k,n+1} = & r^{k,n} + \Delta t \left[\frac{1}{\Delta z^2} (K^{k+1,n} (r^{k+1,n} - r^{k,n}) - K^{k,n} (r^{k,n} - r^{k-1,n})) \right. \\ & \left. - \frac{1}{2\Delta z} \omega_f (r_l^{k+1} - r_l^{k-1}) \right. \\ & \left. + \pi \frac{kQ}{c_p} \left(1 + \frac{L}{c_p T_0} r_v^{k,n} + \frac{1}{2} \left(\frac{L}{c_p T_0} \right)^2 (r_v^{k,n})^2 \right) \right] \end{aligned} \quad (C2)$$

$$\begin{aligned} u^{k,n+1} = & u^{k,n} + \Delta t \left[\frac{1}{\Delta z^2} (K^{k+1,n} (u^{k+1,n} - u^{k,n}) - K^{k,n} (u^{k,n} - u^{k-1,n})) \right. \\ & \left. + f_v^{k,n} \right] \end{aligned} \quad (C3)$$

$$\begin{aligned} v^{k,n+1} = & v^{k,n} + \Delta t \left[\frac{1}{\Delta z^2} (K^{k+1,n} (v^{k+1,n} - v^{k,n}) - K^{k,n} (v^{k,n} - v^{k-1,n})) \right. \\ & \left. - f_u^{k,n} \right] \end{aligned} \quad (C4)$$

These were solved on a one-dimensional staggered grid illustrated in Fig. C1. The surface layer was assumed to extend to $z=25$ m, while the Ekman region extended from 25 m to 2050 m.

wide range of θ_E and p . During the integration r_s was simply obtained from that table by interpolation, which eliminated the need to solve the non-linear system (A10)-(A12) at each time-step. Similarly a table of C_u and C_θ was computed for a range of values of Ri_B in subroutine OBUKHOV. SURFACE calculated the surface fluxes U_*^2 , $U_*\theta_{v*}$ and U_*r_{v*} from the initial (or current) values of ΔU , $\Delta\theta_v$ and Δr_v , and EDDY computed the diffusion coefficient from one of the forms (3.1.40)-(3.1.42).

The gaseous and liquid absorber amounts are determined in QRAD, which calls SOLAR to compute the solar flux and FLUX which computes the thermal flux. The heating rate is computed as the divergence of the net flux in QRAD.

The fields of θ_E , r , u , and v are computed in DIFFEQN and the liquid water content is calculated as $r-r_s$ in WATER. The surface fluxes, diffusion coefficients and radiative parameters are calculated from the current values of the dependent variables in (2.6)-(2.9), and the integration is continued.

All models were run with $\Delta z=50$ m and $\Delta t=10$ min. Most calculations were done over $n=1000$ time-steps, corresponding to an integration period of 6.94 days.

Figure C1.

One-Dimensional Grid Used in Model

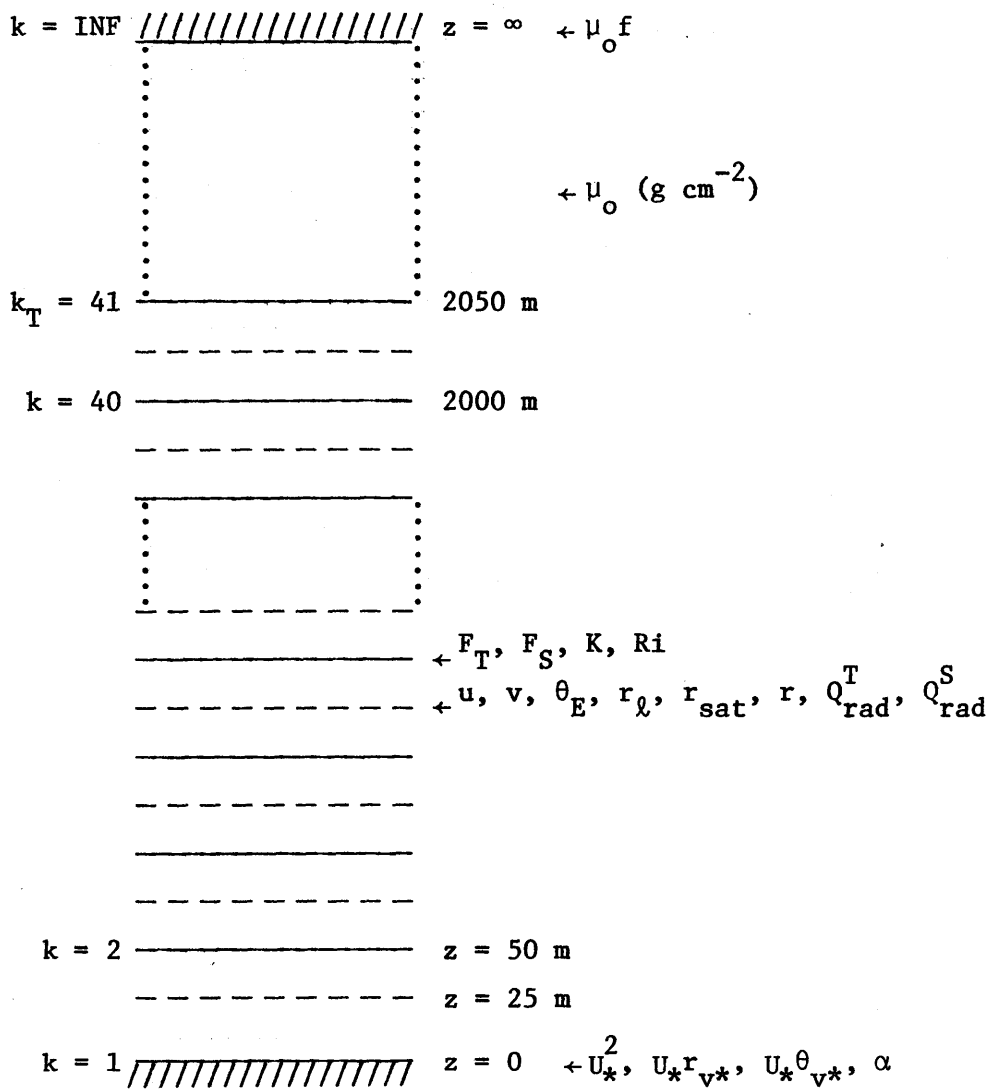
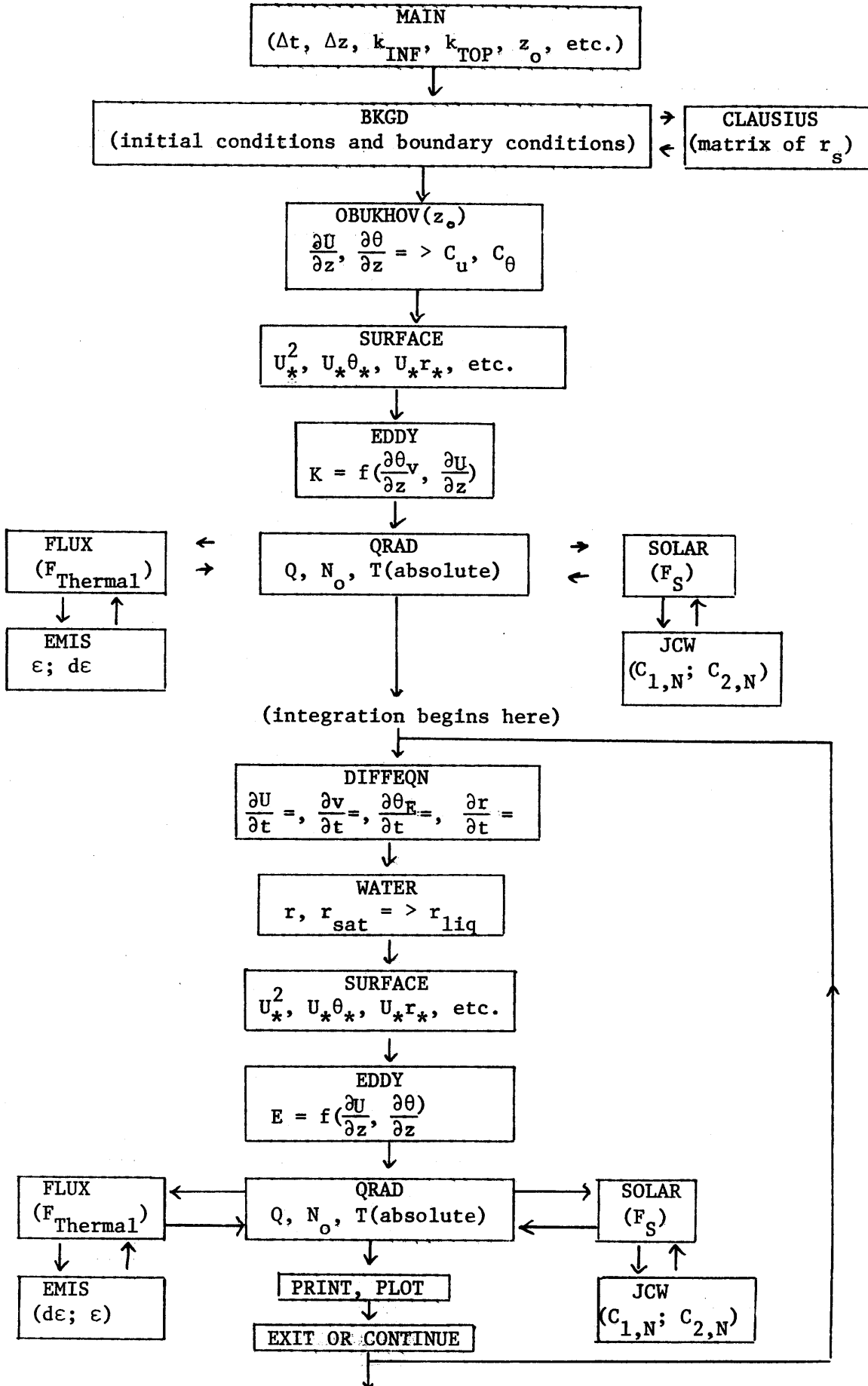


Figure C2



LIST OF SYMBOLS

Symbol	Defined or first used	Definition
a	4.1.2	Thermodynamic constant
a	3.2.2	Droplet radius
a_i	3.2.2	Weighting coefficient
a_j	3.2.1	Weighting coefficients in Gaussian integration
a_0	4.1.3	Constant of integration
A	4.1.2	Constant of proportionality for vertical velocity
A_0	4.1.6	Constant for radiative lifting
\mathbf{A}	3.2.2	Matrix used in calculating solar flux
b	4.1.2	Thermodynamic constant
B'_ν	3.2.1	Source function at frequency ν
B_ν	3.2.2	Planck function at frequency ν
B_d	4.1.6	Black-body intensity corresponding to dew point temperature
B^*		Black-body intensity at $\tau_T = \tau_T^*$
C_θ	3.1.1	Heat transfer coefficient
C_u	3.1.1	Momentum transfer coefficient
C_p	2.2.2	Specific heat of dry air
$C_{1,N}$	3.2.2	Constants for N^{th} homogeneous layer
$C_{2,N}$		
\mathbf{C}	3.2.2	Matrix of constants
D	4.1.2	Vertical scale
e_s	4.1.2	Saturation vapor pressure
f	2.2.2	Coriolis parameter
$f(\nu)$	3.2.2	Solar irradiation at frequency ν
F	3.2.2	Flux
F_S	3.2.2	Flux in solar spectrum
F_T	3.2.3	Flux in longwave region of spectrum
F_S^{Net}	3.2.2	Flux integrated over NIR spectrum
F_T^{Net}	3.2.3	Flux integrated over longwave spectrum

F_B^+	3.2.2	Upward flux at base and top of cloud
F_T^+		
F_B^-	3.2.2	Downward flux at base and top of cloud
F_T^-		
\mathbb{F}	3.2.2	Vector used in solar calculations
g	3.1.1	Gravitational acceleration
G	4.1.6	Constant in radiative lifting calculations
H	3.2.2	Hour angle
I	3.2.1	Specific intensity
I^+	3.2.1	Intensities in the first approximation
I^-		
$I^{(o)}$	3.2.1	Axially symmetric part of the intensity
I_h	3.1.1	Integral of universal function for heat
I_m	3.1.1	Integral of universal function for momentum
K	3.1.3	Eddy diffusivity
k_o	3.1.1	Von Karman's constant
k_i	3.2.2	Absorption coefficient for i^{th} interval
k_g	3.2.1	Gaseous volume absorption coefficient
k'_g	3.3.2	Gaseous mass absorption coefficient
k_c	3.2.1	Cloud volume absorption coefficient
l	3.1.2	Dominant eddy size
L	3.1.1	Obukhov length
L_V	3.1.1	Latent heat of vaporization of water
m	3.3.2	Aerosol absorber amount
M	3.2.2	Index for fit of transmission data
M	3.2.2	Magnification factor
N	3.2.1	Maximum order of Legendre polynomial
N	3.2.2	Number of homogeneous regions in solar calculations
N_o	3.2.2	Droplet density (cm^{-3})

$N_o X_a^S$	3.2.2	Parameter (= $N_o \pi a^2 \overline{Q_a^S}$)
$N_o X_a^T$	3.2.3	Parameter (= $N_o \pi a^2 \overline{Q_a^T}$)
p	3.2.1	Phase function
p	3.2.2	Pressure
p_o	3.2.2	Surface pressure
P_ℓ^m	3.2.1	Associated Legendre polynomials
q	3.1.2	Velocity scale
Q_e	3.2.2	Extinction efficiency
Q_s	3.2.2	Scattering efficiency
Q_a	3.2.2	Absorption efficiency
Q_{rad}	2.2.2	Volume rate of radiative heating
Q_{rad}^S	3.2.2	Heating rate in NIR
Q_{rad}^T	4.1.2	Heating rate in longwave spectrum
$\overline{Q_s^S}$	3.2.2	Planck mean scattering efficiency in NIR
$\overline{Q_a^S}$	3.2.2	Planck mean absorption efficiency in NIR
$\overline{Q_s^T}$	3.2.3	Planck mean scattering efficiency in longwave
$\overline{Q_a^T}$	3.2.3	Planck mean absorption efficiency in longwave
r	2.2.2	Total water mixing ratio (g/g)
r_ℓ	2.2.2	Liquid water mixing ratio (g/g)
r_s	4.1.2	Saturation mixing ratio
r_v	2.2.2	Water vapor mixing ratio
r_*	3.1.1	Characteristic water vapor mixing ratio
Ri_B	3.1.1	Bulk Richardson number for surface layer
R_f	3.1.1	Flux Richardson number
R_c	3.2.2	Cloud reflectivity

R_v	4.1.2	Gas constant for water vapor
R	4.3	Integrated liquid water
s	3.2.1	Volume scattering coefficient
t	2.2.2	Time
t^*	2.2.2	Maximum integration time of model
$\left. \begin{array}{l} T \\ T_d \end{array} \right\}$	4.1.3	$\left\{ \begin{array}{l} \text{Temperature} \\ \text{Dew point temperature} \end{array} \right.$
$\overline{T_{\Delta\nu}}$	3.2.2	Mean transmissivity for frequency $\Delta\nu$
T_c	3.2.2	Cloud transmissivity
u	2.2.2	Departure from geostrophic wind, U_o
u	3.3.2	Gaseous absorber amount
u^*	4.1.6	Gaseous absorber amount
u_a	4.1.2	Anemometer level wind
u_o	3.2.2	Water vapor path length above boundary layer
u'_o	3.2.2	Corrected water vapor path length
u_{∞}^*	3.1.2	Gaseous absorber amount to infinity
u_u^*	3.1.2	Gaseous absorber amount to surface
U_*	3.1.1	Friction velocity
U_o	2.2.2	Basic current in x-direction
U	3.1.1	Resultant wind velocity
w_f	2.2.2	Fall velocity of water drops
w	4.1.1	Mean vertical velocity
$\overline{(w'r'_v)}$	3.1.1	Turbulent flux of water vapor
$\overline{(w'r')}$	2.2.2	Turbulent transport of total water
$\overline{(w'U')}$	3.1.1	Turbulent flux of momentum
$\overline{(w'\theta')}_o$	3.1.1	Turbulent flux of potential temperature at surface
$\overline{(w'\theta'_v)}_o$	3.1.1	Turbulent flux of virtual potential temperature at surface
$\overline{(u'w')}$	2.2.2	Turbulent transport of x-momentum

$(\overline{v'w'})$	2.2.2	Turbulent transport of y-momentum
$(\overline{w'\theta'})$	3.1.1	Turbulent flux of potential temperature
$(\overline{w'\theta'_E})$	2.2.2	Turbulent transport of equivalent potential temperature
$\left. \begin{array}{l} x \\ y \end{array} \right\}$	3.1.1	Dummy variables in similarity equations
z	2.2.2	Vertical coordinate
z_T	4.1.1	Upper boundary of model
z_o	3.1.1	Surface roughness
α	3.1.3	Constant in eddy diffusivity formulation
α	3.2.2	Surface reflectivity
β	3.2.1	Scattering parameter
$\overline{\beta}$	3.2.2	Mean scattering parameter
β^N	3.2.2	Scattering parameter in N^{th} homogeneous layer
γ	3.2.1	Parameter in radiation calculations
γ	4.1.3	Greenhouse factor
Δ	4.1.3	Constant in radiative equilibrium calculations
$\delta_{o,m}$	3.2.1	Kronecker delta
δ	3.2.2	Declination of sun
$\delta/\delta t$	2.2.2	Downstream derivative
Δt	3.1.3	Time step
ϵ	3.1.2	Energy dissipation rate
ϵ'	3.1.2	Derivative of emissivity
ϵ_c	3.2.3	Cloud emissivity
ϵ_g	3.2.3	Gaseous emissivity
ϵ_M	3.2.3	Mixed emissivity
θ	3.2.1	Zenith angle
θ_E	2.2.2	Equivalent potential temperature
θ_v	3.1.1	Virtual potential temperature
θ_{v^*}	3.1.1	Characteristic virtual potential temperature
θ_w	Appendix A	Wet-bulb potential temperature

θ_{v_0}	3.1.1	Virtual potential temperature at surface
θ_*	3.1.1	Characteristic potential temperature
κ	4.1.2	Constant (R/C_p)
λ	3.2.1	Wavelength
λ	3.2.2	Latitude
μ_0	3.2.2	Cosine of solar zenith angle
μ	3.2.1	Cosine of zenith angle
μ_i	3.2.1	Cosine of zenith angle in the i^{th} direction
ν	3.2.1	Frequency
ω	3.2.1	Single scattering albedo
ω_λ	3.2.1	Constants
ρ	2.2.2	Density of air
ρ_w	3.2.2	Density of water vapor
ρ_0	3.1.1	Density of air at surface
σ	3.1.2	Stefan-Boltzmann constant
τ	3.1.1	Surface stress
τ	3.1.2	Eddy lifetime
$\tau_{\text{rad}}^{\text{bound}}$	3.1.2	Radiative relaxation time for exchange with boundary
$\tau_{\text{rad}}^{\text{space}}$	3.1.2	Radiative relaxation time for cooling to space
τ_c	4.1.2	Condensative time scale
τ'	3.2.1	Extinction optical depth
τ	3.2.1	Absorption optical depth
τ_S^N	3.2.2	Absorption optical depth in N^{th} layer
τ_S	3.2.2	Absorption optical depth in solar region
τ_S^*	3.2.2	Total solar optical depth
τ_T	3.2.3	Absorption optical depth in longwave spectrum
τ_T^*	3.2.3	Total absorption optical depth in longwave spectrum
ϕ_h	3.1.1	Universal function for heat
ϕ_m	3.1.1	Universal function for momentum

ϕ_r	3.1.1	Universal function for moisture
ϕ	3.2.1	Azimuth
$\left. \begin{array}{l} \psi_1 \\ \psi_2 \end{array} \right\}$	3.1.1	Dummy variables in similarity equations
$\langle \cos\theta \rangle$	3.2.1	Asymmetry factor
\bar{t}	4.1.6	Integration time
$\left. \begin{array}{l} \overline{J_c} \\ \overline{J_g} \end{array} \right\}$	3.2.3	Frequency averaged cloud and gaseous transmissivities
J_c	3.2.3	Gaseous transmissivity
J_g	3.2.3	Cloud transmissivity

REFERENCES

- Arking, A. and K. Grossman (1972), "The Influence of Line Shape and Band Structure on Temperatures in Planetary Atmospheres", J. Atmos. Sci., 29, 937-949.
- Asai, T. (1965), "A Numerical Study of the Air Mass Transformation over the Japan Sea in Winter", J. Met. Soc. Japan, Ser. II, 43, 1-15.
- Badgley, F. (1961), "Heat Balance at the Surface of the Arctic Ocean", Proc. Western Snow Conf., Spokane, 101-104.
- Ball, F.K. (1960), "Control of Inversion Height by Surface Heating", Quart. J. R. Met. Soc., 86, 483-494.
- Belmont, A.D. (1958), "A Brief Review of Research in Arctic Meteorology", in: Polar Atmosphere Symposium (R. Sutcliffe, ed.), New York: Pergamon Press, 341 pp.
- Belmont, A.D. (1958), "Lower Tropospheric Inversions at Ice Island T-3", in Polar Atmosphere Symposium (R.C. Sutcliffe, ed.), New York: Pergamon Press, 341 pp.
- Bergeron, T. (1928), "Über die dreidimensional verknüpfende Wetteranalyse", Geophys. Publikasjoner, 5, 1-111.
- Berry, F.A., G.V. Owens, and H.P. Wilson (no date), Arctic Weather Maps, U.S. Navy, BUAER Proj. TED-UNL-MA-501.
- Blackadar, A.K. (1962), "The Vertical Distribution of Wind and Turbulent Exchange in a Neutral Atmosphere", J. Geophys. Res., 67, 3095-3102.
- Brooks, D.L. (1950), "A Tabular Method for the Computation of Temperature Change by Infrared Radiation in the Free Atmosphere", J. Met., 7, 313-321.
- Brutsaert, W. (1972), "Radiation, Evaporation, and the Maintenance of Turbulence under Stable Conditions in the Lower Atmosphere", Boundary Layer Meteorology, 2, 309-325.
- Burch, D.E., E.B. Singleton, W.L. France, and D. Williams (1960), "Infrared Absorption by Minor Atmospheric Constituents", Report on RF project 778, Ohio State Univ.
- Burke, C.J. (1945), "Transformation of Polar Continental Air to Polar Maritime Air", J. Met., 2, 94-112.
- Businger, J.A. (1973), "Turbulent Transfer in the Atmospheric Surface Layer", in Workshop on Micrometeorology, D. Haugen (ed.), Boston: American Met. Soc., 392 pp.
- Businger, J.A. and S.P.S. Arga (1974), "Height of the Mixed Layer in the Stably Stratified Planetary Boundary Layer", in: Advances in Geophysics, Vol. 18A (H. Landsberg, ed.), 462 pp.

- Chandrasekhar, S. (1960), Radiative Transfer, New York: Dover Publications, 393 pp.
- Chernigovskii, N.T. (1963), "Radiational Properties of the Central Arctic Ice Coat", Trudy AANII, 253, 249-260 (Eng. Trans. Rand Mem. RM-5003-PR, 1966).
- Cowling, T.G. (1950), "Atmospheric Absorption of Heat Radiation by Water Vapor", Philosophical Mag., 41, 109-123.
- Deardorff, J.W. (1967), "Empirical Dependence of the Eddy Coefficient for Heat upon Stability above the Lowest 50 m", J. Appl. Met., 6, 631-643.
- Deardorff, J.W. (1972), "Parameterization of the Planetary Boundary Layer for Use in General Circulation Models", Monthly Weather Rev., 100, 93-106.
- Dergach, A.L., G. M. Zabrodsky, and V.G. Morachevsky (1960), "The Results of a Complex Investigation of the Type St-Sc Clouds and Fogs in the Arctic", Bulletin (Izvestiya) Acad. Sci. USSR Geophys. Ser., 1, 66-70.
- Dolgin, I.M. (1960), "Arctic aero-climatological studies", Probl. Arktiki, 4, 64-75 (in Russian).
- Dopplick, T. G. (1972), "Radiative Heating of the Global Atmosphere", J. Atmos. Sci., 29, 1278-1294.
- Doronin, Yu. P. (1969), Thermal Interaction of the Atmosphere and the Hydrosphere in the Arctic. Leningrad: Gidrometeorologicheskoe Izd. (English translation by Israel Prog. for Scientific Translation, 1966).
- Dyer, A.J. (1967), "The Turbulent Transport of Heat and Water Vapor in an Unstable Atmosphere", Quart. J. R. Met. Soc., 93, 501-508.
- Dziedzhevskii, B.L. (1945) "The Circulation of the Atmosphere in the Central Polar Basin", Tr. Dreifuiushchei Stantsii "Svernyi Polius", 2, 64-200 (English translation, UCLA Meteorology Dept. Rept.#6, 1954).
- Elasser, W.M. (1942), "Heat Transfer by Infrared Radiation in the Atmosphere", Harvard Meteorological Studies, No.6, Harvard Univ. Press.
- Estoque, M.A. (1963), "Numerical Modelling of the Planetary Layer", in Workshop on Micrometeorology, D. Haugen (ed.), Boston: American Met. Soc., 392 pp.
- Feigel'son, E.M. (1964), Light and Heat Radiation in Stratus Clouds, Izd. "Nauka", 245 pp. (English translation by Israel Prog. for Scientific Translation, 1966).
- Feigel'son, E.M. (1970), Radiant Heat Transfer in a Cloudy Atmosphere. Leningrad: Gidrometeorologicheskoe Izd., 191 pp. (English translation by Israel Prog. for Scientific Translation, 1973).
- Fletcher, J.O. (1965), "The Heat Budget of the Arctic Basin and Its Relation to Climate", RAND Report R-444-PR, 179 pp.

- Fritz, S. (1958), "Absorption and Scattering of Solar Energy in Clouds of 'Large Water Drops'-II", J. Met., 15, 51-58.
- Gathman, S.G. and R.E. Larson (1974), "Marine Fog Observations in the Arctic", Naval Research Laboratory, Report 7693, 24 pp.
- Gavrilova, M.K. (1963), Radiation Climate of the Arctic. Leningrad: Gidrometeorologichskoe Izd., 178 pp. (English translation by Israel Prog. for Scientific Translation, 1966).
- Gierasch, P. and R. Goody (1970), "Models of the Venus Clouds", J. Atmos. Sci., 27, 224-245.
- Goody, R.M. (1956), "The Influence of Radiative Transfer on Cellular Convection", J. Fl. Mech., 1, 424-435.
- Goody, R.M. (1964), Atmospheric Radiation, Oxford: Clarendon Press, 436 pp.
- Griggs, M. (1968), "Aircraft Measurements of Albedo and Absorption of Stratus Clouds, and Surface Albedos", J. Appl. Met., 7, 1012-1017.
- Hare, F.K. and S. Orvig (1958), "The Arctic Circulation", McGill Univ. Arctic Res. Group, Pub. in Meteorology, No.12, 211 pp.
- Hildebrand, F.B. (1962), Advanced Calculus for Applications, Englewood Cliffs, N.J.: Prentice Hall, 646 pp.
- Huschke, R.E. (1969), "Arctic Cloud Statistics from Air Calibrated Surface Weather Observations", RAND Memorandum RM-6173-PR, 79 pp.
- Irvine, W.M. and J.B. Pollack (1968), "Infrared Optical Properties of Water and Ice Spheres", Icarus, 8, 324-360.
- Jayaweera, K.O.L.F. and T. Ohtake (1973), "Concentration of Ice Crystals in Arctic Stratus Clouds", J. Res. Atm., 7, 199-207.
- Knollenberg, R.G. (1972), "On Radiational Cooling Computations in Clouds", J. Atmos. Sci., 29, 212-214.
- Kondrat'yev, K. Ya. (1965), Radiative Heat Exchange in the Atmosphere, New York: Pergamon Press, 411 pp.
- Koptev, A.P. and A.I. Voskresenskii (1962), "On the Radiation Properties of Clouds", Proc. Arctic and Antarctic Res. Inst., 239(2), 39-47 (Translated by Rand Corp., Memo RM-5003-PR, 1966).
- Kumai, M. (1973), "Arctic Fog Droplet Size Distribution and Its Effects on Light Attenuation", J. Atmos. Sci., 30, 635-643.
- Lacis, A.A. and J.E. Hansen (1974), "A Parameterization for the Absorption of Solar Radiation in the Earth's Atmosphere", J. Atmos. Sci., 31, 118-133.
- LeBlanc, L.L. and K.C. Brundidge (1969), "A Numerical Experiment in Predicting Stratus Clouds", J. Appl. Met., 8(2), 177-189.

- Levenberg, K. (1944), "A Method for the Solution of Certain Non-linear Problems in Least Squares", Quart. Appl. Math., 2, 164-168.
- Lilly, D.K. (1968), "Models of Cloud-Topped Mixed Layers under a Strong Inversion", Quart. J. R. Met. Soc., 94, 292-309.
- Lockhart, W.M. (1943), "A Winter Fog in the Interior", in: Characteristic Weather Phenomena of California (H. Byers, ed.), MIT Meteorological Papers, Vol.I, No.2, 54 pp.
- Manabe, S. and R.F. Strickler (1964), "On the Thermal Equilibrium of the Atmosphere with a Convective Adjustment", J. Atmos. Sci., 21(4), 361-385.
- Markosova, L.I. and V.I. Shlyakhov (1972), "Problem of Radiation Properties of Clouds in the Upper and Middle Levels and with Vertical Development", Meteorologiya i Gidrologiya, 5, 89-93.
- Marshunova, M.S. (1961), "Principal Characteristics of the Radiation Balance of the Underlying Surface and of the Atmosphere in the Arctic", Trudy AANII, 229, 5-53 (English translation, Rand memorandum RM-5003-PR, 1966)
- Mason, B.J. (1957), The Physics of Clouds, Oxford: The Clarendon Press, 481 pp.
- Matveev, L.T. (1964), "On the Formation and Development of Layer Clouds", Tellus, 16, 139-146.
- Monin, A.S. and A.M. Obukhov (1954), "Basic Regularity in Turbulent Mixing in the Surface Layer of the Atmosphere", USSR Acad. Sci., Geophys. Inst., No.24.
- Neiburger, M. (1944), "Temperature Changes during Formation and Dissipation of West Coast Stratus", J. Met., 1, 29-41.
- Neiburger, M. (1949), "Reflection, Absorption, and Transmission of Insolation by Stratus Cloud", J. Met., 6, 98-104.
- Newell, R.E., J.W. Kidson, D.G. Vincent, and G.J. Boer (1972), The General Circulation of the Tropical Atmosphere and Interactions with Extratropical Latitudes, Cambridge: MIT Press, 258 pp.
- Newell, R.E., J.W. Kidson, D.G. Vincent, and G.J. Boer (1974), The General Circulation of the Tropical Atmosphere and Interactions with Extratropical Latitudes, Vol.II, Cambridge: MIT Press, 371 pp.
- Oort, A.H. (1974), "Year-to-Year Variations in the Energy Balance of the Arctic Atmosphere", J. Geophys Res., 79(9), 1253-1260.
- Oort, A.H. and E.M. Rasmussen (1971), "Atmospheric Circulation Statistics", U.S. Dept. Commerce, NOAA Prof. Paper #5, 323 pp.
- Paltridge, G.W. (1974), "Atmospheric Radiation and the Gross Character of Stratiform Cloud", J. Atmos. Sci., 31, 244-250.

- Paltridge, G.W. (1974), "Infrared Emissivity, Short-Wave Albedo, and the Microphysics of Stratiform Water Clouds", J. Geophys. Res., 79, 4053-4058.
- Paulson, C.A. (1970), "The Mathematical Representation of Wind Speed and Temperature Profiles in the Unstable Atmospheric Surface Layer", J. Appl. Met., 9, 857-861.
- Petterssen, S. (1956), Weather Analysis and Forecasting, Vol.II, New York: McGraw-Hill, 260 pp.
- Pilie, R.J., E.J. Mack, W.C. Kocmond, C.W. Rogers and W.J. Eadie (1975), "The Life Cycle of Valley Fog, Parts I and II", J. Appl Met., 14, 347-374.
- Poage, W.C. (1954), "The Dropsonde Record from Alaska to the North Pole", UCLA Scientific Report No.2, 52 pp.
- Priestley, C.H.B. (1959), Turbulent Transfer in the Lower Atmosphere, Chicago: University of Chicago Press, 130 pp.
- Prik, Z.M. (1959), "Mean Position of Surface Pressure in the Arctic", Trudy AANII, 217, 5-34 (In Russian).
- Reed, R.J. (1959), "Arctic Weather Analysis and Forecasting", Univ. of Washington Occasional Rept. No.11, 119 pp.
- Reed, R.J. and B.A. Kunkel (1960), "The Arctic Circulation in Summer", J. Met., 17, 489-514.
- Reed, R.J. and R. K. Surface (1959), "Arctic Weather Studies: Summer Season", Dept. Met. and Climatology, Sci. Rept. #5, U. Washington, 48 pp.
- Robinson, G.D. (1950), "Two Notes on Temperature Changes in the Troposphere due to Radiation", Cent. Proc. R. Met. Soc., 26-29.
- Rodgers, C.D. (1967), "The Radiative Heat Budget of the Troposphere and Lower Stratosphere", MIT Dept. of Meteorology Report A2, Planetary Circulations Project, 99 pp.
- Rodgers, C.D. (1967a), "The Use of Emissivity in Atmospheric Radiation Calculations", Quart. J. R. Met., Soc., 93, 43-54.
- Sagan, C. and J.B. Pollack (1967), "Anisotropic Nonconservative Scattering and the Clouds of Venus", J. Geophys. Res., 72, 469-477.
- Shir, C.C. (1972), "A Numerical Computation of Air Flow over a Sudden Change of Surface Roughness", J. Atmos. Sci., 29, 304-310.
- Smith, S.D. E.G. Banke, and O.M. Johannessen (1970), "Wind Stress and Turbulence over Ice in the Gulf of St. Laurence", J. Geophys. Res., 75, 2803-2812.
- Sverdrup, H.U. (1933), The Norwegian North Polar Expedition with the "Maud", 1918-1925, Scientific Results, Vol.II, Bergen: Griegs Boktrykkeri, 527 pp.

- Taylor, G.I. (1935), "Statistical Theory of Turbulence", Proc. Roy. Soc. Lond. A, 151, 421-478.
- Taylor, P.A. (1971), "Airflow above Changes in Surface Heat Flux, Temperature and Roughness, and Extension to Include the Stable Case", Boundary Layer Met., 1, 474-497.
- Townsend, A.A. (1958), "The Effects of Radiative Transfer on Turbulent Flow of a Stratified Fluid", J. Fluid Mech., 4, 361-375.
- Townsend, A.A. (1964), "Natural Convection in Water over an Ice Surface", Quart. J. R. Met. Soc., 90, 248-259.
- U.S. Navy Hydrographic Office (1958), Oceanographic Atlas of the Polar Seas, 2: Arctic, Washington: U.S. Navy Hydrographic Office Publ. 705, 149 pp.
- Untersteiner, N. and F.I. Badgley (1965), "The Roughness Parameters of Sea Ice", J. Geophys. Res., 70, 4573-4577.
- Untersteiner, N. (1961), "On the Mass and Heat Budget of Arctic Sea Ice", Arch. Meteorol. Geophys. Bioklimatol., A, 12, 151-182.
- Untersteiner, N. (1964), "Calculations of Temperature Regime and Heat Budget of Sea Ice in the Central Arctic", J. Geophys. Res., 69, 4755-4766.
- van de Hulst, H.C. (1957), Light Scattering by Small Particles, New York, Wiley.
- von Bezold, W. (1888), "On the Thermodynamics of the Atmosphere", Sitz. der Konig Preuss Akademie der Wissenschaften zu Berlin, 485-522 (Trans. in Abbe: The Mechanics of the Earth's Atmosphere, 1910).
- Vowinckel, E. and S. Orvig (1970), "The Climate of the North Polar Basin", in World Survey of Climatology Vol.14, Climates of the Polar Regions, S. Orvig (ed.), New York: Elsevier, 370 pp.
- Vowinckel, E. and S. Orvig (1967), "The Inversion over the Polar Ocean", in Polar Meteorology, WMO Technical Note No.87 (WMO-No.211.TP.111), 39-59.
- Vowinckel, E. and B. Taylor (1965), "Energy Balance of the Arctic. IV. Evaporation and Sensible Heat Flux over the Arctic Ocean", Arch. Meteorol. Geophys. Bioklimatol., 14, 36-52.
- Walsh, J.E. (1974), "Sea Breeze Theory and Applications", J. Atmos. Sci., 31, 2012-2026.
- Weller, G., S.A. Bowling, B. Holmgren, K.O.L.F. Jayaweera, T. Ohtake and G. Shaw (1975), "The Radiation Matrix in the Arctic", Proc. Conf. on Climate of the Arctic, Fairbanks, 1973 (ed: G. Weller).
- Willett, H.C. and F. Sanders (1959), Descriptive Meteorology, New York: Academic Press, 355 pp.
- Wilson, H.P. (1963), "Notes on Arctic Weather", In Proc. Arctic Basin Symposium, Oct., 1962, Arctic Institute of North America, Washington, 1962.

- Wu, S.S. (1965), "A Study of the Heat Transfer Coefficients in the Lowest 400 m of the Atmosphere", J. Geophys Res., 70, 1801-1807.
- Wyngaard, J.C. (1973), "On Surface-Layer Turbulence", in Workshop on Micro-meteorology, D. Haugen (ed.), Boston: American Met. Soc., 392 pp.
- Yamamoto, G. (1962), "Direct Absorption of Solar Radiation by Atmospheric Water Vapor, Carbon Dioxide and Molecular Oxygen", J. Atmos. Sci., 19, 182-188.
- Yamamoto, G., M. Tanaka, and S. Asano (1970), "Radiative Transfer in Water Clouds in the Infrared Region", J. Atmos. Sci., 27, 282-292.
- Yamamoto, G., M. Tanaka, and S. Asano (1971), "Radiative Heat Transfer in Water Clouds by Infrared Radiation", J. Quant. Spectrosc. Radiat. Transfer, 11, 697-708.
- Zakharova, I.M. (1972), "A Mathematical Model of the Evolution of Radiation Fog", ARCL-72-0720, 25 pp.
- Zavarina, M.V. and O.G. Dyuzheva (1959), "Horizontal Extent of Clouds in the Arctic", Probl. Arkt., 6.
- Zavarina, M.V. and M.K. Romasheva (1957), "Thickness of Clouds over Arctic Seas and over the Central Arctic", Probl. Arkt., 2.
- Zavarina, M.V. and M.K. Romasheva (1959), "Altitude of the Lower Boundary of Clouds over the Arctic", Trudy AANII, 217.
- Zdunkowski, W.G. and B.C. Nielsen (1969), "A Preliminary Prediction Analysis of Radiation Fog", Pure and Appl. Geophys., 19, 45-66.
- Zdunkowski, W.G. and A.G. Barr (1972), "A Radiative-Conductive Model for the Prediction of Radiation Fog", Boundary Layer Met., 3, 152-177.
- Zilitinkevich, S.S., D.L. Laikhtman, and A.S. Monin (1967), "Dynamics of the Atmospheric Boundary Layer", Izv. Atm. Oceanic Phys., 3, 297-333.

BIOGRAPHICAL NOTE

The author was born on 13 September 1948 in Chicago, Illinois. He was raised on the south side of Chicago, and attended high school at De La Salle Institute. He entered the University of Chicago in 1966 as a political science major, and graduated in 1970 in physics and chemistry. His interests in geophysical problems were first stimulated by his association with Dr. Edward Anders, with whom he worked on experimental studies of meteorites and lunar material from the Apollo program. He entered MIT in 1970, where his main areas of interest have been Arctic meteorology, and interactions of radiative transfer with atmospheric dynamics. He has published a number of original papers both in meteorology and in meteoritics.